Finite Element Modeling and Experimental Study of Brittle Fracture in Tempered Martensitic Steels for Thermonuclear Fusion Applications

PAR

Pablo Federico MUELLER

EPFL

ÉCOLE POLYTECHNIQUE
FÉDÉRALE DE LAUSANNE

Suisse
2009

To Carla, Federico and Camila

Abstract

In this work we have studied brittle fracture in high-chromium reduced activation tempered martensitic steels foreseen as structural materials for thermonuclear fusion reactors. Developing the adequate materials that can withstand the severe irradiation conditions of the burning plasma in a future fusion reactor is one of the major challenges to be solved in order to make profit from the great advantages of thermonuclear fusion as an energy source. High-chromium tempered martensitic steels such as F82H and the most advanced version Eurofer97 are among the main candidate materials for structural applications in future fusion power plants due to low irradiation-induced swelling, good mechanical and thermal properties, and reasonably fast radioactive decay. The most concerning drawback of these kind of steels is irradiation embrittlement, which is manifested by a ductile-to-brittle transition temperature shift to higher temperatures after irradiation whose amplitude depends on the irradiation conditions (temperature, neutron flux, neutron fluence, etc)

The aim of this work was to study and model brittle fracture in the ductile-brittle transition region of this kind of steels in the as-received unirradiated conditions. It is necessary to be able to transfer laboratory specimen fracture data to real components and structures in order to assess the performance of these steels in the different operating and transient conditions they could find during the operation life of a fusion reactor. In order to do so, the specimen geometry effects and specimen size effects on measured fracture toughness need to be properly understood, taken into account and predicted with an appropriate model. In particular, specimen size effect on measured toughness is a major concern for the nuclear materials research community owing to the limited irradiation volume in current and planed materials irradiation facilities. The main results of this PhD work are summarized below.

The microstructure of Eurofer97 and F82H has been characterized and compared by means of optical microscopy, scanning electron microscopy, transmission electron microscopy and energy-dispersive X-ray spectroscopy in order to identify

microstructural features that could play a role in the measured fracture toughness. Both steels have similar but slightly different chemical composition and final heat-treatments but the prior austenitic grain size measured in F82H is approximately 8 times larger than in Eurofer97. It was shown that the alloying element Tantalum, added to stabilize the austenite grain size, played a different role in both steels. After a careful analysis of the particles present in both steels, it was found that Tantalum in Eurofer97 formed carbides of an average size around 100 nanometers. In contrast in F82H it did not form small carbides but formed big oxide inclusions with a size up to 30 μm. These large particles do not effectively pin the grain boundaries. The different behavior of Tantalum in these steels is believed to be mainly a consequence of the larger content of Oxygen present and the smaller amount of Aluminum in F82H compared to Eurofer97.

The Master-Curve ASTM-E1921 standard is a method initially developed to determine the ductile-to-brittle transition reference temperature, T_0, in fission reactor ferritic steels from a small number of experiments. In this work the applicability of the Master-Curve method to reduced activation tempered martensitic steels such as Eurofer97 and F82H was studied in detail. Fracture tests with pre-cracked sub-sized compact tension specimens (three different sizes, 0.18T, 0.35T and 0.87T of Eurofer97) were carried out in the temperature range [-196 °C, -40 °C]. The toughness-temperature behavior and scatter were shown to deviate from the ASTM-E1921 standard predictions near the lower shelf. Using the method of maximum likelihood, the athermal component of the Master-Curve was calculated to better fit our fracture toughness data from the lower to the middle transition region. We showed that these Master-Curve adjustments are necessary to make the T_0 values obtained near the lower shelf with 0.35T size C(T) specimens consistent with those obtained in the middle transition region with 0.87T C(T) specimens. The ASTM-E1921 specimen size limitations, setting the maximum toughness measurable with a given specimen size, were found to be too lenient for this kind of steels. This problem was especially evident in fracture toughness data of Eurofer97 and F82H obtained in the upper transition temperature range with two different specimen sizes. Thus a more stringent specimen size requirement was proposed to avoid inconsistent transition temperature determinations.

A promising local fracture model with the potential of predicting cleavage fracture toughness was studied. Finite element simulations were undertaken for compact specimens, notched specimens and tensile specimens of Eurofer97 steel tested from 20 °C down to -197 ºC. Three and two dimensional as well as axisymmetric simulations were run in order to calculate the stress and strain fields at the onset of brittle fracture. For each tested temperature, the calculated load-displacement curves were found to reproduce very well those of the experiments. A local approach fracture criterion was studied. This criterion states that when the maximum principal stress is larger than a critical stress within a critical volume ahead of the crack tip, notch or neck, cleavage is triggered leading to macroscopic fracture of the specimen. It was shown that this model is able to predict the minimum fracture load of the notched specimens with the same values of critical stress and critical volume that were calibrated to predict the lower bound of fracture in compact specimens. This local approach model was also successfully used to predict the strong size effect observed experimentally in pre-cracked compact tension specimens in the upper transition region. The critical fracture stress determined in the standard tensile specimens was found higher than that of the fracture specimens. It was suggested that this difference stems from a significant difference in the stress state between the different specimens (triaxiality).

Finally, the comparison between the overall fracture behavior in the transition between F82H and Eurofer97 steels indicated that these two materials are quite similar. A difference in the reference temperature T_0 of about 20 °C was found, with a nominal value of -100 °C and -80 °C for F82H and Eurofer97 respectively. However, some excessive scatter in the toughness data was found in F82H with more data points than expected lying below the 1% tolerance bound; this was not observed in Eurofer97. From an engineering point of view, the entire fracture databases of these two steels are encompassed practically by the same lower tolerance bound.

Keywords: Brittle fracture, tempered martensitic steels, ductile-to-brittle transition, master curve, local approach, finite element modeling.

Résumé

Dans ce travail, nous avons étudié la fracture fragile des aciers martensitiques revenus à forte teneur en chrome et à activation neutronique réduite, prévus comme matériaux de structure pour les réacteurs à fusion thermonucléaire. Développer des matériaux adéquats résistant aux conditions extrêmes d'irradiation d'un plasma d'un futur réacteur de fusion est un des défis majeurs à relever pour mettre à profit les avantages indéniables de la fusion thermonucléaire en tant que source d'énergie. Les aciers martensitiques revenus à forte teneur en chrome, tels que l'acier F82H ainsi que la version plus avancée Eurofer97, sont parmi les principaux matériaux candidats pour des applications structurales des futurs réacteurs de fusion en vertu de leur faible propension au gonflement induit par irradiation, à leurs bonnes propriétés mécaniques et thermiques et une décroissance relativement rapide de la radioactivité induite. Un des désavantages principaux de ce type d'acier est la fragilisation induite par irradiation, qui se manifeste par une augmentation de la température de la transition ductile-fragile dont l'amplitude dépend des conditions d'irradiation (température, flux et fluence neutroniques, etc…).

L'objectif de ce travail a été d'étudier et de modéliser la fracture fragile dans le domaine de la transition de ces aciers dans leur état final de production non-irradié. Il est nécessaire d'être capable de transférer les données de fracture d'échantillons de laboratoire à des composants réels et des structures afin d'évaluer la performance des ces aciers dans les conditions d'opération et de transitoire qu'ils peuvent rencontrer durant la durée de vie du réacteur de fusion. Dans ce but, les effets de géométrie et de dimension d'échantillons sur la ténacité mesurée doivent être bien compris, pris en compte et prédits par un modèle approprié. En particulier, les effets de dimension des échantillons est une question majeure pour la communauté de recherche sur les matériaux nucléaires en raison des volumes d'irradiation limités des sources actuelles et futures. Les résultats de ce travail de thèse sont résumés ci-dessous.

Les microstructures de l'Eurofer97 et du F82H ont été caractérisées et comparées par microscopie électronique, par microscopie électronique à balayage et transmission et par analyse dispersive en énergie de rayons-X dans le but d'identifier certaines particularités microstructurales qui pourraient jouer un rôle sur la ténacité en fracture. Les deux aciers ont des compositions chimiques et traitements thermiques finaux similaires, quoique légèrement différents, mais la taille des grains austénitiques est environ huit fois plus grande dans le F82H que l'Eurofer97. Il a été montré que le tantale, élément d'alliage, ajouté pour stabiliser les grains austénitiques, joue un rôle différent dans ces deux aciers. Après une analyse détaillée des particules présentes dans ces aciers, il a été trouvé que le tantale dans l'Eurofer97 forme des carbures de dimension moyenne de l'ordre de 100 nm. Au contraire, dans le F82H, le tantale ne forme pas des carbures mais des grands oxydes de structure complexe dont la taille peut être de 30 μm. Ces grandes particules n'épinglent pas efficacement les joints de grains. Ce comportement différent du tantale dans ces aciers est pensé être la conséquence d'un contenu en oxygène plus élevé et d'un contenu en aluminium plus petit dans le F82H en comparaison avec l'Eurofer97.

Le standard ASTM-E1921 de la courbe-maîtresse est une méthode développé initialement pour déterminer la température de référence T_0 de la transition ductile-fragile des aciers ferritiques des cuves des réacteurs de fission à partir d'un nombre restreint d'essais. Dans ce travail, l'applicabilité de la méthode de la courbe-maîtresse aux aciers martensitiques tels que Eurofer97 et F82H a été étudié en détail. Des essais de fracture sur des échantillons de traction compacts pré-fissurés (trois dimensions différentes, 0.18T, 0.35T et 0.87T d'Eurofer97) ont été réalisés dans le domaine de température [-196 °C, -40 °C]. Le comportement ténacité-température et la dispersion des résultats ont été trouvés s'écarter des prédictions du standard ASTM-E1921 près du plateau inférieur. En utilisant la méthode de l'estimation du maximum de vraisemblance, la composante athermique de la courbe-maîtresse a été calculée pour ajuster la courbe sur nos données de ténacité en fracture depuis le bas jusqu'au milieu de la transition. Nous avons montré que ces ajustements de la courbe-maîtresse sont nécessaires pour rendre les valeurs de T_0 obtenues vers le plateau inférieur avec des échantillons de dimensions 0.35T cohérentes avec celles obtenues dans le milieu de la transition avec des échantillons de dimensions 0.87T. Les limitations de dimensions

imposées par le standard ASTM-E1921, définissant la ténacité maximale mesurable avec un échantillon de taille donnée, ont été trouvées trop tolérantes pour ce type d'acier. Ce problème était particulièrement évident sur les données de ténacité obtenues dans la partie haute de la transition avec des échantillons de deux tailles différentes. Aussi une limite de taille d'échantillon plus restrictive a été proposée afin d'éviter des incohérences dans la détermination de la température de transition.

Un modèle prometteur basé sur l'approche local de la fracture avec le potentiel de prédire la ténacité en clivage a été étudié. Des simulations par éléments finis des échantillons de traction compacts, d'échantillons de traction avec une encoche et d'échantillons de traction standard d'Eurofer97 ont été entreprises pour des températures d'essais comprises entres -197 °C et 20 °C. Des simulations deux et trois dimensionnelles ainsi qu'axisymétriques ont été faites pour calculer les champs de contraintes et de déformations au point d'initiation de la fracture fragile. Pour chaque température d'essai, les courbes calculées ont parfaitement reproduit les courbes expérimentales. Un critère du modèle de fracture locale, basé sur un volume critique dans lequel une contrainte critique est atteinte en tête de fissure, d'encoche, ou dans la scission, prédit que le clivage est initié conduisant à la rupture macroscopique de l'échantillon. Il a été montré que ce modèle est capable de prédire la charge minimale de fracture des échantillons ayant une encoche avec les mêmes valeurs critiques de contrainte et de volume que celles calibrées sur la courbe de tolérance 1% des échantillons de fracture de traction compacts. Cette approche locale a aussi été utilisée avec succès pour prédire les forts effets de taille d'échantillons observés expérimentalement sur les échantillons pré-fissurés de traction compacts dans la partie haute de la transition. La contrainte de fracture critique déterminée pour les échantillons standards a été trouvée plus élevée que celle des échantillons de fracture. Il a été suggéré que cette divergence est due à une différence de l'état du champ de contrainte entre les différents échantillons (triaxialité).

Finalement, la comparaison des propriétés générales de fracture dans la transition entre les aciers F82H et l'Eurofer97 a indiqué que ces deux matériaux sont très similaires. Une différence de température de transition d'environ 20 °C a été trouvée, avec une valeur nominale de -100 °C et -80 °C pour le F82H et Eurofer97 respectivement. Cependant une dispersion excessive des données du F82H a été

trouvée avec plus de points que prédit se situant au-dessous de la courbe de tolérance 1% ; cela n'a pas été observé pour l'Eurofer97. D'un point de vue engineering, les bases de données entières de ténacité de ces deux aciers, sont pratiquement englobées par la même courbe de tolérance.

Mots clés : fracture fragile, aciers martensitiques revenus, transition fragile-ductile, courbe maîtresse, approche locale, modélisation par éléments finis.

Table of Contents

Chapter 1

Chapter 2

Chapter 3

Chapter 4

Chapter 5

Chapter 6

Chapter 7

Chapter 1

Introduction

Thermonuclear fusion power appears as a promising energy source for the future to fulfill the growing energy need of the world population. One of the greatest challenges that the realization of nuclear fusion power plants face is the development of new materials able to sustain the aggressive irradiation environment of a burning deuterium-tritium plasma. For the last three decades, international fusion material programs in Europe, Japan, US and more recently in China have been highly focused on the development of the so-called reduced activation tempered martensitic steels such as F82H steel and the more advanced version Eurofer97 steel. Eurofer97 is the reference material for the test blanket modules of ITER. These high-chromium steels are among the main candidate materials for structural applications in future fusion power plants due to low irradiation induced swelling, good mechanical and thermal properties, and reasonably fast radioactive decay. While being attractive materials, the major degradation of their mechanical properties under the reactors operating conditions is reflected by irradiation embrittlement, which is characterized by an upward shift of the ductile-to-brittle transition temperature and a toughness decrease in the ductile regime.

The objective of this research is to better understand and model brittle fracture of the reduced activation tempered martensitic steels in the ductile-brittle transition region. It is well known that measured fracture toughness is specimen size dependent, at least for specimen types usually used. Therefore the models need to account for specimen size and geometry effects on measured toughness. Indeed, specimen size effect on brittle fracture, for instance, is a major concern for the nuclear materials research community that is forced to test a reduced number of small specimens when studying irradiated materials. This strong limitation mainly comes from the limited volume of current and future material irradiation facilities. The miniaturization of the specimens is also driven by the need of reducing the strong neutron flux gradient intrinsic to most irradiation sources and therefore to obtain a reasonable irradiation damage homogeneity through a given specimen. In addition, it is also highly desirable to miniaturize the specimens from the point of view of handling, testing and managing radioactive materials. The fracture models also need to describe the fracture properties in the ductile-brittle transition temperature domain and ideally to predict the upper shift of the transition temperature induced by irradiation-hardening.

For this study, three main sub-objectives were defined. We will need first to complete the fracture toughness database of Eurofer97 steel in particular in the upper transition region where not enough data was available to precisely assess the temperature toughness behavior over the entire ductile to brittle transition temperature range. This data will serve us as baseline to model the toughness behavior in the transition region. Second a local approach fracture model to predict cleavage is studied and calibrated. This kind of model intends to predict brittle fracture from the local stress and strain fields around the crack tip of a fracture specimen calculated from finite element simulations. The main experimental inputs for these simulations are the two elastic constants and the plastic flow curve of the material which will be obtained from tensile tests data. The idea is to predict the cleavage fracture dependence on: specimen size, specimen type, geometry and test temperature. Third, we will make an assessment of the validity of the Master Curve methodology, as described in the ASTM-E1921 standard, for these high-alloyed tempered martensitic steels. Possible adjustments on the Master-Curve will be considered if necessary. Finally, we will highlight the differences in the fracture behavior of F82H-mod and Eurofer97 and attempt to relate them to microstructural observations undertaken in this study.

This work is divided in seven Chapters: Introduction, Literature survey, Microstructural observations, Mechanical tests, Finite element simulations, Discussion and Conclusions. After this Introduction, the literature survey is presented in Chapter 2 along with some important theoretical concepts needed to understand the work. In Chapter 3 we report a microstructural investigation of Eurofer97 and F82H-mod steels performed in order to have a good characterization of the studied materials and to relate specific features to the micromechanical fracture models applied afterwards. The experimental results are presented in Chapter 4 along with an in-depth study of the fracture toughness properties of Eurofer97 in terms of the Master Curve approach. In Chapter 5 finite element simulations are compared with the mechanical tests presented in Chapter 4; we also present and employ a local approach model to predict brittle fracture based on the numerical simulations. A general discussion of the work is presented in Chapter 6 and finally we recall the main conclusions in Chapter 7.

Chapter 2

Literature survey and theory

2.1 Reduced-activation high-chromium steels for fusion reactor structures: Development and challenges

The ultimate goal of thermonuclear research is to harvest the energy released by the fusion of light elements. The easiest fusion reaction to initiate involves deuterium and tritium that releases one ^{4}He and one neutron according to:

$$D^+ + T^+ \Rightarrow He^{++} \text{ (3.5 MeV)} + n \text{ (14.1 MeV)}$$
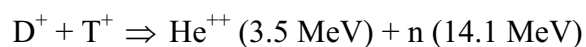
The first generation of fusion reactors will be based on that reaction and these devices will rely on the tokamak configuration (Figure 2-1) to confine magnetically the plasma whose temperature will be of the order of 100 – 200 millions of degrees [1]. Thanks to their charge, the alpha particles (He^{++}) remain confined in the plasma yielding their energy to the burning plasma. Thus, they compensate energy loss and can make the nuclear reactions self-sustaining. On the contrary, the energetic neutrons leave the plasma creating a flux on the structure facing the plasma. Being not charged, the neutrons interact with the nuclei of the material producing high-energy primary recoil atoms (PKAs), with energies ranging from less than 1 keV to several hundreds

keV [2]. The energy of the PKA is then partitioned between the surrounding atoms, creating a series of secondary recoil atoms, which ultimately create a cascade of displacements. All these recoils atoms leave their normal lattice site producing a vacancy and its associated interstitial: the so-called Frenkel pair. However, only a minority, about 10%, of the displaced atoms from their lattice sites survive the recombination phase of the cascade as interstitials atoms, vacancies or small clusters. Some of these defects are highly mobile and diffuse towards grain boundaries, dislocations, precipitate at boundaries or aggregate in the form of extended defects such as voids or small faulted loops for example [2].
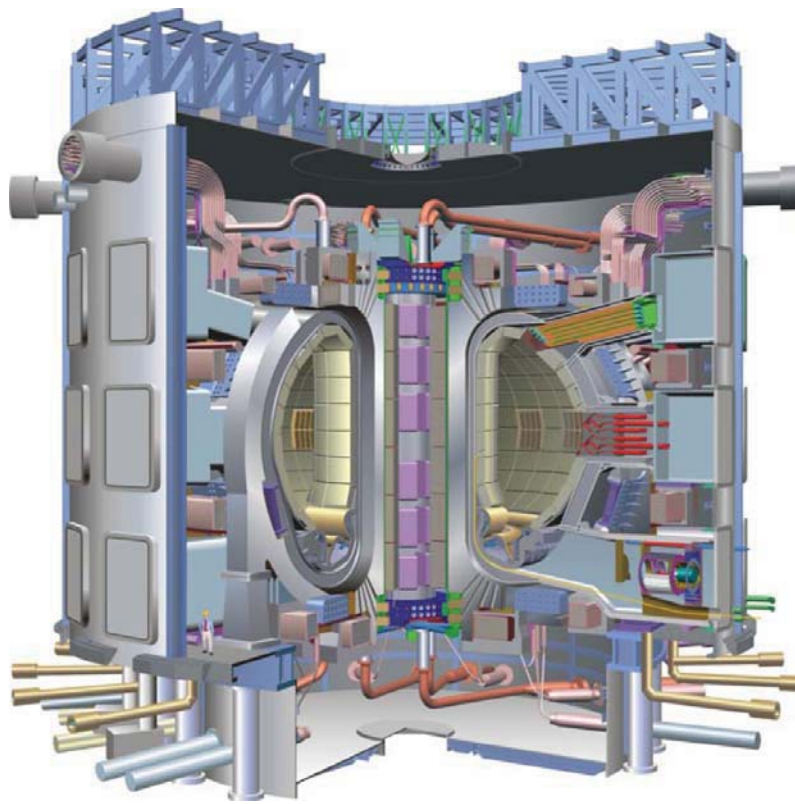
Figure 2-1: ITER International Thermonuclear Experimental Reactor to be built in Cadarache France. It is a Tokamak type fusion reactor.

Transmutation reactions constitute another source of radiation damage. In particular, gaseous transmutation products, such has helium and hydrogen, produced from (n,α) and (n,p) reactions respectively, are well known to impact the evolution of the microstructure and to degrade the mechanical properties. Typically, the (n,α) reaction has a threshold energy of the order of 5 MeV for the elements typically used in structural alloys for fusion [3].

The accumulation of irradiation defects in the microstructure depends strongly on irradiation temperature, T_{irr}, typically:

a) At low irradiation temperature, $T_{irr} < 0.3T_m$, where T_m is the melting temperature, the vacancy do not evaporate from their cluster. The microstructure is dominated by defect clusters that are responsible for the irradiation hardening, namely an increase of the flow stress, and a subsequent degradation of the fracture toughness.

b) At intermediate irradiation temperature, $0.3T_m < T_{irr} < 0.5T_m$, phenomena such as irradiation-creep and swelling occur.

The microstructural irradiation-induced changes of the materials do not depend only on the irradiation temperature but also on a variety of other parameters such as: neutron flux, neutron spectrum, neutron fluence, neutron fluence rate, chemical content of the investigated material as well as its overall thermo-mechanical processing and final heat-treatment.

Material exposure to neutrons is usually characterized by the average number of total displacements per atom (dpa) [4]. The *dpa* has replaced the measure of neutron fluence as well as the neutron flux by *dpa s⁻¹*. The damage rate is calculated as:

$$\text{dpa}/s = \int_0^\infty \sigma_d(E)\phi(E,t)dE \tag{2.1}$$

where $\sigma_d(E)$ is the displacement cross-section for a particular material and $\phi(E,t)dE$ is the neutron flux in the energy range E to E+dE. The displacement cross-section is obtained from the cross-section of energy transfer to the pka, which is converted into a number of displacements using the Norgett-Torren-Robins model [5].

$$N_d(T_d) = \left[\begin{array}{ll} 0 & T_d < E_d \\ 1 & E_d \leq T_d < 2E_d/\beta \\ \dfrac{\beta T_d}{2E_d} & 2E_d/\beta \leq T_d < \infty \end{array} \right. \tag{2.2}$$

N_d is the number of displaced atoms, $\beta=0.8$ is an atomic scattering correction factor, $E_d=40$ eV is an effective displacement threshold energy and T_d is the damage energy.

In a tokamak type of fusion reactor, the plasma is surrounded by the first wall covering the blanket as well as by the divertor on the bottom part of the torus. Most of the neutrons interact with the first wall and penetrate inside the blanket. The blanket serves as: i) a converter of the neutron energy to heat, ii) a tritium breeder, iii) transfer system of the heat to the cooling system and iv) provide some shielding for the magnets. The neutrons slow down as they penetrate the reactor structure components; consequently, the neutron spectrum also becomes softer with the penetration depth and so does the PKA spectrum itself. In addition, the irradiation temperature is not uniform so that the magnitude of the irradiation effects will be strongly position dependent in the components. As an example, we report below the damage and gaseous impurities production rate in steel at the level of the first wall, which is the most exposed part, of a 3-4 GW fusion power reactor [6]:

Damage rate:	20-30 dpa/year
Helium production:	10-15 appm/dpa
Hydrogen production:	40-50 appm/dpa

In the mid 80's, the concept of *low-activation materials* was introduced, which can be regarded as materials which would either not activate or with an induced-radioactivity from the transmutation elements that would quickly decay to allow safe operation and hands-on reactor maintenance [7]. Note that several criteria were proposed to define the concept of *low-activation materials* [8]. They take into account three fundamental conditions: radioactive emissions in routine and off-normal conditions, maintenance operations after a shutdown, and finally waste management and disposal aspects. To be *low-activation* with very short decay half-life, a given material must not contain chemical elements susceptible to transmute into long-lived radioactive elements. Note that the transmutation products of iron do not generate very short radioactive half-life elements and so prevent the production of real low-activation steels. In addition, for being *low-activation* structural materials, the concentration of impurities, which form

long-lived radioactive nuclides, must be extremely low (<< 1 at. ppm) [9]. Such low levels make it practically impossible to produce low-activation materials at industrial scale so that the concept of *reduced-activation materials* arose. Radioactivity from reduced-activation materials should decay to low levels in about 100 years. Only few chemical elements can be considered in the definition of the chemical composition of an alloy that must meet the requirements for reduced activation materials, namely Fe, Cr, V, Ti, W, Ta C, [10].

The goal of the long-term material development for a demonstration reactor is to produce materials that can withstand the aggressive plasma environment: they must keep their integrity, their dimensional stability and their functionality. Nowadays, the reduced activation tempered martensitic steels appear among the most promising candidate material for the first wall and the blanket of a fusion reactor and are being the reference material for the test blanket module of the International Thermonuclear Experimental Reactor [11]. They were introduced in the international fusion material development programs about 30 years ago. Originally, they were proposed in the middle of the 70s as replacement of the austenitic steel in the high neutron damage applications, in particular for the liquid metal fast breeder reactors. It was indeed observed that cavities developed in austenitic steels lead to a volumetric expansion, called *swelling*, with an associated irradiation-induced creep, which turned out to be a limiting factor [12]. Alternative materials were proposed, like the tempered martensitic steels that were shown to have much better swelling resistance than the austenitic steels, even up to doses over 200 dpa [13]. In addition, the tempered martensitic steels present a good balance of thermal, physical and mechanical properties at high temperatures [7]. The composition of the most advanced tempered martensitic steels results from the original composition of the Cr-Mo conventional steels where the Mo has been replaced by W and/or V and Ni by Ta. In 1992 in Tokyo, an international collaboration (Japan, US, Europe) was initiated to, under the auspices of the International Energy Agency, study the feasibility of using high-chromium steel for fusion structural components. Two large 5-tons heats of reduce-activation steels, called F82H-mod, were produced by Japan Atomic Energy Research Institute and NKK Corporation; the composition of the steels was Fe-7.5Cr-2W-0.2V-0.04Ta. The physical and material properties of these heats were determined and introduced into a database available to the fusion material community. Irradiation

experiments in more than twenty different facilities were carried out throughout the world. Investigations and experiments on these F82H-mod plates are still in progress. More recently, another steel, designated Eurofer97, was produced in Europe. This steel is currently the reference material for the blanket modules to be tested in the International Thermonuclear Experimental Reactor [14]. The composition of the Eurofer97 slightly differs from that of the F82H-mod in the Cr, W and Ta contents. The lower tungsten content was actually intended because the tritium-breeding rate is higher for lower tungsten content. In addition, lower tungsten levels tend to reduce the amount of Laves phases formed with respect to higher contents [7].

2.2   Fracture toughness and ductile-brittle transition

The toughness concept applies equivalently to different critical loading conditions of cracked bodies. For instance, it can be related to static fracture toughness K_{Jc}, to dynamic fracture toughness K_d, to fracture toughness arrest K_a. Since the work undertaken in this study is related to static fracture toughness, we mainly focus on the K_{Jc} parameter in the following. In a cracked body, it is useful to define a parameter that relates the applied loads P and their displacement points D to the near crack tip stress/strain fields that result from those loads and that ultimately mediate the crack initiation and propagation. For a cracked specimen loaded elastically from the macroscopic point of view in mode I, having a deep crack and very small plastic zone with respect to the actual dimension of the specimen, the parameter describing the fields is the elastic stress-intensity factor written as [15, 16]:

$$K_I = f(\frac{a}{W})(\frac{P}{BW})\sqrt{a} \qquad\qquad (2.3)$$

with *a* the crack length, W the specimen width, B the crack front, f(a/W) a non-dimensional geometrical function and P the load. In case of unstable fracture, K_{Ic} is the critical stress intensity factor, calculated at the critical load in the macro-elastic domain of the P-D curve, and represents the elastic toughness of the material. K_{Ic} can

be regarded as material property only if the following strict specimen size requirements are met [15]:

$$(W - a) \geq 2.5 \left(\frac{K_{Ic}}{\sigma_{ys}} \right)^2 \qquad (2.4)$$

where σ_{ys} is the yield stress.

When the specimen cleaves at a point of the macroscopic P-D curve beyond the K_I validity range, the concept of elastic critical stress intensity factor is not valid any more. In this case it has to be generalized by another parameter which is the energy release rate, also called the J-integral. Experimentally, J is obtained from [16]:

$$J = (K_I^2 / E') + \eta A_p / bB \qquad (2.5)$$

From J, one defines an elastic-plastic loading parameter as [15]

$$K_J = \sqrt{E'J} \qquad (2.6)$$

$E'=E/(1-v^2)$ is the plane-strain elastic modulus, E the Young modulus, v the Poisson ratio, η is a constant that depends on the specimen geometry, A_p is the plastic work area under the P-D curve, B is the crack front length and b is the uncracked ligament length, respectively. Similarly to K_{Ic}, K_{Jc} is determined by the applied load at fracture and defines the elastic-plastic fracture toughness of the material. K_{Jc} corresponds to the initiation of an unstable crack before stable tearing occurs. Even for small-scale yielding condition, namely for a very small plastic zone size with respect to the other specimen dimensions, K_{Jc} is observed to depend on the crack front length for common specimen sizes.

The tempered martensitic steels are body-centered cubic (bcc) materials and share with other bcc alloys several similar characteristics. One critical issue resides in the fact that bcc alloys exhibit a so-called ductile-to-brittle fracture mode transition from high-temperature microvoid coalescence to low-temperature quasi-cleavage (fast or

unstable fracture) [17]. The transition region between the upper and lower shelves spreads over more than 100 °C. In the transition region, the fracture mode remains unstable, being quasi-cleavage for the tempered martensitic steels [18]. Note that a very large scatter in the data is observed in the transition region, which is inherent to the probabilistic nature of unstable fracture [19, 20]. A schematic illustration of the fracture toughness-temperature dependence is given in Figure 2-2. Owing to the intrinsic probabilistic nature of cleavage, a very large scatter is observed in the transition region so that it is common to describe the data with cumulative probability functions and draw a lower and upper bounds representing given cumulative failure probabilities. In order to define a transition temperature, one usually uses T_o that corresponds to the temperature at which the median fracture toughness is 100 MPa $m^{1/2}$.
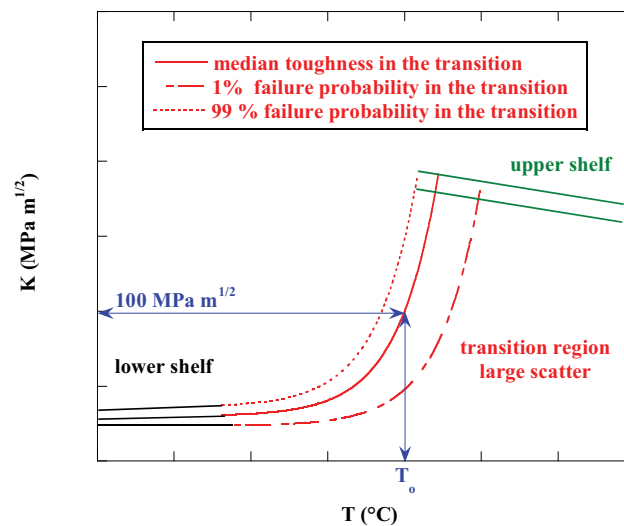
Figure 2-2: Illustration of the fracture toughness-temperature dependence of "ferritic" steel.

A similar transition behavior between a ductile and brittle regime is also observed from Charpy impact test. In this type of test, the absorbed energy to fracture a notched bar loaded behind the notch by the impact of a pendulum is recorded as a function of the testing temperature. Figure 2-3 illustrates the type of curves obtained from Charpy impact experiments.
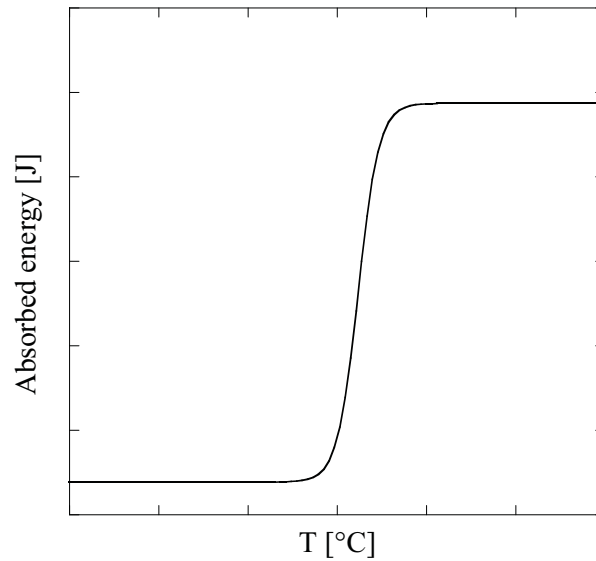
Figure 2-3: Illustration of the Charpy impact energy – temperature curve.

Three different measurements are used to define the so-called ductile-brittle transition, DBTT [21]. First, the DBTT can be indexed at a given absorbed energy; for standard Charpy tests (10 x 10 x 55 mm^3), the DBTT is usually indexed at an absorbed energy of 41 Joules: DBTT = T_{41J}. However, it is also common to define the DBTT at the energy equal the half of that on the upper shelf, in particular for sub-sized specimens. The third measurement relies on ductility characterized by the amount of lateral expansion at the compression side of the specimen. The third DBTT evaluation is based upon the percentage of fracture appearance, which usually changes from 100% percent cleavage at low temperature to 100 % fibrous at high temperature. It must be strongly emphasized here that for both the Charpy and fracture toughness the DBTT is not a material property but it depends on many extrinsic factors such as: the specimen size, the specimen geometry, notch geometry, crack length of fracture specimen, the loading rate, etc. All these factors may lead to a difference in the "DBTT" for a given material which is typically of the order of 100 to 200 °C depending on the testing conditions and specimen size/geometry.

2.3   Embrittlement of "ferritic" steel and master-curve approach

As mentioned in the previous section, the fluence of high-energy neutrons, to which the plasma facing and breeding blanket components of a fusion reactor will be

exposed, leads to significant changes in the mechanical properties of the tempered martensitic steels. For irradiation lower than 425-450 °C, irradiation-hardening occurs, defined by an increase of the yield stress or more generally of the flow stress. Note that above 425-450 °C, irradiation-softening is observed owing to slow dislocation recovery mechanisms and precipitates coarsening enhanced by irradiation [22]. Irradiation-hardening is caused by the production and accumulation of a high density of small dislocation loops, irradiation-induced nano-voids, helium bubbles and small precipitates; all these defects acts as additional obstacles to moving dislocations A reduction of strain-hardening capacity is also often observed after irradiation. The combination of irradiation-hardening and reduction of strain-hardening cause a strong decrease of uniform elongation. This fact is illustrated in Figure 2-4, where the effect on the tensile curves of proton irradiation performed at 50 °C at two doses on the Eurofer97 steel is shown [23].
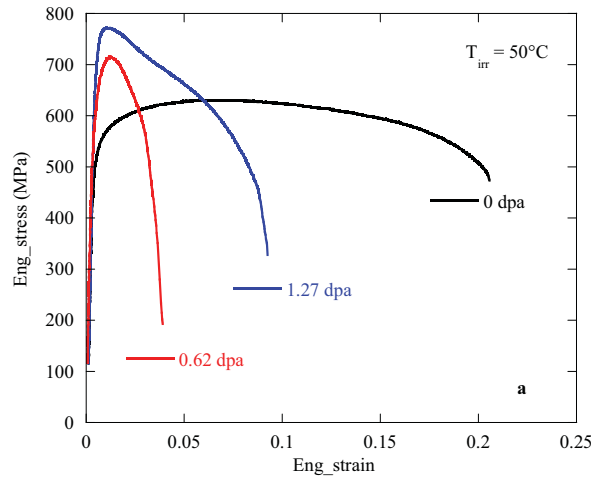
Figure 2-4: Typical tensile curves before and after irradiation at 50 °C, T_{test} = T_{irr}.

The irradiation-hardening has deleterious consequences on the fracture properties that are represented by an upper shift of the DBTT, whatever definition of the DBTT is used (see above). This phenomenon is usually referred to as *embrittlement* [24]. In addition, the upper shelf of both the Charpy test energy and fracture toughness decreases following irradiation. These effects on Charpy impact curve and fracture toughness-temperature curve are shown in Figure 2-5 and Figure 2-6 respectively where the irradiation conditions and materials are indicated in the Figure captions.
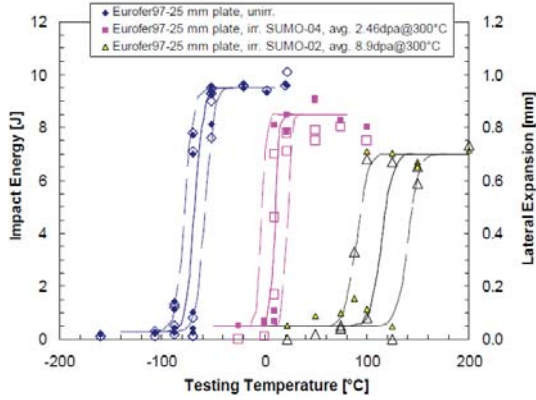
Figure 2-5: Absorbed energy and lateral expansion for sub-sized Charpy specimens of Eurofer97: unirradiated and irradiated conditions [25].
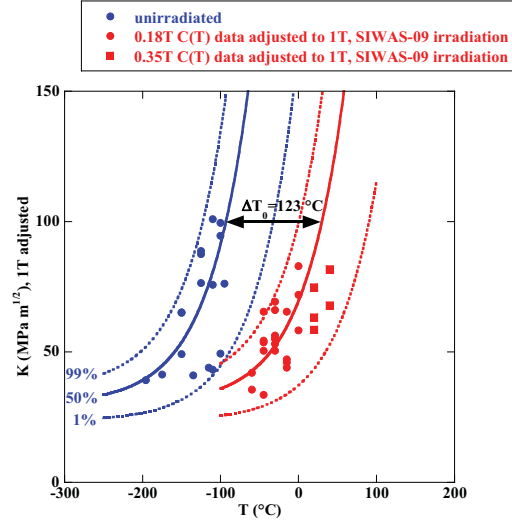
Figure 2-6: K(T) shift of the master-curve after 2.2 dpa at T_{irr} = 60 °C, SIWAS-09 at HFR-Petten [26].

A very efficient way to assess the embrittlement of irradiated tempered martensitic steels is based on the master curve-temperature shifts method [27]. This method is based on the recognition that the toughness-temperature behavior in the transition region of "ferritic" steel is universal and unaffected by irradiation [28]. In other words, the shape of the median toughness-temperature curve is unique. When determined with one inch thick specimen, the equation of the master curve is given by:

$$K_{Jc\_med}(T) = 30 + 70\exp(0.019(T - T_o)) \qquad (2.7)$$

The difference between different "ferritic" steels is accounted for only by T_o that indexes the curve at 100 MPam$^{1/2}$ on the absolute temperature axis. The index T_o is indicated in Figure 2-2. One method to determine T_o is defined in the American Society for Testing and Materials standard, ASTM E1921-08 [29]. As mentioned above, the effect of irradiation is to shift the $K_{Jc\_med}(T)$ curve to higher temperature or equivalently to increase T_o by ΔT_o. Thus, ΔT_o appears as the quantity characterizing the embrittlement. We emphasize that the ASTM E1921 standard is originally intended to quantify the embrittlement of low alloyed reactor pressure vessel steels. Within the Fusion Materials community, there has recently been many fracture studies

on the high-chromium tempered martensitic steels to characterize their behavior in the transition region and to determine the ΔT_o shift following irradiations.

The magnitude of the temperature shifts and of the decrease of the upper shelf values depend on the irradiation conditions. However, since the irradiation-hardening, usually characterized by the increase of the yield stress $\Delta\sigma_y$, strongly depends on the irradiation temperature, it is natural to quantify the embrittlement, defined as the shift of the reference temperature T_o of the master-curve, as a function of $\Delta\sigma_y$ ($\Delta\sigma_y$ is measured at room temperature). Plotting ΔTo versus $\Delta\sigma_y$ was done for all the irradiation performed on the F82H-mod at temperatures between 250 and 380 °C by Yamamoto et al. [30]. This plot is presented in Figure 2-7 where we indicated the corresponding irradiation associated with the data points. In addition, we added few points (blue ones) that were not included in the original plot. In spite of the rather large uncertainty mentioned above, the trend line in Figure 2-7 clearly shows that it is possible to get a reasonable prediction of ΔT_o based upon the irradiation hardening defined as $\Delta\sigma_y$. One of the limitations is related to the fact that the only irradiation effect on the plastic flow explicitly taken into account is the yield stress increase. However, it is well established that irradiation also affect the strain-hardening, especially for high dose.

1. 1/3 PCC, JMTR irradiation, 290 °C, 0.02 dpa

2. 1/3 PCC, JMTR irradiation, 290 °C, 0.14 dpa

3. DC(T), HFIR irradiation, 377 °C, 3.8 dpa

4. 0.38T C(T), HFR SIWAS-09, 60 °C, 2.2 dpa

5. 0.38T C(T), HFR SUMO-09, 300 °C, 2.1 dpa

6. 0.47T C(T), HFR SIWAS-07, 60 °C, 1.43 dpa

7. DC(T), HFIR irradiation, 250 °C, 3.8 dpa

8. 0.39T C(T), HFR, SINEXT-06, 300 °C, 5 dpa

$$\Delta T_0 = 0.58 \ \Delta\sigma_y$$

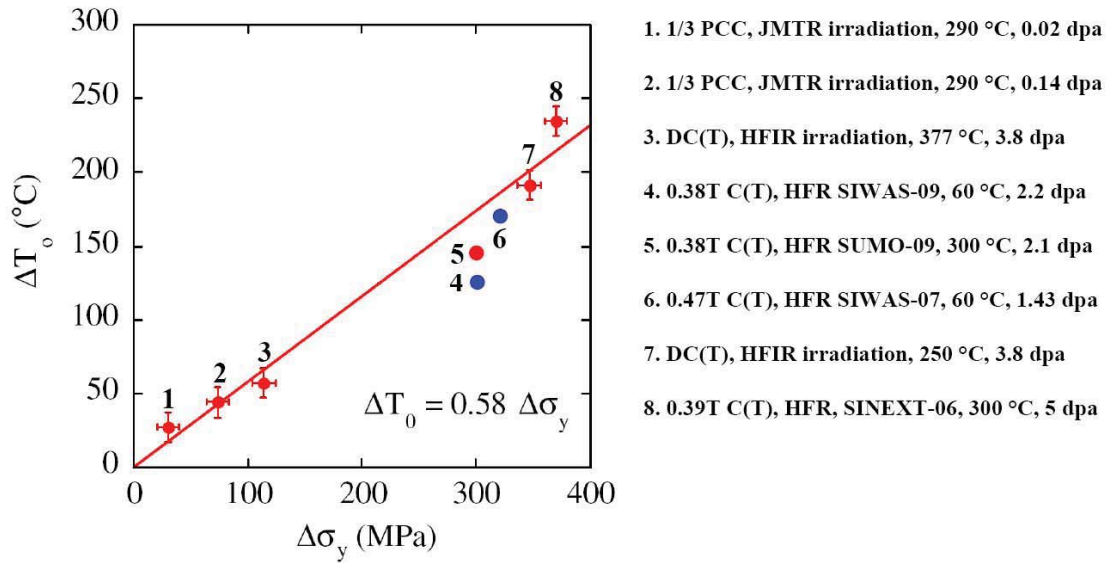**Figure 2-7**: ΔT_0 versus $\Delta\sigma_y$ for all the data presented in [30] on F82H.

The T_o shifts measured from the IRFUMA irradiations in the B2 reactor in Mol and those following the irradiation in HFR reactor in Petten on the Eurofer97 suggest that the ratio $\Delta T_o/\Delta\sigma_y$ is slightly lower for Eurofer97 than for F82H. Indeed, it was found that this ratio is between 0.31 and 0.45 °C/MPa, to compare with 0.58 found for F82H-mod [25, 31]. This difference would probably vanish if we calculated and compared the ratio, $\Delta T_o/<\Delta\sigma_{flow}>$, as it was proposed by Odette et al. [32]. It was already shown that irradiation-induced changes in the strain-hardening law has a profound effect on the local stress/strain fields around the crack tip of the specimens; in fact, these stress/strain fields significantly differ from those obtained by considering only an increase of yield stress with an unmodified strain-hardening behavior [33]. Further, it is the overall flow stress that mediates the stress field in the process zone and therefore that controls cleavage. The peak stress ahead of the crack tip is controlled by the flow stress and not the yield stress only. Thus, it appears more justified to consider an average increase of the flow stress $<\Delta\sigma_{flow}>$ (average over few percent of plastic strain) as the parameter controlling the shift of T_o and write $\Delta T_o = C <\Delta\sigma_{flow}>$. The finite element simulations results of Odette et al. actually support this view as they found a more accurate relation between ΔT_o and $<\Delta\sigma_{flow}>$. We can conclude that the smaller ΔT_o shift of Eurofer97 in comparison to F82H-mod probably results from a more pronounce decrease of strain-hardening in Eurofer97 than in F82H-mod after irradiation.

2.4 Possible issues regarding the applicability of the master-curve to tempered martensitic steels.

Within the fusion material international program, the fracture toughness properties of the two steels F82H-mod and Eurofer97 steels have been investigated. We note that these steels were mainly produced in the form of rolled plate with a maximum thickness of 25 mm but some plates were as thin as 8 mm. As mentioned in Section 2.2, the size of specimen has a strong influence on the measured toughness. The direct consequence of this fact is that rather small specimens had to be used for the undertaken fracture investigations on these steels. This has lead to rather larger

discrepancy between the results between various authors [31]. In order to properly deal with this issue of size effect on toughness, Odette proposed to use a fracture local approach to take into account the specimen size and geometry [18]. In the next Chapters, we will present in details this local approach that we have considered in this work to model the toughness-temperature dependence of Eurofer97 and the specimen size effect. At this point, suffice to say that in the local approach proposed by Odette, one has to define a critical stress field at the crack tip, rather than the critical stress intensity factor, which triggers cleavage. In his model, the critical condition is defined as the attainment of a critical stress σ^*, such as the stress component perpendicular to the crack plane or the maximum principal stress, within a critical volume V^*. Odette et al. [34] assembled the entire existing F82H-mod database, obtained with a large variety of specimens, and applying his model to rescale all the data to one specimen size (1T specimen). In doing so, they showed that the fracture toughness behavior in the transition was reasonably consistent with the master-curve (Eq. (2.7)). In Figure 2-8 and Figure 2-9, the unadjusted toughness data and the size-corrected data are presented respectively. However, in [34], the authors recognized that a total of 34 data points fall below the 5% and 22 above the 95% confidence interval limits, respectively. This is 2.5 times the number (22) of data points expected to fall outside the 5–95% confidence interval.
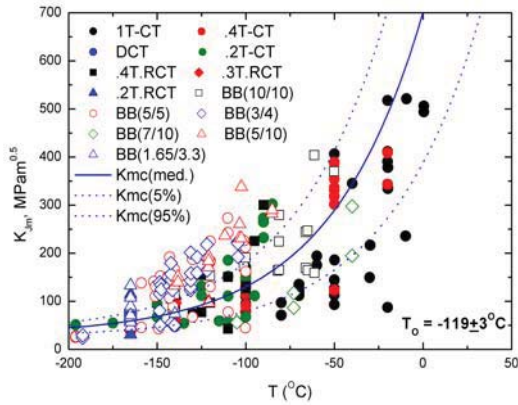
Figure 2-8: Measured fracture toughness data without specimen size adjustment, [35].
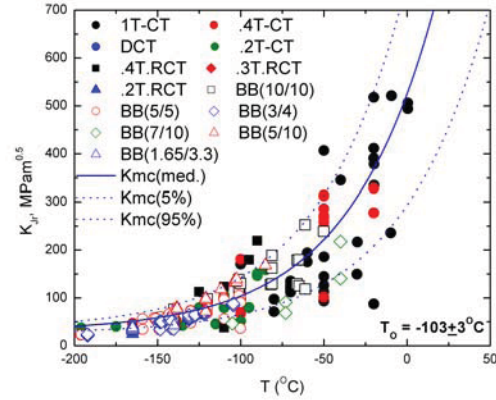
Figure 2-9: Adjusted fracture toughness data with the σ^*-V^* model, [35].

Questions and concerns regarding the applicability of the master-curve approach, as described in the ASTM E1921 standard have been raised by Lucon [36], Bonadé et al.

[37] and Sokolov et al. respectively [38]. Lucon analyzed fracture from a large fracture toughness database made of various tempered martensitic steels, namely Eurofer97, EM10, T91 and HT9 steels in both the unirradiated and irradiated conditions.

In his study, Lucon followed carefully the ASTM E1921 standard to determine the reference temperature T_o of these different steels. He also focused on the scatter of the data and observed that, by plotting the 1% and 5% failure probability bounds as a function of temperature and counting the number of points falling below these curves, the expected number of data was significantly higher than the prediction of the master-curve approach. For example, he counted 13.3% of below the 5%-bound and 4.2% below the 1%-bound (see Figure 2-10). Lucon associated the discrepancy between the data and the prediction to some inhomogeneity of the steels, and suggested more complicated analytical approaches such as the multi-modal master curve [39].
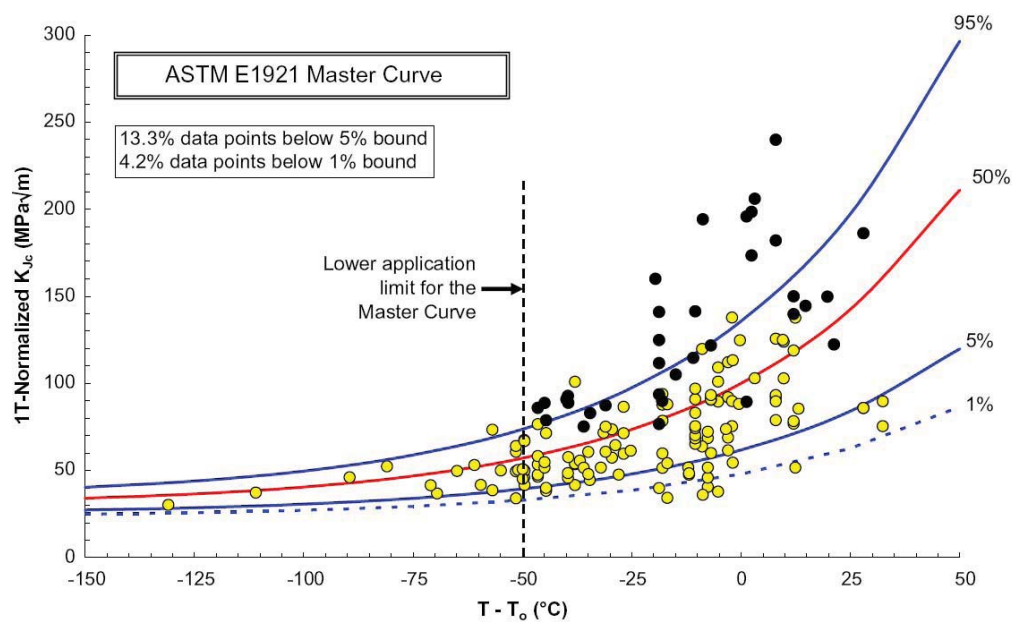
Figure 2-10: MC analysis of 160 fracture toughness test results on E97, EM10, T91 and HT9, [36]. Black solid points are invalid data according to E1921-05.

Similarly to Lucon, Sokolov and Tanigawa [38] showed that the scatter of a 25 mm plate of F82H-mod was larger than anticipated by the standard master-curve. These authors applied a random inhomogeneity analysis of the fracture toughness data

where T_o is considered as a random variable [39]. With such an analysis a much better description of the scatter was found. However, as mentioned by the authors the main drawback of this analysis is the large number of specimens necessary, which constitutes a serious limitations for irradiated material characterization because only a limited number of specimens is usually available for any irradiation conditions.

Bonadé [37, 40] created a database with sub-sized C(T) specimens of Eurofer97 in the lower part of the transition region. He tested a series of specimens at different temperatures in the range –148 to -100 °C so that a median toughness value could be properly determined at each of the selected temperatures. From the temperature dependence of these median values, he found that the master-curve equation (Eq. (2.7) above) did not provide a satisfactory description of the results. He proposed a shape adjustment of the master curve. A steeper master-curve was shown to describe well the data in this restricted temperature range, which was defined as the Eq. (2.7) above with a coefficient 0.04 instead of 0.019.

One of the main objectives of this PhD work, as described in the Introduction, ultimately aimed to better assess the applicability of the master-curve concept on the high-chromium tempered martensitic steels by modeling the specimen size effects on fracture toughness with finite element simulations.

2.5   References

[1]   Ongena J, Van_Oost G. Energy for Future Centuries: Prospects for fusion power as a future energy source. Transactions of Fusion Science and Technology. 2006;49.

[2]   Lucas GE, Odette GR, Rowcliffe AF. Innovations in Testing Methodology for Fusion Reactor Materials Development. MRS Bulletin/July. 1989:29-35.

[3]   Guinan M. Fundamental Studies of Irradiation Effects in Fusion Materials. MRS Bulletin/July. 1989:20-28.

[4]   ASTM. E 693 - 01 (Reapproved 2007). Standard Practice for Characterizing Neutron Exposures in Iron and Low Alloy Steels in Terms of Displacements Per Atom (DPA), E 706(ID); 2001.

[5]   Norgett MJ, Robinson MT, Torrens IM. A Proposed Method of Calculating Displacement Dose Rates. Nuclear Engineering and Design. 1975;33:50-54.

[6]   Baluc N, Abe K, Boutard JL, Chernov VM, Diegele E, Jitsukawa S, Kimura A, Klueh RL, Kohyama A, Kurtz RJ, Lässer R, Matsui H, Möslang A, Muroga T, Odette GR, Tran MQ, van_der_Schaaf B, Wu Y, Yu J, Zinkle SJ. Status of R&D activities on materials for fusion power reactors. Nuclear Fusion. 2007;47:S696-S717.

[7]   Klueh RL. Reduced-activation bainitic and martensitic steels for nuclear fusion applications. Current Opinion in Solid State and Materials Science. 2004;8:239-250.

[8]   Rocco P, Zucchetti M. Criteria for defining low activation materials in fusion reactor applications. Fusion Engineering and Design. 1992;15:235-244.

[9]   Boom EE, Conn RW, Davis JW, Gold RE, Little R, Schultz KR, Smith DL. Low activation materials for fusion applications. Journal of Nuclear Materials. 1984;122-123:17-26.

[10]   Schiller P. Review of materials selection for fusion reactors. Journal of Nuclear Materials. 1993;206:113-120.

[11]   Möslang M, Diegele E, Klimiankou M, Lässer R, Lindau R, Lucon E, Materna-Morris E, Petersen C, Pippan R, Rensman JW, Rieth M, van_der_Schaaf B, Schneider H-C, Tavassoli F. Towards a Reduced Activation Structural Materials Database for Fusion DEMO Reactors. FT/P1-21. 2005.

[12]   Gelles DS. Development of martensitic steels for high neutron damage applications. Journal of Nuclear Materials. 1996;239:99-106.

[13]   Gelles DS. Microstructural development in reduced activation ferritic alloys irradiated to 200 dpa at 420 ºC. Journal of Nuclear Materials. 1994;212-215:714-719.

[14]   van_der_Schaaf B, Tavassoli F, Fazio C, Rigal E, Diegele E, Lindau R, LeMarois G. The development of EUROFER reduced activation steel. Fusion Engineering and Design. 2003;69:197-203.

[15]   Anderson TL. Fracture Mechanics, Fundamentals and Applications, Third Edition. 2005.

[16]   Kanninen MF, Popelar CH. Advanced Fracture Mechanics. 1985.

[17]   Odette GR, Yamamoto T, Rathbun HJ, He MY, Hribernik ML, Rensman JW. Cleavage fracture and irradiation embrittlement of fusion reactor alloys: mechanisms, multiscale models, toughness measurements and implications to structural integrity assessment. Journal of Nuclear Materials. 2003;323:313-340.

[18] Odette GR. On the ductile to brittle transition in martensitic stainless steels - Mechanisms, models and structural implications. Journal of Nuclear Materials. 1994;212-215:45-51.

[19] Wallin K. The Scatter in K_{IC}-Results. Engineering Fracture Mechanics. 1984;19:1085-1093.

[20] Wallin K, Saario T, Törrönen K. Statistical model for carbide induced brittle fracture in steel. Metal Science. 1984;18:13-16.

[21] Dieter GE. Mechanical Metallurgy, Third Edition, SI Metric Edition. 1988.

[22] Bae KK, Ehrlich K, Möslang A. Tensile behavior and microstructure of the helium and hydrogen implanted 12% Cr-steel MANET. Journal of Nuclear Materials. 1992;191-194:905-909.

[23] Spätig P, Stonescu R, Mueller P, Odette GR, Gragg D. Assessment of irradiation embrittlement of the Eurofer97 steel after 590 MeV proton irradiation. Journal of Nuclear Materials. 2009;386-388:245-248.

[24] Rensman J, van_Hoepen J, Bakker JBM, den_Boef R, van_den_Broek FP, van_Essen DDL. Tensile properties and transition behavior of RAFM steel plate and welds irradiated up to 10 dpa at 300 °C. Journal of Nuclear Materials. 2002;307-311:245-249.

[25] Rensman J. NRG Irradiation Testing: Report on 300 ºC and 60 ºC Irradiated RAFM Steels. 2.5 and 10 dpa neutron irradiated Eurofer97 Plate, HIPed Powder, HIP diffusion welds, TIG welds, EB welds, F82H and NRG 9Cr lab heats. 20023/05.68497/P. Petten; 30 August 2005.

[26] Spätig P, Bonadé R, Odette GR, Rensman JW, Campitelli EN, Mueller P. Plastic flow properties and fracture toughness characterization of unirradiated and irradiated tempered martensitic steels. Journal of Nuclear Materials. 2007;367-370:527-538.

[27] Odette GR, Edsinger K, Lucas GE, Donahue E. Developing fracture assessment methods for fusion reactor materials with small specimens. ASTM-STP-1328, American Society for Testing and Materials, Philadelphia, PA. 1998:p. 298.

[28] Wallin K. Irradiation Damage Effects on the Fracture Toughness Transition Curve Shape for Reactor Pressure Vessel Steels. Int J Pres Ves & Piping. 1993;55:61-79.

[29] ASTM. E 1921 - 08. Standard Test Method for Determination of Reference Temperature, T_0, for Ferritic Steels in the Transition Range; 2008.

[30]   Yamamoto T, Odette GR, Gragg D, Kurishita H. Evaluation of fracture toughness master curve shifts for JMTR irradiated F82H using small specimens. Journal of Nuclear Materials. 2007;367-370:593-598.

[31]   Spätig P, Mueller P, Kruml T. Final Report, Task TW5-TTMS-001 deliverable 7, Period 01/2005 - 09/2008, CRPP-EPFL, Assessment of irradiations performed on Eurofer97. Comparison and critical review of the fracture properties and microstructures of RAFM steels. 2008.

[32]   Odette GR, He MY, Yamamoto T. On the relation between irradiation induced changes in the master curve reference temperature shift and changes in strain hardened flow stress. Journal of Nuclear Materials. 2007;367-370:561-567.

[33]   Spätig P, Campitelli EN, Bonadé R, Baluc N. Assessment of plastic flow and fracture properties with small specimen test techniques for IFMIF-designed specimens. Nuclear Fusion. 2005;45:635-641.

[34]   Odette GR, Yamamoto T, Kishimoto H, Sokolov M, Spätig P, Yang WJ, Rensman JW, Lucas GE. A Master Curve Analysis of F82H Using Statistical and Constraint Loss Size Adjustments of Small Specimen Data. Journal of Nuclear Materials. 2004;329-333:1243-1247.

[35]   Odette GR, Rathbun HJ, Hribernik M, Yamamoto T, He M, Spätig P. NATO Science for Peace and Security Series - B, Materials Issues for Generation IV Systems, A multiscale approach to measuring and modeling cleavage fracture toughness in structural steels. Springer; 2007. p. 203-226.

[36]   Lucon E. A closer look at the fracture toughness of ferritic/martensitic steels. Journal of Nuclear Materials. 2007;367-370:575-580.

[37]   Bonadé R, Spätig P, Baluc N. Fracture toughness properties in the transition region of the Eurofer97 tempered martensitic steel. Journal of Nuclear Materials. 2007;367-370:581-586.

[38]   Sokolov MA, Tanigawa H. Application of the master curve to inhomogeneous ferritic/martensitic steel. Journal of Nuclear Materials. 2007;367-370:587-592.

[39]   Wallin K, Nevasmaa P, Laukkanen A, Planman T. Master Curve analysis of inhomogeneous ferritic steels. Engineering Fracture Mechanics. 2004;71:2329-2346.

[40]   Bonadé R. PhD Thesis Number 3405, Constitutive Behavior and Fracture Properties of Tempered Martensitic Steels for Nuclear Applications: Experiments and Modeling. Lausanne, Switzerland: EPFL; 2006.

Chapter 3

Microstructural observations

3.1 Introduction

In this chapter we study the microstructure of the tempered martensitic steels Eurofer97 and F82H-mod in order to find possible relations between microstructure, composition, heat treatment and plastic flow properties that ultimately control fracture. From the fracture mechanics point of view, the particles, namely precipitates, impurities and/or inclusions may play a key role in the fracture initiation. The microstructure of the two steels was mainly studied by means of the following techniques: Optical Microscopy, Scanning Electron Microscopy (SEM), Transmission Electron Microscopy (TEM), and Energy Dispersive X-ray spectroscopy (EDX).

3.2 Chemical composition and heat treatment

F82H-mod and Eurofer97 steels belong to the 7-9 wt% Cr (weight percent) class of tempered martensitic stainless steels. They belong to the so-called reduced activation steels, where elements like Ni were removed and Nb and Mo were replaced by W, Ta

and V, which under fusion neutron irradiation transmute to relatively short half-live isotopes and therefore show reasonable radiological properties. To quantify this concept, it must be understood that reduced-activation means that the neutron-induced radioactivity should decay to low level in about a few hundred years [1], compared to thousands of non-reduced activation steels. The compositions of the reduced-activation steels derived from the tempered-martensitic steel T91, whose composition is 9Cr1Mo0.2V0.08Nb. The 1 wt% Mo was replaced by a 2 wt% equivalent of W in F82H-mod. This content was reduced for the Eurofer97 down to 1 wt% due to the high interaction of neutrons with W as well as to reduce the ductile to brittle transition temperature. The strong carbide former Nb was replaced by Ta which was added in order to stabilize the grain size of these steels. The compositions and heat-treatments of the two F82H-mod heats as well as those of the Eurofer97 produced by Böhler are indicated in the Tables below.

Two important remarks are done here. First, the oxygen content of the two F82H-mod heats was never reported in the reference documentation. We found only two references where the oxygen content was measured for the heat 9741 [2, 3], quoting 0.0084 wt% and 0.011 wt%, respectively, for the heat 9753 we found only one measurement of oxygen content in [4] quoting 0.0074 wt%. We emphasize here that the final Ta content in Eurofer97, 0.14 wt%, is much higher than the targeted value of 0.07 wt%.

	Sample				Specification for Eurofer-97
	Plates			bar	
Thickness/Diameter	8 mm	14 mm	25 mm	⌀ 100 mm	
Certificate ref (heat, Böhler)	E83698		E83697	E83699	
C	0.12		0.12	0.12	0.09-0.12
Si	0.04		0.06	0.07	≤0.05
Mn	0.49		0.46	0.44	0.20-0.60
P	<0.005		<0.005	<0.005	≤0.005
S	0.004		0.004	0.004	≤0.005
Cr	8.93		8.90	8.97	8.50-9.50
Mo	<0.0010		0.0023	<0.001	≤0.005
Ni	0.020		0.022	0.007	≤0.005
V	0.20		0.20	0.19	0.15-0.25
W	1.08		1.07	1.10	1.0-1.2
Cu	0.0019		0.0039	0.0022	≤0.005
Co	0.006		0.006	0.004	≤0.005
Ti	0.006		0.009	0.009	≤0.01
Al	0.009		0.008	0.008	≤0.01
Nb	0.0017		0.0020	<0.001	≤0.001
B	<0.001		<0.001	<0.001	≤0.001
N	0.021		0.020	0.017	0.015-0.045
Pb	<0.0003		<0.0003	<0.0003	
Ta	0.15		0.15	0.14	0.05-0.09
O	0.006		0.0007	0.0012	≤0.01
As	<0.005		<0.005	<0.005	As+Sn+Sb+Zr
Sn	<0.005		<0.005	<0.005	≤0.05
Zr	<0.005		<0.005	<0.005	
Sb	<0.005		<0.005	<0.005	
Heat treatment					
Normalising Tempering	980°C – 27 min– air-cool		980°C – 30.6 min- air cool	979°C – 1 h 51 min - air	
Tempering	760°C – 90 min air-cool		760°C – 90 min – air-cool	739C – 3h 42 min - air	

Table 3-1: Chemical compositions and heat-treatments of Böhler Eurofer97 products, from [5].

Element	F82H-mod heat 9741 (7.5 and 15 mm plate)	F82H-mod heat 9753 (15 and 25 mm plate and welds)
C	0.09	0.09
Si	0.11	0.07
Mn	0.16	0.1
P	0.002	0.003
S	0.002	0.001
Cr	7.71	7.84
Ni	0.02	0.02
Mo	0.003	0.003
N	0.006	0.007
Cu	0.01	0.01
Co	0.005	0.003
Ta	0.02	0.04
B	0.0002	0.0002
Ti	0.01	0.004
Nb	0.0001	0.0002
V	0.16	0.19
Al	0.003	0.001
W	1.95	1.98
Fe	bal.	bal.

Table 3-2: Chemical compositions of the F82H-mod products, from [6].

Product	Heat	Normalisation	Temper
F82H-mod	9741		
7.5 mm plate		1040°C/37min	750°C/60min
15 mm plate		1040°C/38min	750°C/60min
F82H-mod	9753		
15 mm plate		1040°C/38min	750°C/60min
25 mm plate		1040°C/40min	750°C/60min

Table 3-3: Heat treatments of the F82H-mod products, from [6].

3.3   Optical Microscopy

An optical microscope equipped with a digital photographic camera is an important tool for metallographic observations. This rather simple tool, compared with electron microscopes, still has some advantages for certain applications. It allows working at low magnifications, where a large area of the specimen can be observed. This is very useful to measure the grain size, and to count large particles in order to estimate their density.

3.3.1   Specimen preparation

In order to find, observe and count particles, the surface of the specimens were prepared in the following way: first a surface of about 1 cm^2 was polished with sandpaper number 1000 to 2400 at about 300 rpm. The specimens were further polished with polishing cloth plus alcohol glycerol and DP-Spray containing 3 μm diamond particles. The final polishing was performed with colloidal alumina and the surfaces were finally cleaned with distilled water and dried with clean air. After that process, the surfaces looked like mirrors and were ready to be observed in the microscope for examination.

For some specimens an electrochemical etching step was added in order to make visible also the grain boundaries. The surface of the specimens was prepared in the following way: after performing the same procedure described in last paragraph, the specimens were introduced in a saturated solution of oxalic acid and distilled water at room temperature (10 g/ml). Using two electrodes the specimens were kept at an electrical potential of 10 Volts with respect to the solution for approximately 20 seconds by means of a direct current power source. Finally the specimens were cleaned in distilled water and alcohol. Since the acid reacts at a different rate on the grain boundaries compared to the matrix, the grain boundaries and the martensitic laths become visible.

3.3.2   Observed particles

In this subsection we compare the largest particles we could find in Eurofer97 and F82H-mod. Under the microscope we could clearly see larger particles in F82H-mod than in Eurofer97. In Eurofer97 the largest particle found was about 8 μm, while for F82H-mod the largest one was about 30 μm. In this last analysis, for both steels the same number of specimens and pictures were examined in order to avoid statistical differences when comparing them. In Figure 3-1, Figure 3-2, Figure 3-3, Figure 3-4 and Figure 3-5 we show some examples of the largest particles found in Eurofer97

and F82H-mod. A particularity of these particles is that they are composed by to different regions. In next section we show that these bicolor particles do not have the same composition in Eurofer97 and F82H-mod as determined by EDX analysis. For both steels the particles were found indistinctly in the grain boundaries and in the matrix. A clear example can be seen for the case of F82H-mod in Figure 3-6 and Figure 3-7.
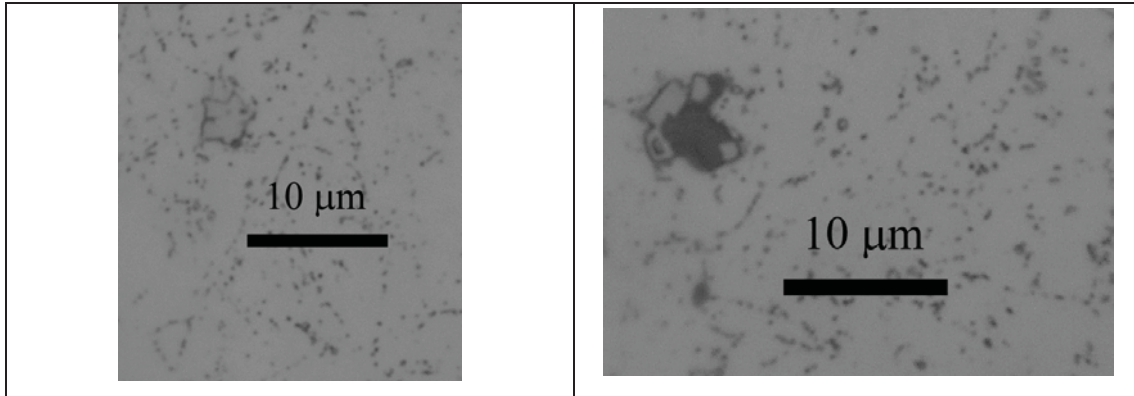

Figure 3-1: Some of the largest particles found in **Eurofer97**. Most of these particles contain two well differentiable regions. These specimens were etched.
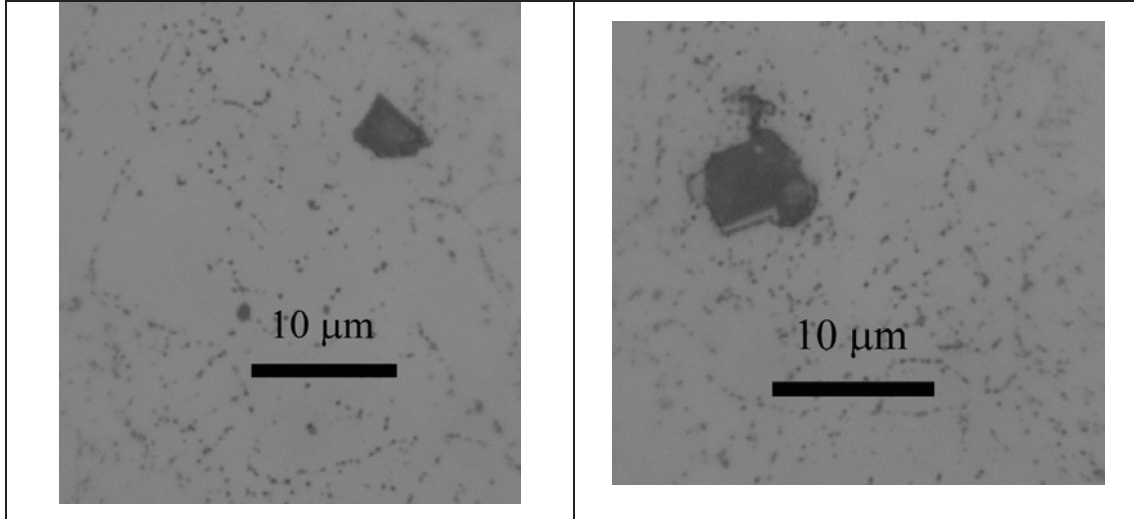
Figure 3-2: Some of the largest particles found in **Eurofer97**. Etched specimens.
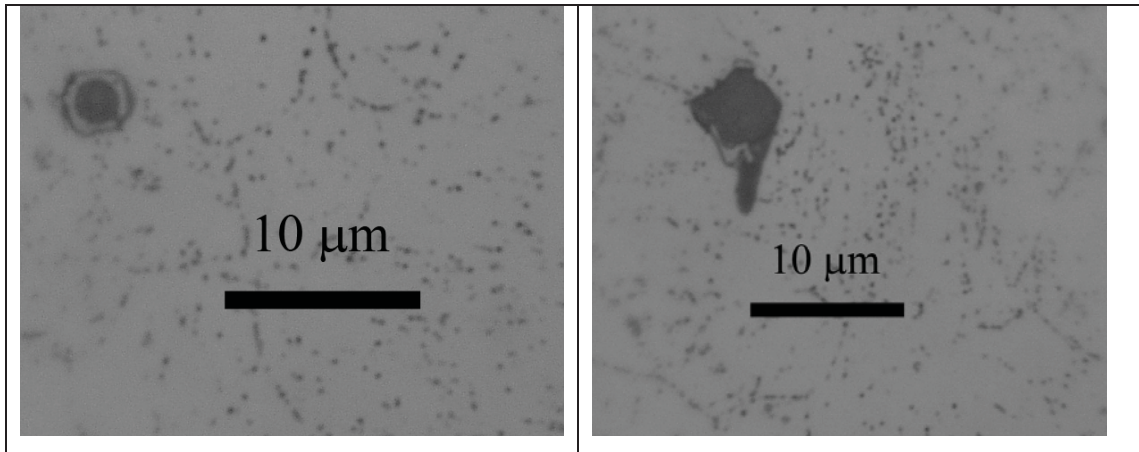
Figure 3-3: Some of the largest particles found in **Eurofer97**. Etched specimens.

Figure 3-4: Some of the largest particles found in **F82H-mod**. The scratch below the left particle was intentionally introduced in order to find again the same particle in the scanning electron microscope and analyze its composition. These specimens were not etched.

Figure 3-5: Bicolor particle in **F82H-mod** along with the grain boundaries and laths.

3.3.3   Particles density

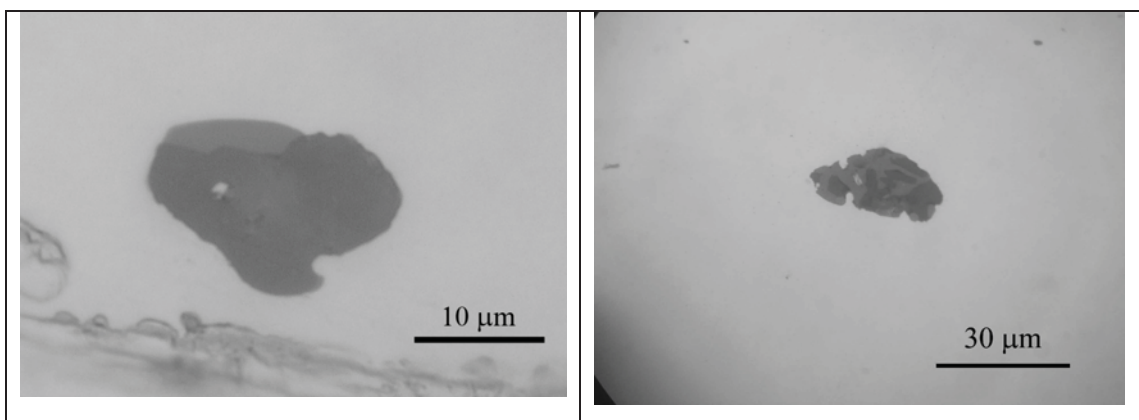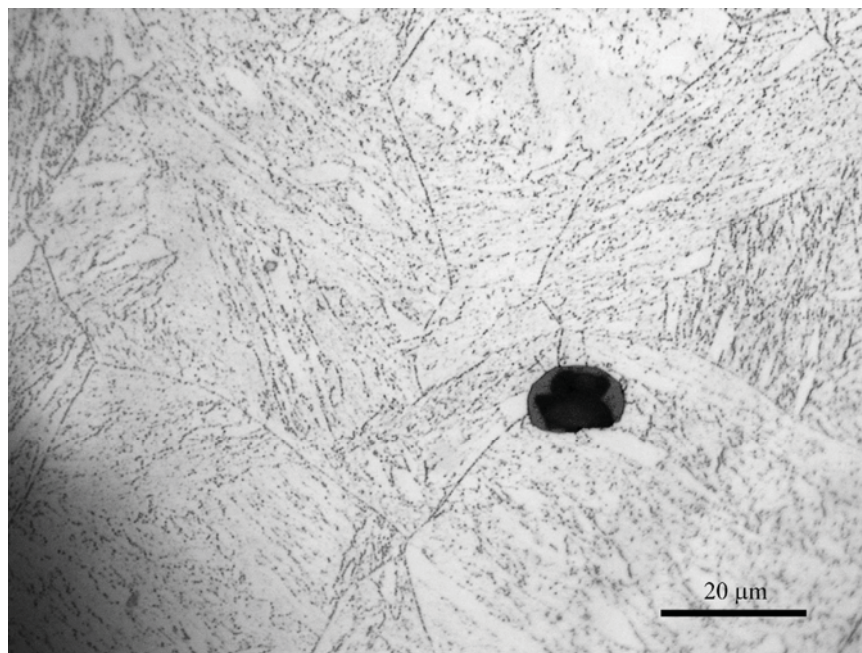By taking pictures on the surface of a specimen at different locations and counting the number of particles that are larger than a certain size, it is possible to estimate the number of particles per unit of area. This quantity is also called surface density (ρ_S). This estimation is done by performing the average of the counted particles per picture and dividing by the area of the picture. The number of pictures used to calculate each average value was between 20 and 50 depending on the magnification. The pictures were taken on not-etched specimens so that the grain boundaries do not complicate the image and the counting procedure. Using different magnifications the minimum particle size counted can be changed. Below we present the results obtained for F82H-mod and Eurofer97 along with the standard deviation:

- Particles counted larger than 1.5 μm (± 20%)

    F82H-mod: $\rho_S = (12.8 \pm 1.4)$ particles / mm^2

    Eurofer97:   (not determined)

- Particles counted larger than 2.5 μm (± 20%)

    F82H-mod: $\rho_S = (20.9 \pm 2.7)$ particles / mm^2

    Eurofer97: $\rho_S = (10.1 \pm 2.5)$ particles / mm^2

- Particles counted larger than 3.5 μm (± 20%)

    F82H-mod: $\rho_S = (24.8 \pm 5.2)$ particles / mm^2

    Eurofer97:   (not determined)

In order to calculate the number of particles per unit of volume (or volume density, ρ_V) based on the surface density of particles, it is necessary to know the particle size distribution and the particle shape. Large particles have a higher probability to appear in the examined plane than small particles. The following equation relates the two mentioned densities.

$$\rho_V = c \frac{\rho_A}{d_{av}} \qquad\qquad (3.1)$$

d_{av} is the average particle size and c is a constant close to one that depends on the particle size distribution and on the particles shape. A number of works studying the relation between particle size distribution and shape can be found in the literature, for instance [7, 8].

The number of particles per unit *area* in F82H-mod is larger than in Eurofer97. In principle we cannot ensure that there is such a difference in the number of particles per unit *volume* because the particle distribution is not the same in both materials. For instance in F82H-mod the maximum particle size is about 4 times larger than in Eurofer97. Nevertheless the average particle size is not that different based on our observations among the particles larger than 2.5 µm: we could roughly estimate that the average size of these mentioned particles is for Eurofer97 between 2.5 and 3.5 µm; and for F82H-mod between 2.5 and 5 µm. Using these last values along with Eq. (3.1) with c=1 we can assess for both materials the order of magnitude of the number of particles larger than 2.5 µm per unit volume: around 3000 to 4000 particles / mm3 for Eurofer97 and around 4000 to 8000 particles / mm^3 for F82H-mod.

3.3.4   Grains

A typical microstructure of tempered martensitic steels results from the applied final heat-treatments. Such a microstructure is illustrated in Figure 3-5, Figure 3-6 and Figure 3-7 for F82H-mod and in Figure 3-8 for Eurofer97. The prior austenite grain boundaries (PAG) are visible. The PAG of the two steels were characterized using the mean interception length technique [9]. A significant difference in PAG size between them was found. Indeed, the average PAG size of F82H-mod is about 70 µm, while in Eurofer97 it is about 10 µm. The prior austenite grain sizes taken from the following reference [10] is consistent with our observations. A possible reason for the difference in the PAG size between the two steels is proposed in a following section.
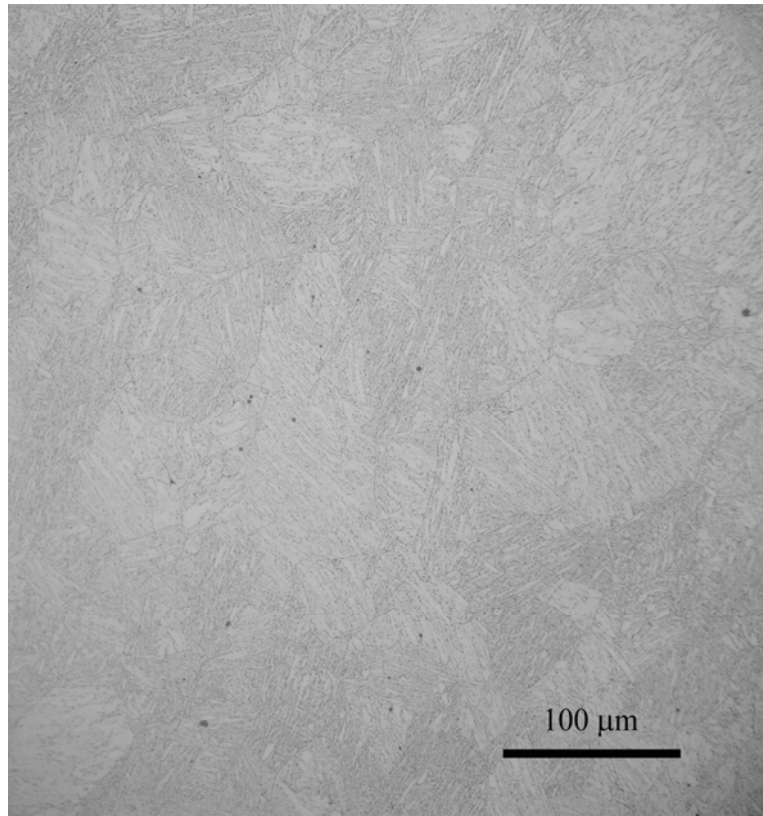
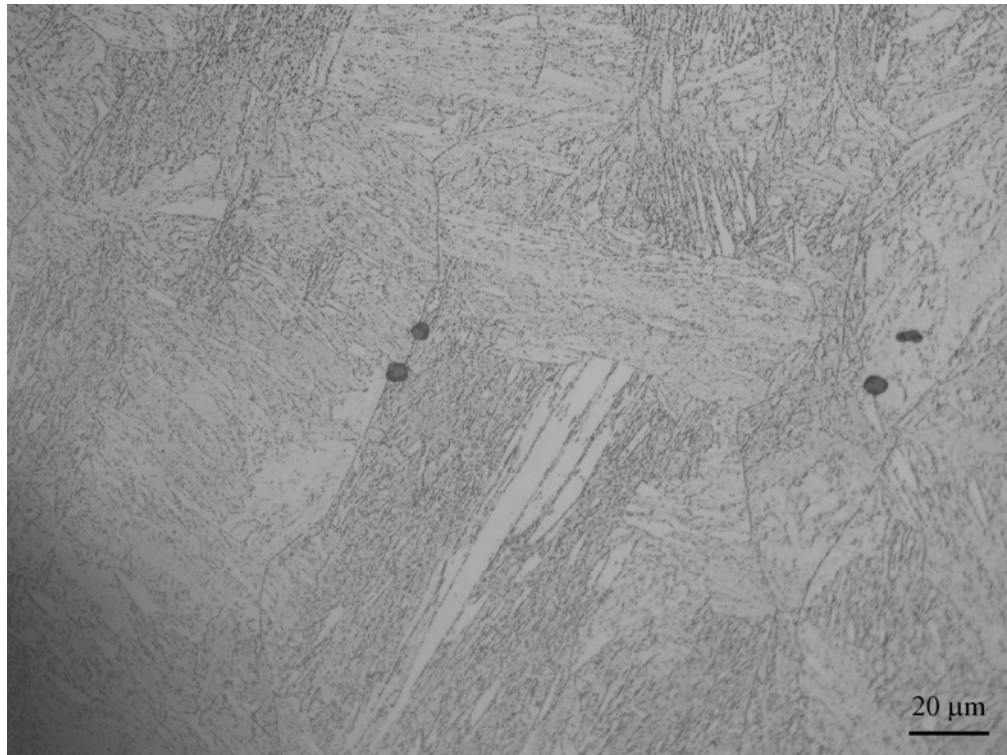**Figure 3-6**: Grains and laths in **F82H-mod**.

Figure 3-7: Grains and laths in **F82H-mod**. Particles appear on the prior austenitic grain boundaries and also inside the grains.
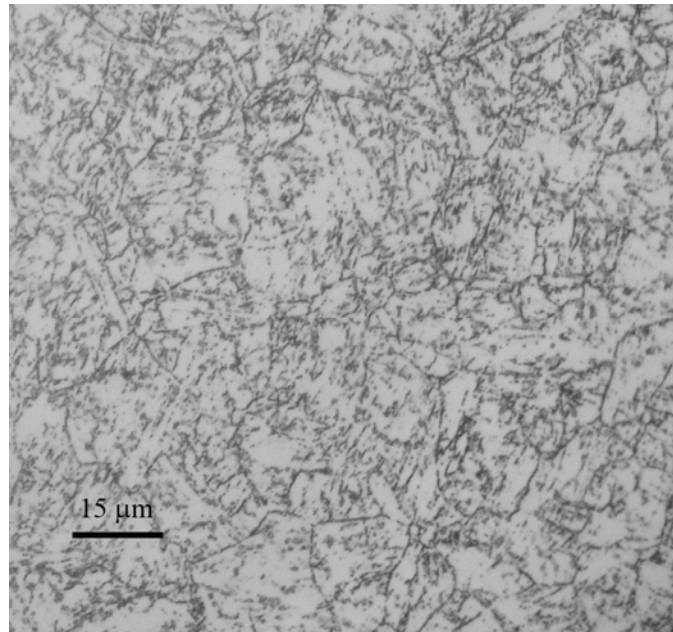
Figure 3-8: Grains and laths in **Eurofer97**.

3.4   Scanning Electron Microscopy

Scanning Electron Microscopy is a technique to image sample surfaces by scanning it with a high-energy beam of electrons. This electron beam is focused at different positions on the surface of the observed specimen, while the backscattered or secondary emitted electrons are detected and counted. The different intensity measured at each position creates contrast in the digital image. The electrons interact with the atoms that make up the sample producing signals that contain information about the sample's surface topography, composition and other properties such as electrical conductivity.

Backscattered electrons consist of high-energy electrons originating from the electron beam, which are reflected or back-scattered out of the specimen interaction volume by elastic scattering interactions with specimen atoms. Since heavy elements (high atomic number) backscatter electrons more strongly than light elements (low atomic number), and thus appear brighter in the image, backscatter electrons are used to detect contrast between areas with different chemical compositions. This was the SEM operating mode used in the following pictures in order to identify particles.

Characteristic X-rays are also emitted when the electron beam removes an inner shell electron from the sample, causing a higher energy electron to fill the shell and release energy. These characteristic X-rays are used to identify the composition and measure the abundance of elements in the sample. This technique is called energy dispersive X-ray spectroscopy.

3.4.1   Specimen preparation

The specimens were prepared in the same way as described in the last section for the optical microscope.

3.4.2   Particles in Eurofer97

In Eurofer97 three kinds of particles were clearly identified.

- Bicolor particles in Eurofer97: Composed of two regions, one rich in Aluminum and Oxygen (probably Al_2O_3 since it is the only known common aluminum oxide), and the other rich in Manganese and Sulfur. Sometimes Ti and V also appeared. Particles up to 6 μm were found.
- Silicates: Particles rich in Silicon and Carbon. They have usually an elongated shape. Up to 7 μm.
- Tantalum Carbides: Particles rich in Ta and C. Plenty of this kind of particles were found. The largest ones were about 1 μm.

Examples of these particles along with the EDX analysis are shown in the following figures.
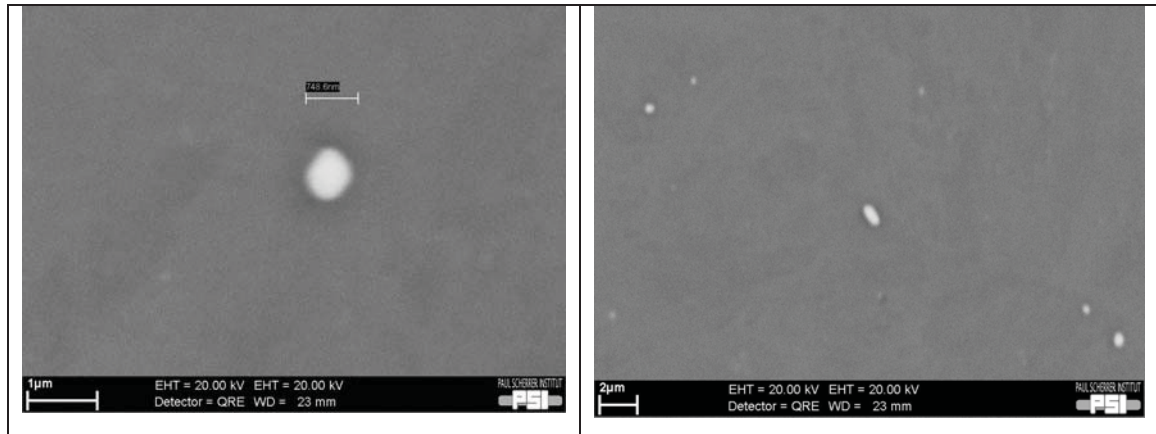
Figure 3-9: Typical big Tantalum Carbides. The light contrast of these particles indicates a large intensity of backscattered electrons, consistent with the large atomic number of Ta. An EDX analysis of the left particle is shown in next figure.
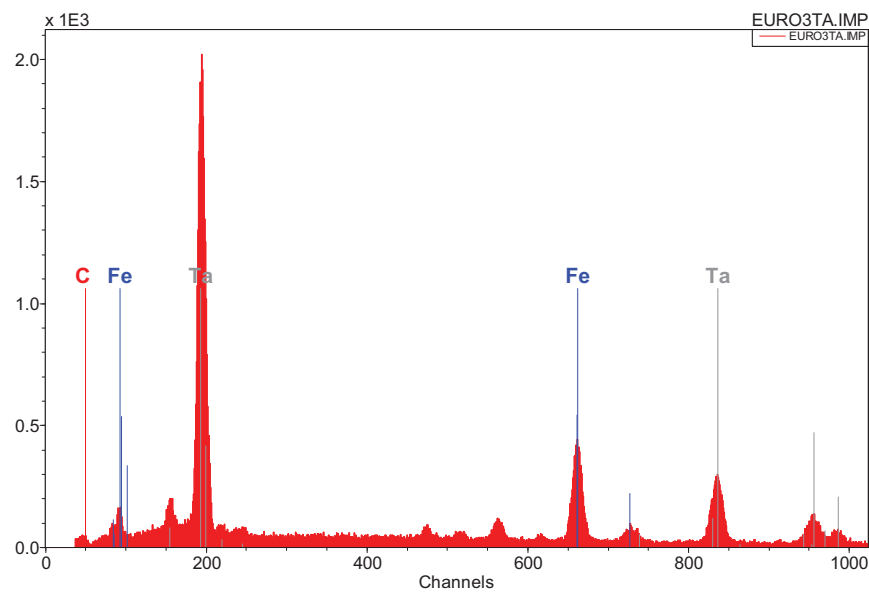
Figure 3-10: This EDX spectrum corresponds to the left Tantalum Carbide shown in the previous figure. The Ta peak is clearly visible. The Carbon peak is not very pronounced due to its low energy characteristic X-ray which makes the detection difficult and inefficient.
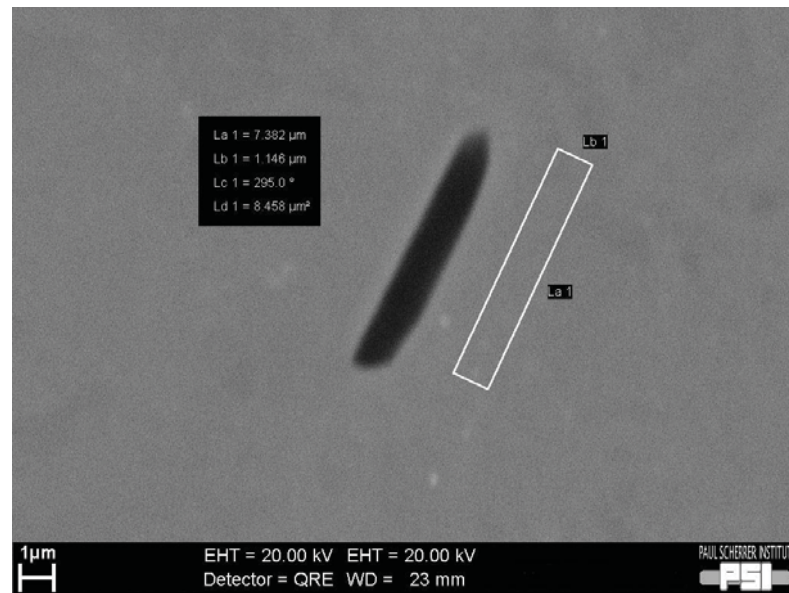
Figure 3-11: Silicate particle. The EDX analysis of this particle is shown in next figure.
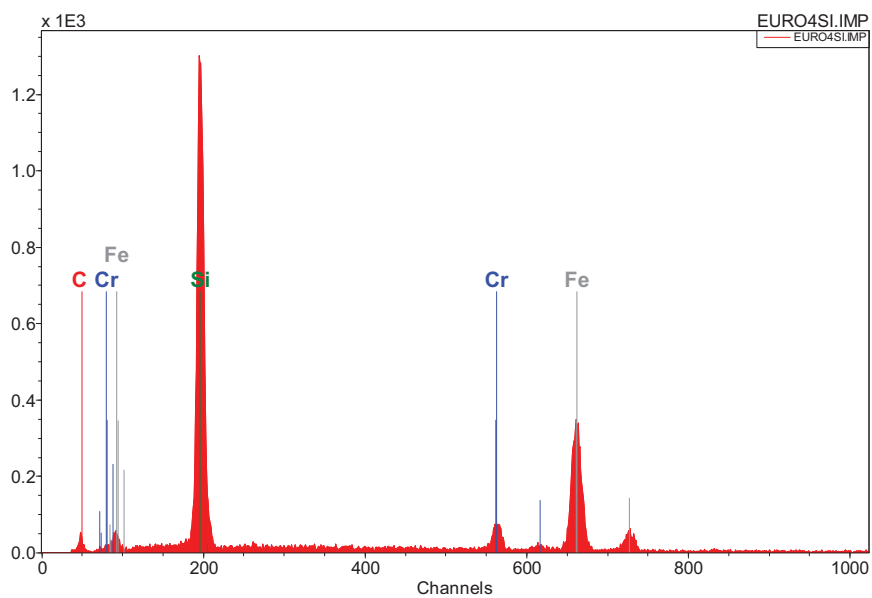
Figure 3-12: EDX analysis of the Silicate Particle of the previous picture. The Silicon peak is clearly visible along with Cr, Fe which comes from the matrix and Carbon.
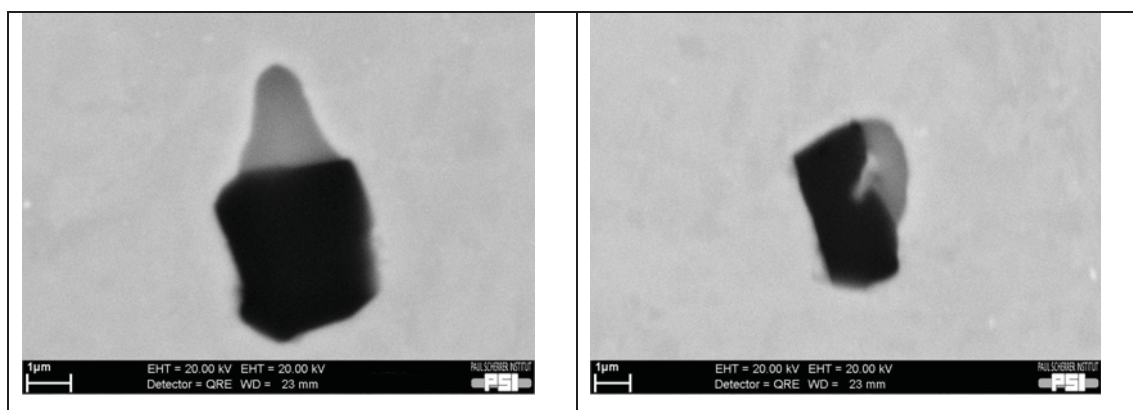
Figure 3-13: Typical bicolor particles. In the next two figures, the typical EDX spectra of the light and dark region of bicolor particles are shown.
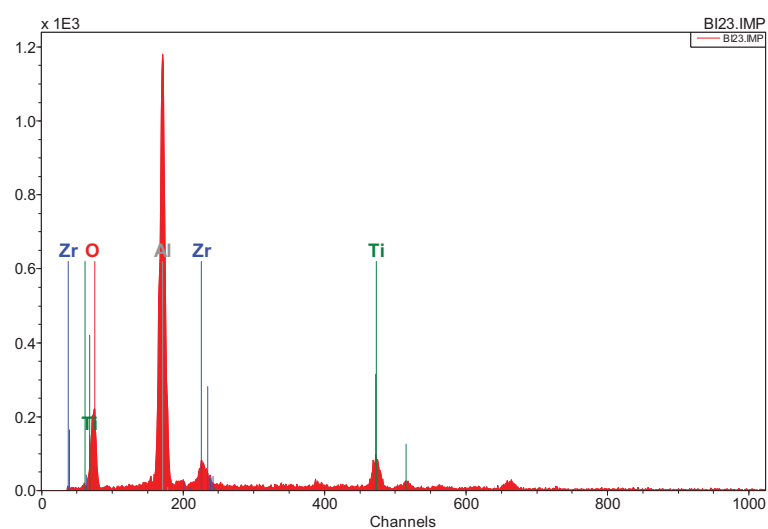
Figure 3-14: EDX composition in the dark region of a bicolor particle, indicating clearly the presence of Oxygen and Aluminum.
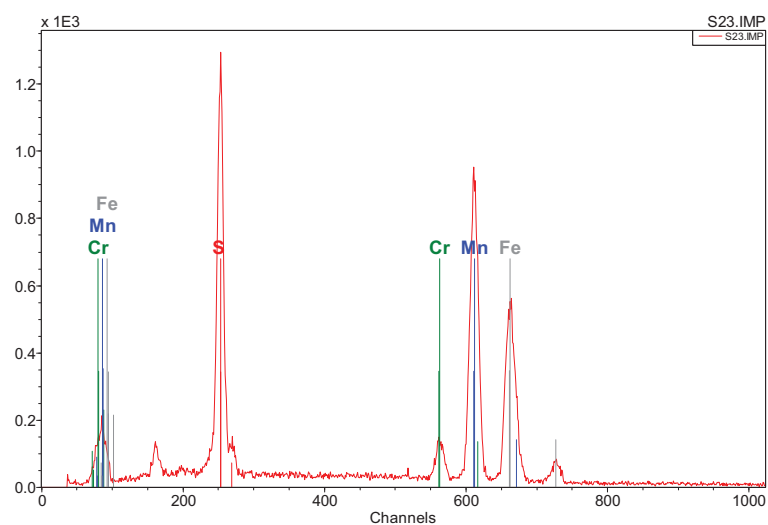
Figure 3-15: EDX composition in the light region of a bicolor particle. Typically this region is rich in Sulfur and Manganese.

3.4.3   Particles in F82H-mod

In F82H-mod two kinds of particles were clearly identified.

- Bicolor particles in F82H-mod: Composed by two regions, one rich in Aluminum and Oxygen (probably Al_2O_3), and the other rich in Tantalum and Oxygen. Sometimes Ti and V also appeared. Particles up to 25 μm were found.

- Silicates: Particles rich in Silicon and Carbon. They have usually an elongated shape. Found with a length of up to 15 μm.

Note that no Tantalum Carbides were found in F82H-mod. Also note that the bicolor particles are not the same in Eurofer97 and in F82H-mod.

Examples of such particles along with the EDX analysis are shown in the following figures.
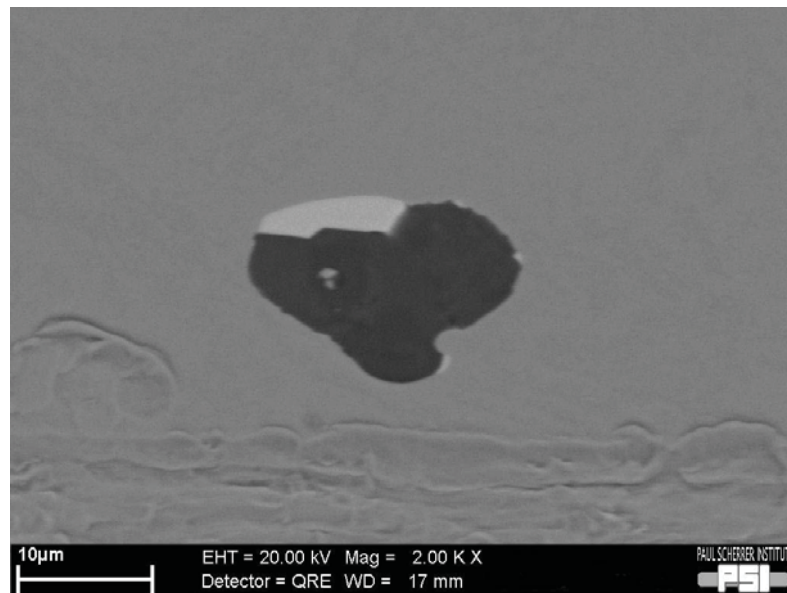
Figure 3-16: This 20 microns big bicolor particle was first identified with the optical microscope. With the help of the intentionally introduced scratch below of the particle, it was possible to find it again with the SEM. The dark and the white regions are analyzed by EDX in the next two figures.
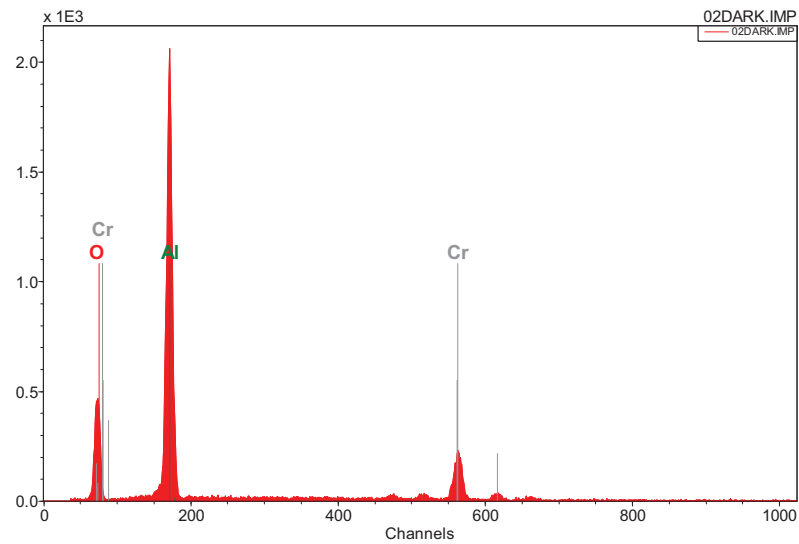
Figure 3-17: EDX spectra of the dark region in the bicolor particle of last figure. The peaks of Aluminum and Oxygen are clearly visible.
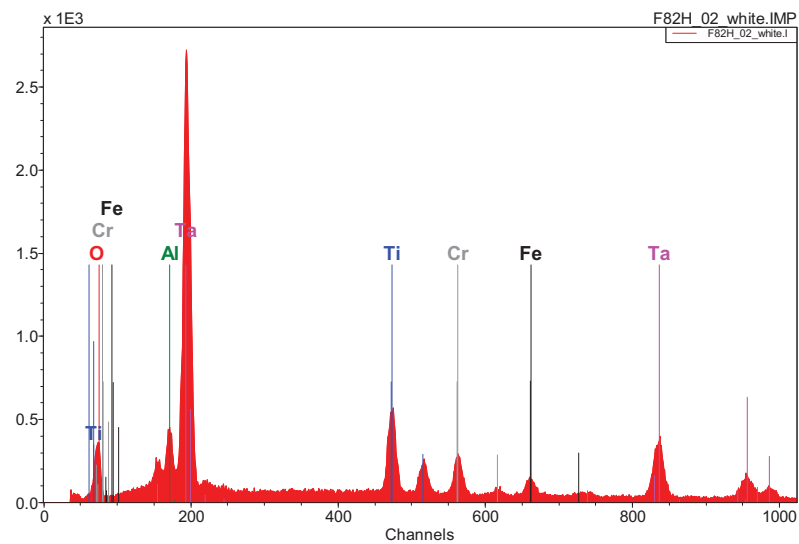
Figure 3-18: Here the light region of the bicolor particle mentioned before. In the white region the bicolor particles in F82H-mod are rich in Tantalum and Oxygen.
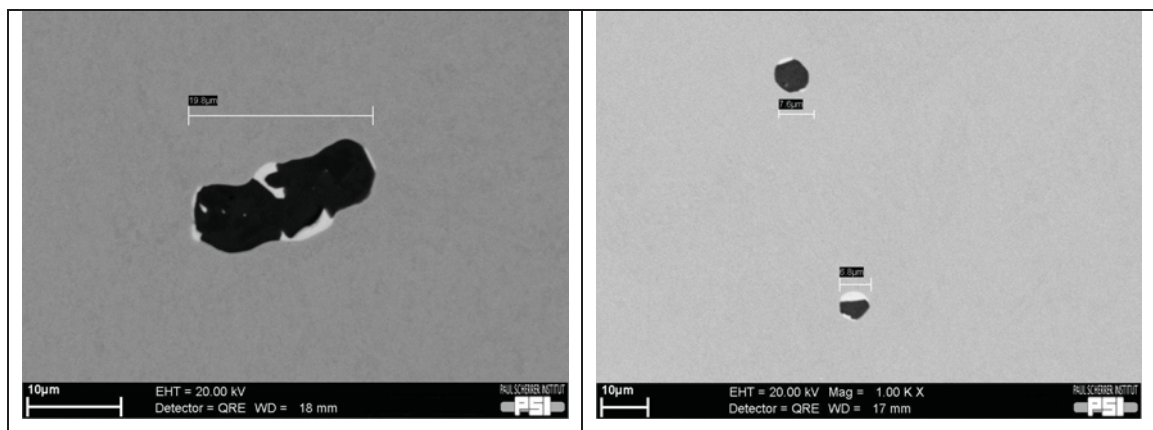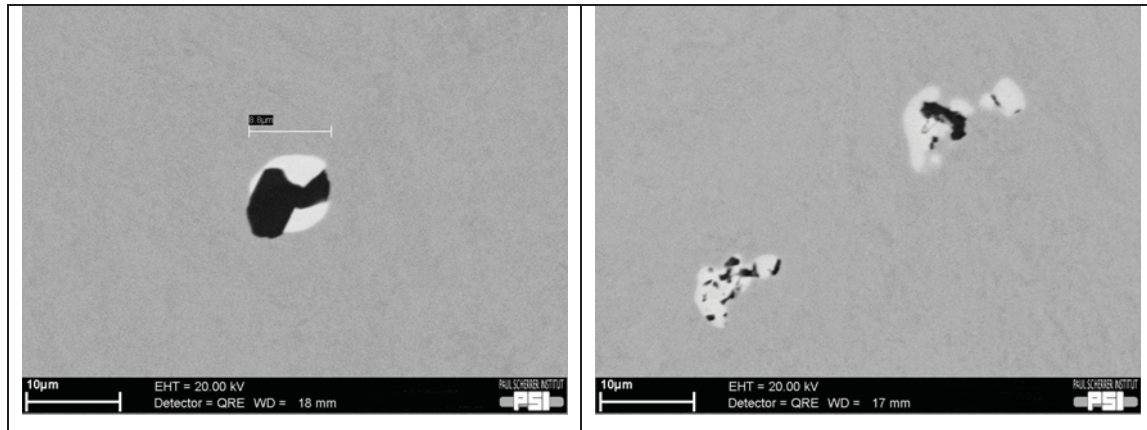
Figure 3-19: Typical large bicolor particles found in F82H-mod.

3.5   Transmission Electron Microscopy

Transmission electron microscopy (TEM) is a microscopy technique whereby a beam of electrons is transmitted through an ultra thin specimen, interacting with the specimen as they pass through. An image is formed from the interaction of the electrons transmitted through the specimen, which is magnified and focused by an objective lens and onto an imaging device, such as a fluorescent screen [11]. On the one hand, this technique has the great advantage that extremely high resolutions can be obtained. On the other hand, there are also some disadvantages for instance: the specimen must have a maximum thickness of about 100 nanometers in order to be semi-transparent to the electrons, only an extremely small volume of material can be examined, specimen preparation is difficult and may introduce changes in the original microstructure, and some damage may also occur due to the high energy of the electrons.

3.5.1   Specimen preparation

The specimen consists in a 3mm diameter disc with a thickness of about 150 microns with an electro-polished region in the middle of the disc where the specimen thickness reaches less than 100 nm. Eurofer97 and F82H are ferritic steels and thus ferromagnetic at room temperature. This magnetism makes more difficult the TEM

alignment procedure, which is needed for observation, because the electrons are not only deviated by the magnetic lenses but also by the specimen. In order to minimize this problem the amount of ferromagnetic material was minimized. Since austenitic steel is not magnetic, a hole with a diameter of 1.3 mm was produced in the middle of a 3 mm austenitic steel disc. A 1.3 mm disc of the ferromagnetic material to be examined was inserted and glued in the hole of the 3mm aluminum disc. Finally the specimen was electro polished by means of a TenuPol-5 equipment from Struers. The specimen is polished from both sides simultaneously in order to minimize deformation. When the perforation appears the polishing is automatically stopped by an infrared detector system.

3.5.2 General microstructure

Typical tempered martensitic structures were observed in Eurofer97 and F82H-mod samples. For both F82H-mod and Eurofer97 steels, the typical thickness of the remaining laths after the tempering is about 0.5-0.7 μm, as revealed by TEM technique and shown in Figure 3-20 and Figure 3-21. Small equiaxed subgrains were also observed in some regions of the specimens that have a typical diameter smaller than 1 μm. For Eurofer97 steel, it appears that most of the volume contains small equiaxed subgrains having a size of around 0.7 μm. Elongated martensitic laths are scarcer than in F82H-mod.

Figure 3-20: Typical TEM images for F82H-mod.

Figure 3-21: Typical TEM images for Eurofer97.

3.5.3   Particles

Using SEM, Tantalum carbides were identified in Eurofer97 but not in F82H. With this last technique, it was only possible to observe and analyze particles larger than about 200 nanometers. With the TEM it was possible to identify and analyze carbides by EDX as small as about 10 nanometers. Again a great amount of Tantalum carbides could be found in Eurofer97 while none of them were found in F82H-mod. For the EDX analysis of the particles we chose particles that were as close as possible to the TEM specimen central hole in order to minimize the background signal from the Iron and Chromium matrix. We did not have this problem with the SEM because the particles are large enough so that the electrons do not penetrate more than the particle deepness and therefore the characteristic X-rays correspond to the ones generated in the particle. On the contrary, with the TEM the electrons are transmitted through the specimen and, if the particle is smaller than the specimen thickness, some matrix background signal is unavoidable. In Figure 3-22 and in Figure 3-23 typical TEM images of particles found and analyzed in F82H-mod and Eurofer97 are shown.

Figure 3-22: Typical particles found and analyzed in F82H-mod.
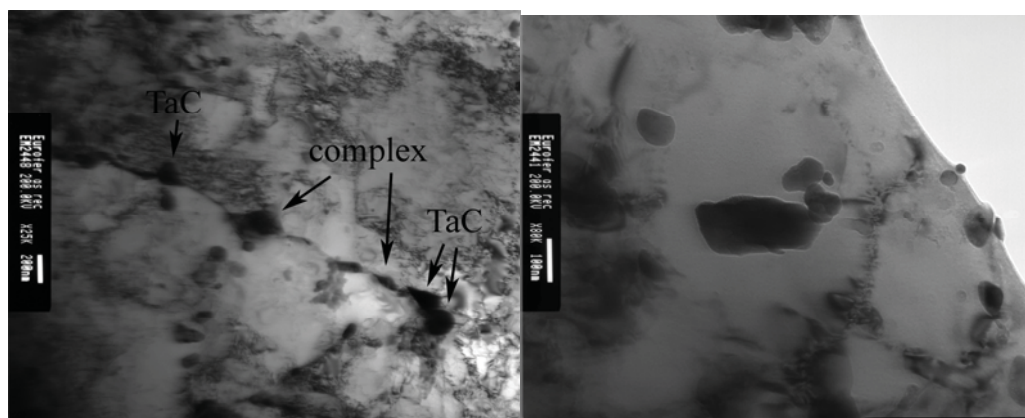
Figure 3-23: Typical particles found and analyzed in Eurofer97.

3.6 Discussion

In Eurofer97, it was found that the alloying element Tantalum formed small dispersed carbides. These carbides are the main reason for adding this alloying element to reduced activation steels in order to stabilize the grain size. This mechanism is based on the small carbides which act as pinning points for the grains preventing them to grow as easily as in a carbide free matrix. The maximum size of the Tantalum carbides was found to be about 1 micron. We remark that no Tantalum oxides where found in Eurofer97 indicating that the Tantalum formed only small carbides in this steel.

In F82H-mod, we found out that the alloying element Tantalum did not form the intended small dispersed carbides. Instead, it formed big oxides up to about 50 microns in size. The oxides were found in complex inclusions mainly formed by two well differentiated regions: Tantalum oxide in one region of the particle and Aluminum oxide in the other region. The lack of small dispersed Tantalum carbides in F82H-mod is likely to be the reason why F82H-mod has bigger prior austenitic grains than Eurofer97.

Another consequence of the different behavior of the Tantalum in both steels is the presence of the big bicolor oxides found in F82H-mod. This big particles could explain why some unexpected low toughness values can be found in F82H-mod above -40 ºC (for instance the low K_J values tested in [12]) which do not appear in Eurofer97.

A possible reason for the different behavior of Tantalum in both steels may be due to the different content of impurities. Aluminum is a significantly stronger oxide former than Tantalum, the free energy of formation of Aluminum oxide is about 50 kcal / mole O_2 lower than Tantalum oxide [13]. Since the Aluminum content of Eurofer97 is about 8 times higher than in F82H-mod it is likely that for Eurofer97 there was enough Aluminum to capture most of the Oxygen and form Aluminum oxide. In F82H-mod we also found Aluminum oxide particles but since the Aluminum content was lower and the oxygen content higher, in this case the Aluminum content was not enough to capture all the oxygen. Thus, the remaining oxygen combined with Tantalum forming the big Tantalum oxides.

Note that 54 grams of Aluminum plus 48 grams of Oxygen are needed in order to form 102 grams of Al_2O_3. The different element weight percent contents given in Section 3.2   show that in 1 kg of F82H-mod there is only 1 gram of Aluminum and 7.4 grams of Oxygen, while in 1 kg of Eurofer97 there are 8 grams of Aluminum and only 0.7 grams of Oxygen.

3.7   References

[1]   Klueh RL. Reduced-activation bainitic and martensitic steels for nuclear fusion applications. Current Opinion in Solid State and Materials Science. 2004;8:239-250.

[2]   Schirra M, Heger S, Falkstein A. Wissenschaftliche Berichte. 1999;FZKA-6265.

[3]   Report STA/LMS/98-RT 3650. Centre d'étude de recherches sur les matériaux; 1998.

[4]   Tanigawa H, Sawahata A, Sokolov MA, Enomoto M, Kueh RL, Kohyama A. Effects of Inclusions on Fracture Toughness of Reduced-Activation Ferritic/Martensitic F82H-IEA Steels. Materials Transactions. 2007;48:570-573.

[5]   Rensman J. NRG Irradiation Testing: Report on 300 ºC and 60 ºC Irradiated RAFM Steels. 2.5 and 10 dpa neutron irradiated Eurofer97 Plate, HIPed Powder, HIP diffusion welds, TIG welds, EB welds, F82H and NRG 9Cr lab heats. 20023/05.68497/P. Petten; 30 August 2005.

[6]   van_Osch EV, van_Hoepen J, Boskeljon J, Rensman J. Tensile Properties of 2.5 dpa 300 ºC Neutron Irradiated RA FM plate, powder HIP and EB and TIG weld. F82H-mod, JLF-1, JLF-1B,ORNL-3791. Final report EBP 95-98 programme, subtask SM 1.2.2. 20023/99.26704/P. Petten; 20 November 2000.

[7]   Underwood EE. Quantitative Stereology. Addison-Wesley Publ. Co., 1970.

[8]   Umezaki A, Enomoto M. Estimation of number of precipitate particles per unit volume from measurements on polished specimen surfaces: Computer simulation. ISIJ international ISSN 0915-1559. 2000;40:1142-1148.

[9]   ASTM. E 112 - 96 (Reapproved 2004). Standard Test Methods for Determining Average Grain Size; 2004.

[10]   Fernández P, Lancha AM, Lapeña J, Hernández-Mayoral M. Metallurgical characterization of the reduced activation ferritic/martensitic steel Eurofer'97 on as-received condition. Fusion Engineering and Design. 2001;58-59:787-792.

[11]   Williams DB, Carter CB. Transmission Electron Microscopy, 2nd rev. ed., 2008.

[12]   Sokolov MA, Tanigawa H. Fusion Materials Semiannual Progress Report for the period ending December 31, 2006, DOE-ER-0313/41. p. 85-97.

[13]   Perry RH. Perry's Chemical Engineers' Handbook, Sixth Edition. McGraw-Hill, 1987.

Chapter 4

Mechanical tests

In this chapter we present the experimental procedures of the mechanical tests and fracture results obtained for the reduced activation tempered martensitic steel Eurofer97 along with an extensive analysis of the fracture toughness data in terms of the ASTM E1921 standard that was introduced in Chapter 2: the Master Curve modeling the toughness-temperature behavior in the ductile to brittle transition region. The experimental results presented in this chapter will be used in next chapter to compare them with the finite element simulations and to validate a local approach model to predict quasi-cleavage fracture.

4.1 Experimental procedures

Three kinds of specimens were tested in this work: standard round tensile specimens, notched tensile specimens and pre-cracked fracture specimens. All Eurofer97 specimens were machined from the 25 mm thick plate, heat E83697, produced by Böhler AG. Most of the experiments presented in this work were carried out with a Schenck RMC100 electro-mechanical testing machine equipped with a load cell calibrated up to 20kN. An MTS hydraulic testing machine, with a higher load

capacity, was used to pre-crack and test the fifteen 0.87T C(T) specimens that failed at up to about 65 kN. In order to control the temperature during the tests, a thermally isolated temperature chamber was mounted around the load train. Temperature control was provided by a PID controller along with a regulated liquid nitrogen flow.

4.1.1   C(T) specimens

The experimental procedure used to measure fracture toughness was based on the ASTM standard E 1820 [1]. Standard compact tension specimens, called C(T) specimens, were produced in three sizes that correspond to the following specimen thicknesses: 0.87T (B=22 mm), 0.35T (B=9 mm), 0.18T (B=4.5 mm). The specimen shape and relative dimensions are shown in Figure 4-1.

Most of the specimens were cut in the L-T orientation. Only eight 0.35T specimens tested at -120 ºC were cut in the T-L orientation. No significant orientation effect could be observed. The load line displacement was measured by compliance correcting the load-train displacement. A provision to insert a clip gage in the front face of the 0.35T specimens tested at temperatures above -100 ºC was machined to accurately measure the crack mouth opening displacement during the test. This allows a direct comparison with the finite elements simulations. The pre-cracks were introduced by fatigue at room temperature. The temperature of the specimens during the test was monitored with an attached thermocouple. The standard nine point crack length measurement was performed in order to determine the initial crack length ratio a/W. This measurement was performed on the broken pieces of the specimens after testing using an optical microscope. The stress intensity factor K_J was calculated in the standard way, Eq. (4.1).

$$K_J = \sqrt{\frac{(J_e + J_{pl})E}{1-\nu^2}}$$
(4.1)

Being E the Young modulus and ν the Poisson ratio. The elastic J-integral was calculated as follows:

$$J_e = \frac{K_{el}^2(1-v^2)}{E} \tag{4.2}$$

$$K_{el} = \frac{P}{B\sqrt{W}} f\left(\frac{a}{W}\right) \tag{4.3}$$

Where P is the breaking load and:

$$f\left(\frac{a}{W}\right) = \frac{\left(2+\frac{a}{W}\right)\left(0.886 + 4.64\frac{a}{W} - 13.32\left(\frac{a}{W}\right)^2 + 14.72\left(\frac{a}{W}\right)^3 - 5.6\left(\frac{a}{W}\right)^4\right)}{\left(1-\frac{a}{W}\right)^{3/2}} \tag{4.4}$$

The plastic J-integral was calculated as follows:

$$J_{pl} = \frac{\eta A_{pl}}{Bb_0} \tag{4.5}$$

Where $b_0 = W - a$ is the initial ligament length, $\eta = 2 + 0.522 b_0/W$, and A_{pl} is the plastic area shown in Figure 4-2.
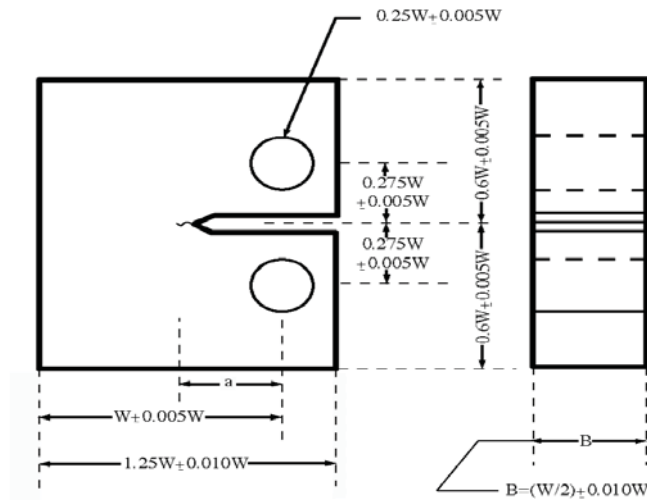
Figure 4-1: Standard C(T) specimen.
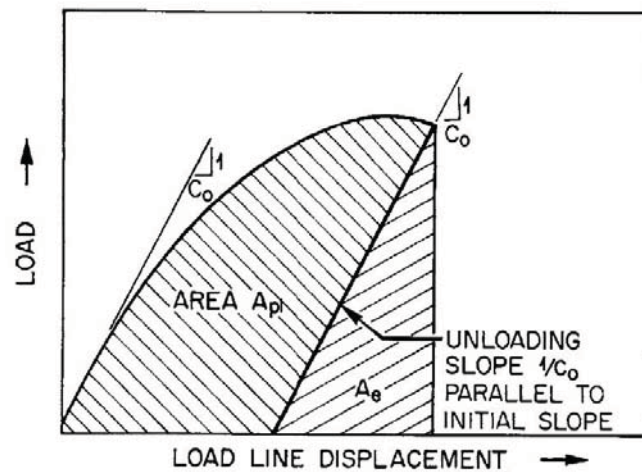
Figure 4-2: Definition of the plastic area for J_{pl} calculations.

4.1.2   Notched tensile specimens

A series of tests of notched tensile specimens were carried out. The notched specimen diameter was 6 mm with a 1.5 mm deep notch in the middle of the gage length, the notch root radius was 0.4 mm (Figure 4-3). The tests were also performed at low temperature and the cross-head velocity of the machine was constant, equal to 0.1 mm/min. In the following, we report the load–deflection curves for which the displacement δ corresponds to the opening of the notch measured with a clip gage whose knives were symmetrically positioned at 5mm on each side of the notch plane. The results will be presented only in the next chapter along with the corresponding finite element simulations to study the stress fields around the notch at the onset of fracture.
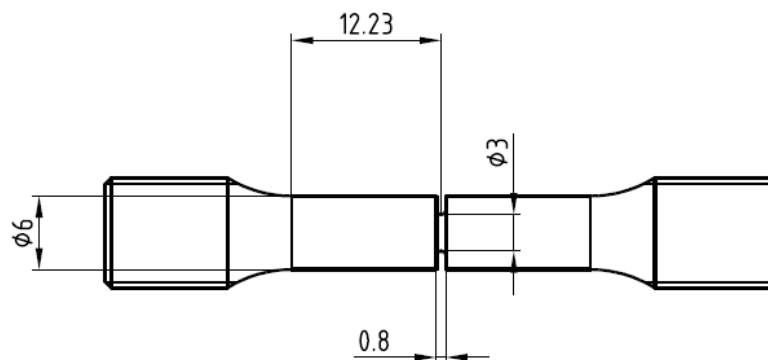
Figure 4-3: Notched tensile specimen (dimensions in millimeters).

4.1.3   Standard tensile specimens

Normal round tensile tests were performed with four main purposes. First, to obtain the true stress – true plastic strain curve, also called plastic flow curve, which is part of the material constitutive properties needed for the finite element simulations. Second, to obtain the yield stress as a function of temperature used in ASTM fracture specimens size limit criteria (see below). Third, to validate the finite element simulation of a complete tensile test including the necking phenomenon. And finally, to validate the σ^*-V^* brittle fracture local approach model for these kind of specimens. Two sizes of round specimens were used. Namely 2.4 mm in diameter with 13.2 mm gauge length and 3 mm diameter with 18 mm gauge length.

The displacement of the specimen was measured by compliance correcting the load-train displacement and by directly measuring the displacement with a clip gage attached on the specimen. The experimental results will be presented and compared to the finite element simulations in the next chapter.
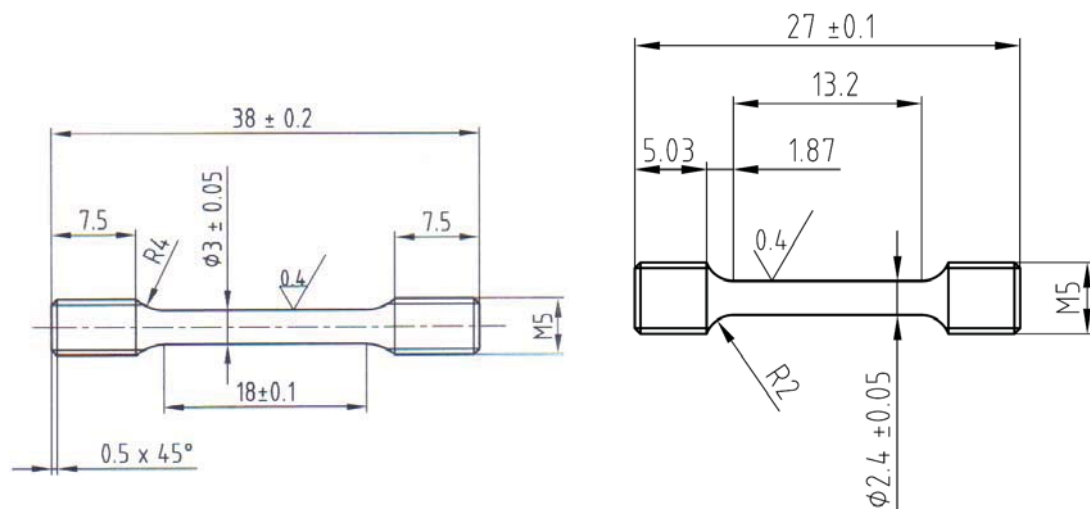
Figure 4-4: Round tensile specimen (dimensions in millimeters).

4.2   C(T) specimens experimental results

In this section, the C(T) fracture toughness dataset of Eurofer97 is presented. Three different sizes of Eurofer97 specimens have been tested in the temperature window -196 ºC to -40 ºC, making a total of 187 experiments. As mentioned in the objectives described in the Chapter 2, the fracture tests performed in this study have been done in order to extend the previously existing database produced by Bonadé with subsized 0.18T and 0.35T C(T) specimens [2] over the temperature range -148 to -100 °C. So, additional tests on the lower shelf at -196 °C as well as at -80, -60, -50 and -40 °C have been carried out. Bigger specimens, 0.87T C(T), were used in the upper transition region. In the following table, the number of experiments performed at each temperature and for each specimen size is indicated.

	0.18T (B=4.5 mm)	0.35T (B=9mm)	0.87T (B=22mm)
-196 ºC	8	5	
-148 ºC		6	
-138 ºC		12	
-129 ºC		15	
-120 ºC	13	27	
-100 ºC	38	33	
-80 ºC		3	3
-60 ºC		11	6
-50 ºC		1	4
-40 ºC			2

Table 4-1: Number of C(T) fracture toughness tests performed on Eurofer97 at each temperature and with each specimen size.

In Figure 4-5 we present the experimental results in a toughness versus temperature plot. Along with the data points, the standard ASTM E1921 specimen toughness capacity limits [3] (Eq. (4.6) with M=30) for each specimen size are also plotted. This limit reads:

$$K_{Jc\_limit} = \sqrt{\frac{E b_0 \sigma_{ys}}{M(1-\nu^2)}} \qquad (4.6)$$

In Figure 4-5, we can see that most of the data falls below the standard limits. Note that according to the ASTM E1921 standard, the data that falls above remains useful and is used, as recommended, in a censoring procedure. As expected for fracture toughness tests, the data presents an important amount of scatter which is especially evident above -100 ºC. Another remarkable feature of the data is the very strong size effect which is clearly observed in the upper transition. All the experimental data together is analyzed in next sections in terms of the master curve approach and in Chapter 5 by means of finite elements simulations and a local approach to cleavage.
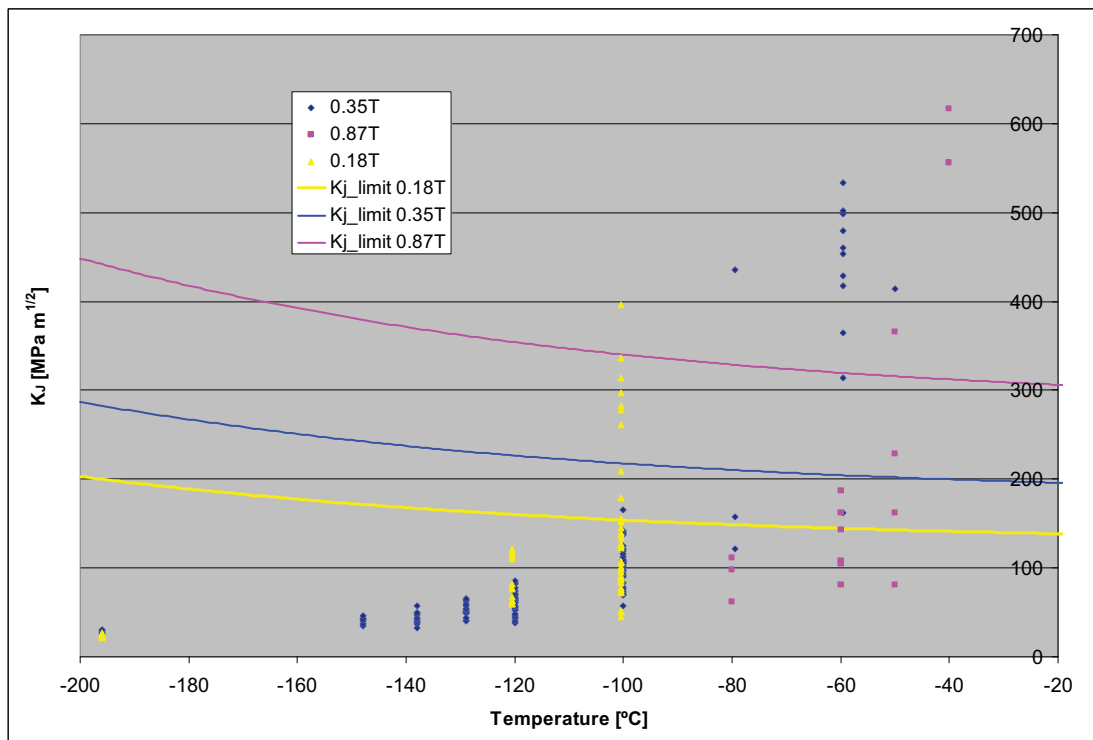
Figure 4-5: Measured fracture toughness data for Eurofer97 along with the standard ASTM size limits ($M_{limit} = 30$) for each specimen size.

In Figure 4-6 the load-displacement curves measured with the clip gage are plotted for 0.35T specimens tested at -60 ºC. The initial slope of the experimental curves shows a very good reproducibility. The difference in maximum load from specimen to specimen is attributed to small variation in the crack length ratio (a/W) and in the

crack angle. By means of finite element simulations, it was observed that a small increase in the crack length ratio decreases the general yield and the maximum load significantly, but the initial slope is not so visibly affected. The curve corresponding to specimen P5.2 represents in good approximation an average load-displacement curve. Hence, this curve was used for comparison with that calculated from the finite element simulations, where the modeled crack length ratio was a/W = 0.52. This value corresponds to the average measured initial crack length ratio of the specimens tested above -90 ºC (also about a/W=0.52). In the plot, the load and deformation at the breaking point is clearly visible. The breaking load is similar in all specimens, nevertheless not all the specimens undergo the same amount of deformation before fracture. For the specimens that broke beyond maximum load a small amount of ductile tearing could be observed in the fracture surface of the broken specimen. This indicates that in these cases some amount of stable crack growth, up to about 1 mm, occurred before unstable fracture.
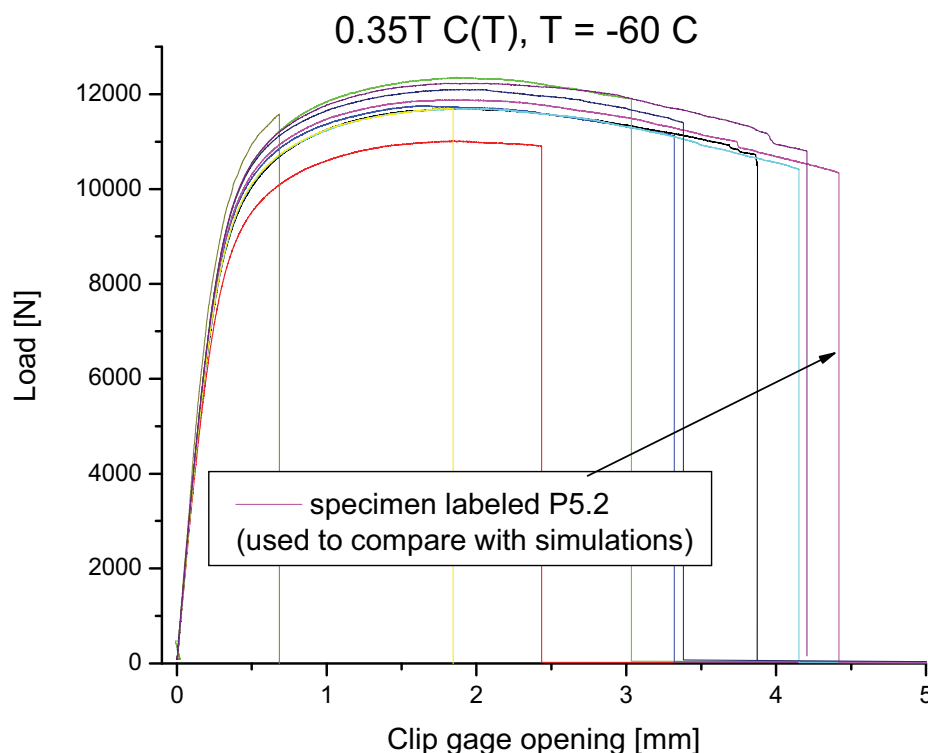

Figure 4-6: Load - displacement curves of the specimens measured with an attached clip gage.

4.3   Standard Master Curve method

The American Society of Testing Materials has developed the standard ASTM E 1921 [3] to measure a ductile-to-brittle transition reference temperature, T_0, from a small number of data, obtained with specimens tested within a temperature window of $T_0 \pm$ 50 ºC. This approach is a standardization of the Master Curve method proposed by Wallin [4, 5]. This method was initially developed for fission reactor pressure vessel ferritic (RPV) low alloy steels and seems to work fairly well for this kind of steels. For instance in [6], Wallin analyzed the "Euro" fracture toughness dataset [7] in terms of the Master Curve approach.

The transition temperature T_0 is defined as the temperature where the median fracture toughness (K_{Jc}) of 1T thickness (B=25.4mm) specimens is 100 MPa m$^{1/2}$. The standard Master Curve is based on a universal shape of the temperature-median toughness curve, a Weibull description of the scatter and a statistical size effect associated to the crack front length.

The universal median toughness temperature dependence for 1T specimens is described by the following equation [8]:

$$K_{Jc\_med}(T) = A + (100 \, MPa \, m^{1/2} - A) \, exp(C(T - T_0)) \tag{4.7}$$

With A = 30 MPa m$^{1/2}$ and C = 0.019 / ºC. T_0 is the only material dependent parameter.

The standard provides a toughness size adjustment if specimen sizes different from 1T are used. This correction accounts for the statistical size effect and reads:

$$K_1 = K_{min} + (K_2 - K_{min})\left(\frac{B_2}{B_1}\right)^{1/4} \tag{4.8}$$

where K_{min} is a minimum threshold value, usually taken equal to 20 MPa m$^{1/2}$ for ferritic steels. Note that this B-scaling was experimentally verified to work fairly well [9].

The standard assumes that the cumulative failure probability of a dataset at a given temperature follows Eq. (4.9) if $K_{Jc} < K_{Jc\_limit}$.

$$P(K_{Jc} < K) = 1 - \exp\left(-\left(\frac{K - K_{min}}{K_0 - K_{min}}\right)^4\right) \tag{4.9}$$

with $K_0 = (K_{Jc\_med} - K_{min})\ln(2)^{-1/4} + K_{min}$. This means that K_0 corresponds to a 63.2% cumulative failure probability and is the temperature dependent parameter in Eq. (4.9)

The toughness limit K_{Jc_limit} is given by Eq. (4.6), with M=30, b_0 = W - a_0, being a_0 the initial crack length, E the Young modulus, ν the Poisson ratio and σ_{ys} the yield stress. Note that $b_0 \approx B$ when a/W $\approx$ 0.5 and that K_{Jc_limit} depends on the specimen size [10].

In addition to the specimen crack front length adjustment of Eq. (4.8), the issue of constraint loss is addressed in the ASTM standard by defining a specimen measuring capacity with Eq. (4.6).

The standard assumes that the measured K_{Jc} values that fall below the K_{Jc_limit} are not affected by loss of constraint and that the distribution of these values will follow Eq. (4.9) for $K_{Jc} < K_{Jc\_limit}$. On the other end, for values greater than the limit, $K_{Jc} > K_{Jc\_limit}$, it is assumed that loss of constraint could have affected the measured K_{Jc} by increasing its apparent toughness and thus these values would not follow the mentioned distribution. Nonetheless, as already mentioned, a value above the limit still carries some useful information: the toughness of the specimen was at least equal or greater than the limit because, before reaching the limit, it did not loose constraint and did not break. The standard combines these assumptions with equations (4.7),

(4.8), (4.9) and (4.6) in order to determine T_0 by means of the maximum likelihood method. This leads to Eq. (4.10) where T_0 can be determined by iteration.

$$\sum_{i=1}^{N} \delta_i \frac{\exp(0.019(T_i - T_0))}{11 + 77\exp(0.019(T_i - T_0))} - \sum_{i=1}^{N} \frac{(K_{Jc(i)} - 20)^4 \exp(0.019(T_i - T_0))}{(11 + 77\exp(0.019(T_i - T_0)))^5} = 0 \quad (4.10)$$

With the temperatures in ºC, K_J in MPa m$^{1/2}$ and:

N : number of specimens tested

T_i : test temperature corresponding to $K_{Jc(i)}$

$K_{Jc(i)}$: either K_{Jc} (if $K_{Jc} < K_{Jc\_limit}$) or K_{Jc_limit} (if $K_{Jc} > K_{Jc\_limit}$)

δ_i : either 1.0 (if $K_{Jc} < K_{Jc\_limit}$) or zero (if $K_{Jc} > K_{Jc\_limit}$)

4.4   Standard Master Curve analysis of the fracture database

In this section we analyze the Eurofer97 fracture toughness data first in terms of the master curve exactly as standardized by the American Society of Testing and Materials in ASTM E 1921 [3]. In particular we highlight that this means A=30MPa m$^{1/2}$ and M=30 in equations (4.7) and (4.6) respectively. The standard requires that only the data tested in the temperature range $T_0 \pm 50$ ºC should be used to estimate the transition temperature T_0. Since T_0 is the unknown parameter, the selection of the appropriate datasets is performed iteratively. This procedure gives as a result $T_0 = -87.6\,^{\circ}\text{C}$, with the fracture data tested at -129, -120, -100, -80, -60 and -50 ºC. This data gives a total of 154 experiments from which 131 fall below the maximum toughness limit of Eq. (4.6) with M=30. It has been verified that the inclusion or not of the datasets at -40 and -138 ºC changes T_0 in only about 0.5 ºC.

The first problem in the use of the standard MC as it is with Eurofer97 steel can be seen in Figure 4-7 where at low temperature most of the measured data falls below the median toughness prediction. In next sections this problem is even more evident when comparing the transition temperature predictions obtained by performing single

temperature T_0 estimations with individual datasets rather than using all the data together.
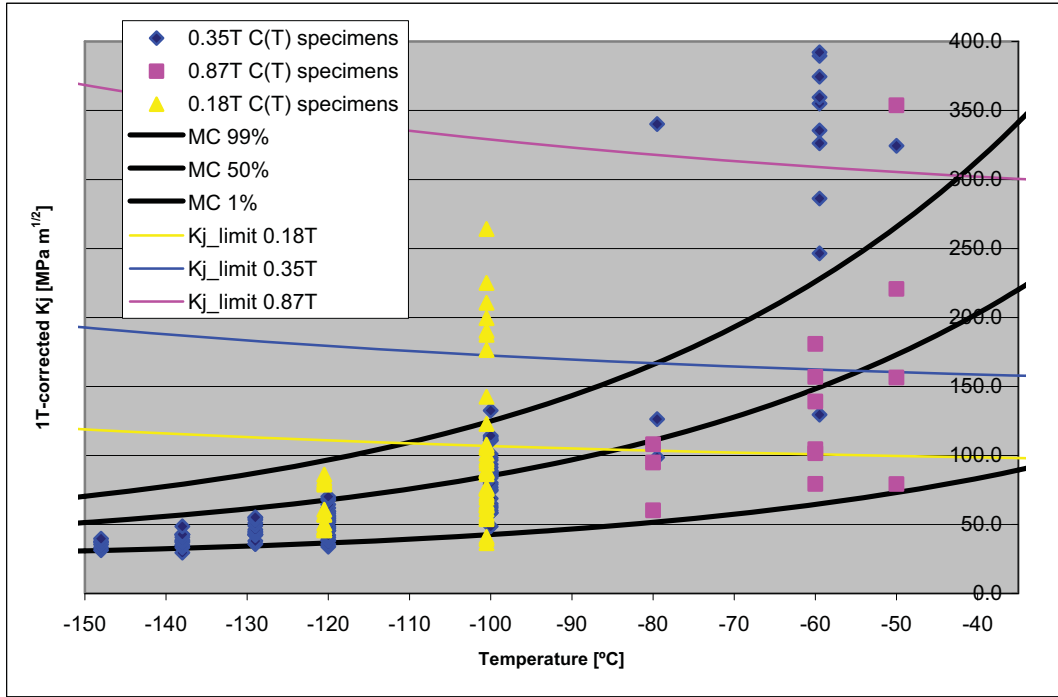
Figure 4-7: Standard Master Curve fit of the Eurofer97 fracture toughness dataset.

The second problem of the standard MC application to Eurofer97 is also evident in last figure. At -60 degrees almost no 0.35T specimen broke below the median toughness predicted by the MC despite of the fact that the median toughness is below the toughness limit. Next two sections basically deal with solving these two mentioned problems by adapting the MC in order to properly describe steels like Eurofer97.

4.5   Master Curve shape adjustment

4.5.1   Statistical analysis method

In this subsection we generalize the maximum likelihood analysis performed for the standard MC in section 4.3   to determine T_o in order to be able to estimate and

adjust the shape parameters, namely A and C, of the median toughness-temperature curve in Eq. (4.7).

At different given temperatures in the transition region, a number of specimens were tested to study the intrinsic scatter in the toughness data. The data were analyzed within the framework of statistical brittle fracture models [10, 11] that yield, for highly constrained specimens, the cumulative failure probability as the three parameter Weibull distribution, Eq. (4.9). We recall that the statistical models predict a B-dependence of the form of Eq. (4.8).

The effect of in-plane constraint loss on the measured toughness imposes a higher limit of K_{Jc}, the so-called K_{Jc_limit}, below which the measured toughness can be regarded as independent of the ligament length b (Eq. (4.6)). The ASTM E1921 requires that M=30 but this value is discussed here and in next sections in the light of the presented results.

The temperature dependence of the median toughness of 25.4 mm thick specimens (1T) in the transition region of "ferritic" steels is given by the ASTM master curve Eq. (4.7) with A = 30 MPa m$^{1/2}$ and C = 0.019 1/ºC. We have reported in [12, 13] a toughness behavior in the lower transition region of the Eurofer97 steel that deviates somewhat from Eq. (4.7) with A = 30 MPa m$^{1/2}$ and C = 0.019 / ºC. However, with the new data obtained in this study and owing to the large number of data points of this analyzed database, it was possible to better assess and fit the coefficients of Eq. (4.7) as presented hereafter and published in [14].

By doing so, we adjust the level of the athermal part of master curve (A) as well as the shape (C). Note that the term (100 – A) in (4.7) keeps the significance of T_o as the temperature where the median toughness is 100 MPa m$^{1/2}$. The parameters A, C and T_o in Eq. (4.7) can be obtained by using the method of maximum likelihood. The likelihood function of the Weibull probability density reads:

$$L = \prod_{i=1}^{N} \frac{4(K_{Jc,i} - K_{min})^3}{(K_o(T) - K_{min})^4} \; \exp(-(\frac{K_{Jc,i} - K_{min}}{K_o(T) - K_{min}})^4) \qquad (4.11)$$

Having a dataset ($K_{Jc,i}$ at T_i), the coefficient A, C and T_o are determined by solving numerically and iteratively the three equations: $\partial lnL/\partial A = \partial lnL/\partial C = \partial lnL/\partial T_o = 0$, which are respectively:

$$\sum_{i=1}^{n} \frac{(1 - \exp(C(T_i - T_o)))}{(K_o - K_{min})} - \sum_{i=1}^{n} \ln(2) \frac{(K_{J,i} - K_{min})^4 (1 - \exp(C(T_i - T_o)))}{(K_o - K_{min})^5} = 0 \quad (4.12)$$

$$\sum_{i=1}^{n} \frac{\exp(C(T_i - T_o))(T_i - T_o)}{K_o - K_{min}} - \sum_{i=1}^{n} \frac{(K_{J,i} - K_{min})^4 \exp(C(T_i - T_o))(T_i - T_o)}{(K_o - K_{min})^5} = 0 \quad (4.13)$$

$$\sum_{i=1}^{n} \frac{\exp(C(T_i - T_o))}{K_o - K_{min}} - \sum_{i=1}^{n} \frac{(K_{J,i} - K_{min})^4 \exp(C(T_i - T_o))}{(K_o - K_{min})^5} = 0 \qquad (4.14)$$

With $\left(K_o - K_{min}\right) = \dfrac{A - K_{min}}{\ln(2)^{1/4}} + \dfrac{(100 - A)\exp(C(T - T_o))}{\ln(2)^{1/4}}$.

4.5.2   Application

In this subsection equations (4.12) to (4.14) are applied in order to adjust the athermal part of the MC witch is controlled by the A parameter. In order to make a proper estimation of this parameter, it is necessary to avoid the use of data that suffered from loss-of-constraint. Therefore we start with a short discussion related to the size limit criterion that will be further analyzed and confirmed in next sections.

Eq. (4.9) was used to draw failure probability diagrams. An example is shown in Figure 4-8 for two datasets of measured toughness data at -100 °C obtained with 0.18T and 0.35T C(T) specimens. The rank probability was calculated as $P_f = (i-0.3)/(n+0.4)$, i is the rank of the data considered and n the number of points [15]. This probability diagram was constructed by considering K_{min}=20 MPa m$^{1/2}$. In Figure 4-8,

a deviation from the expected linear behavior is observed for the 0.18T C(T) specimens at a limit measured toughness of about 90 MPa m$^{1/2}$, which corresponds to an M value (see Eq. (4.6)) of about 80. This deviation is attributed to constraint loss that results in an increase of the measured toughness. It has to be emphasized that this M value is significantly larger than M=30 recommended in the ASTM E1921 standard. This observation is also consistent with the extensive fracture database of Rathbun *et al.* [9] who showed that constraint loss begins at relatively low deformation levels, corresponding to M $\approx$ 200 for bend bars. In Figure 4-9, the measured toughness is plotted versus temperature along with the K_{Jc_limit} lines. The filled symbols correspond to measured toughness on specimens for which the load-displacement curve passed through a maximum and for which the toughness was calculated at the point of fracture. Such specimens underwent a large amount of plasticity and, as a consequence, suffer from significant constraint loss so that the toughness measured on such specimens is not really representative of cleavage toughness. Thus, those points were not considered in the following master curves analysis. In addition, we emphasize that there are in total six datasets, at six different temperatures, that are well constrained, namely below the K_{Jc_limit} lines associated with M=80. These datasets are the four ones of the 0.35T C(T) specimens at the lowest temperature and the two datasets of the 0.87T C(T) at -80 °C and -60 °C. These six datasets will be considered later as reference data to assess the shape of the toughness-temperature curve.
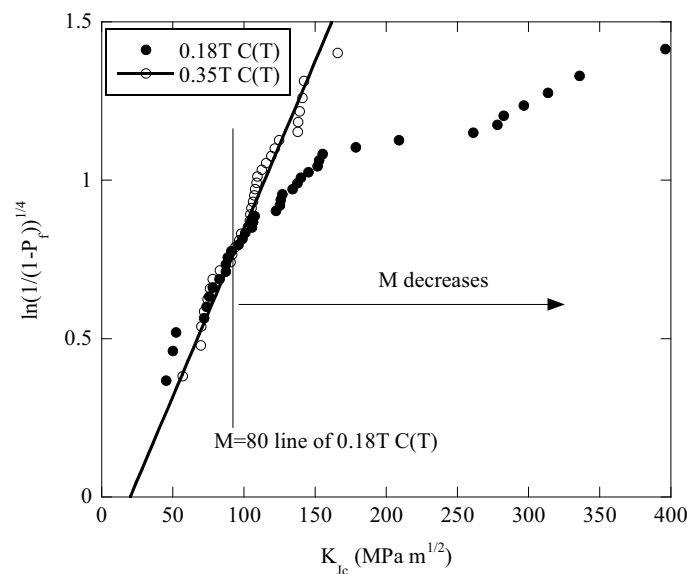

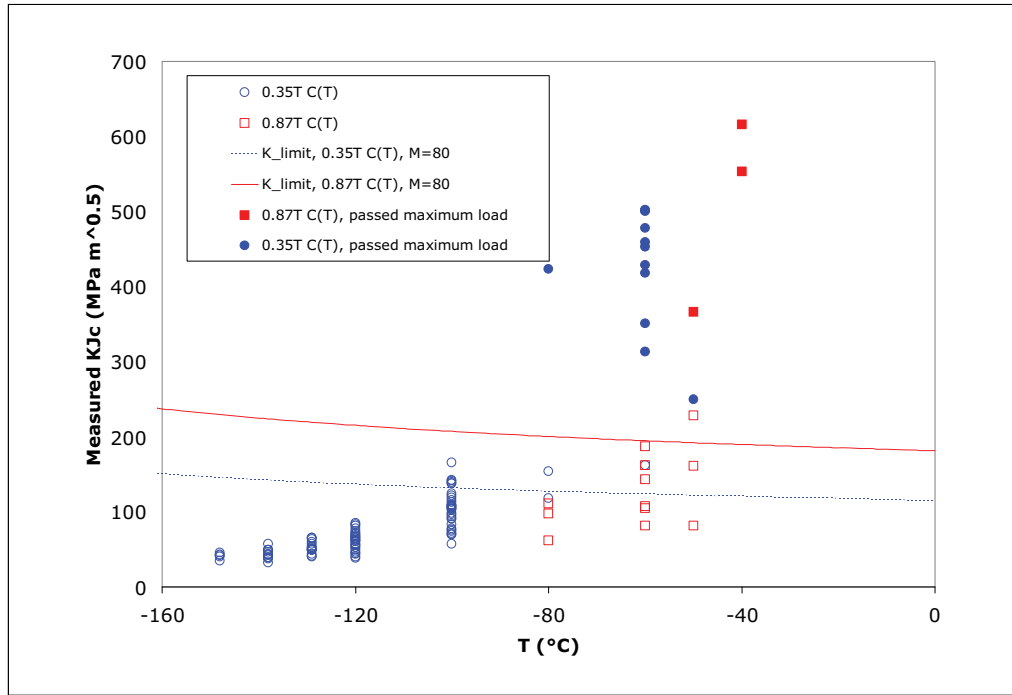**Figure 4-8**: Failure probability diagram at T = -100 °C.

Figure 4-9: Measured fracture data and K_{Jc_limit} lines associated with M=80.

First, a multi-temperature determination of T_o was performed according to the ASTM E1921 standard by considering only the 0.87T C(T) data. Note that for the censoring of the data we used a K_{Jc_limit} (Eq. (4.6)) with M=80. Again, as mentioned above, the three data points that failed after a large amount of plasticity (beyond maximum load on the load-displacement curve) were not considered in the analysis. Only one point lied above the K_{Jc_limit} associated with M=80, which was replaced by the K_{Jc_limit} value according to the standard. T_o was found equal to -78 °C. All 1T-adjusted data are plotted in Figure 4-10 along with the MC indexed at -78 °C. One observes that on the lower transition region side, for temperatures ≤ -120 °C, most of the 0.35T C(T) data fall below the median curve. For instance, at -120 °C, only 4 points over 27 lie above the median curve. However, this temperature is still in the restricted temperature range, defined as $T_o \pm 50$ °C, in which the reference temperature T_o can be in principle determined [3]. Furthermore, in Figure 4-11, we plot T_o as determined from a series of single temperature T_o-determination made on the four lower temperature datasets. As indicated in Fig. 4, the two lowest temperature datasets are well outside the validity range of the ASTM E1921 applicability range, the dataset at -129 °C is just one degree Celsius out and the dataset at -120 °C is within the applicability range. T_o determinations out the applicability temperature range of the ASTM E1921 standard

were done to find how fast T_o diverges from the correct value when analyzing data at temperature lower than T_o-50 °C. The trend line showed in Figure 4-11 indicates that T_o decreases with increasing T_o determination temperature indicating that on the lower shelf side, the ASTM master-curve does not describe properly the median toughness, even in the temperature range where it is supposed to work. Indeed, applying the ASTM E1921 standard at -128 and -120 °C, the trend line in Figure 4-11 indicates that testing at those last temperatures would yield T_o values respectively 30 and 15 °C greater than the correct T_o. In addition, it is emphasized that the T_o values calculated on the low temperature datasets are very far from the T_o value calculated on the 0.87T C(T) data, which is -78 °C; they overestimate T_o determined with the 0.87T C(T) specimens up to about 50 °C. These observations, made possible by the large number of data points in this analyzed database, led us to make an adjustment of the toughness-temperature curve shape.
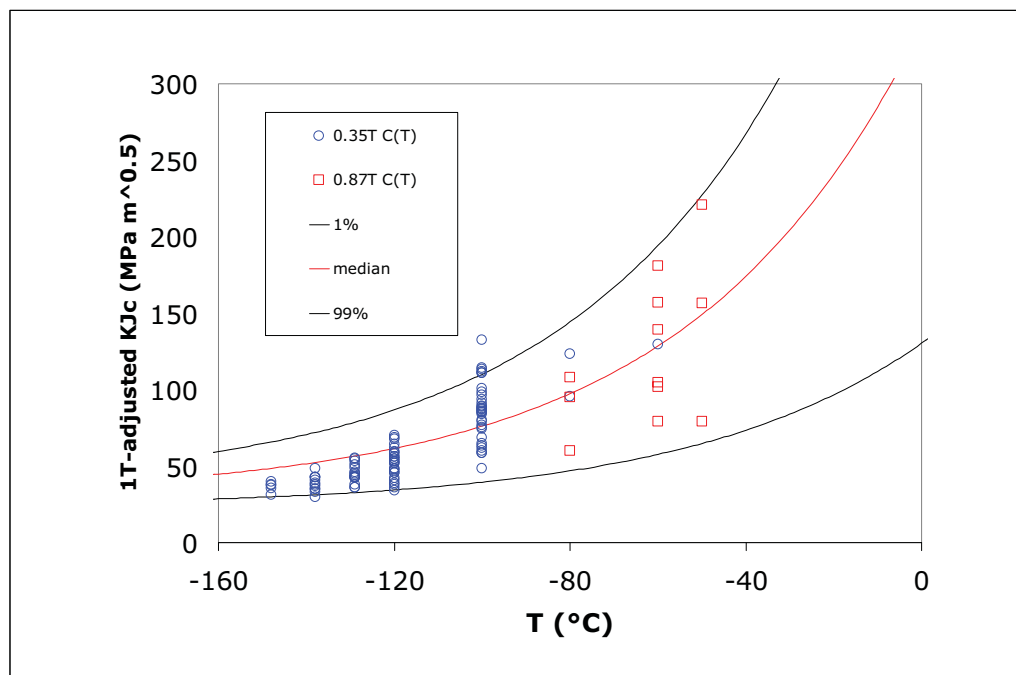
Figure 4-10: Standard ASTM E1921 master-curve analysis on the 0.87T C(T) data, T_o=-78 °C.
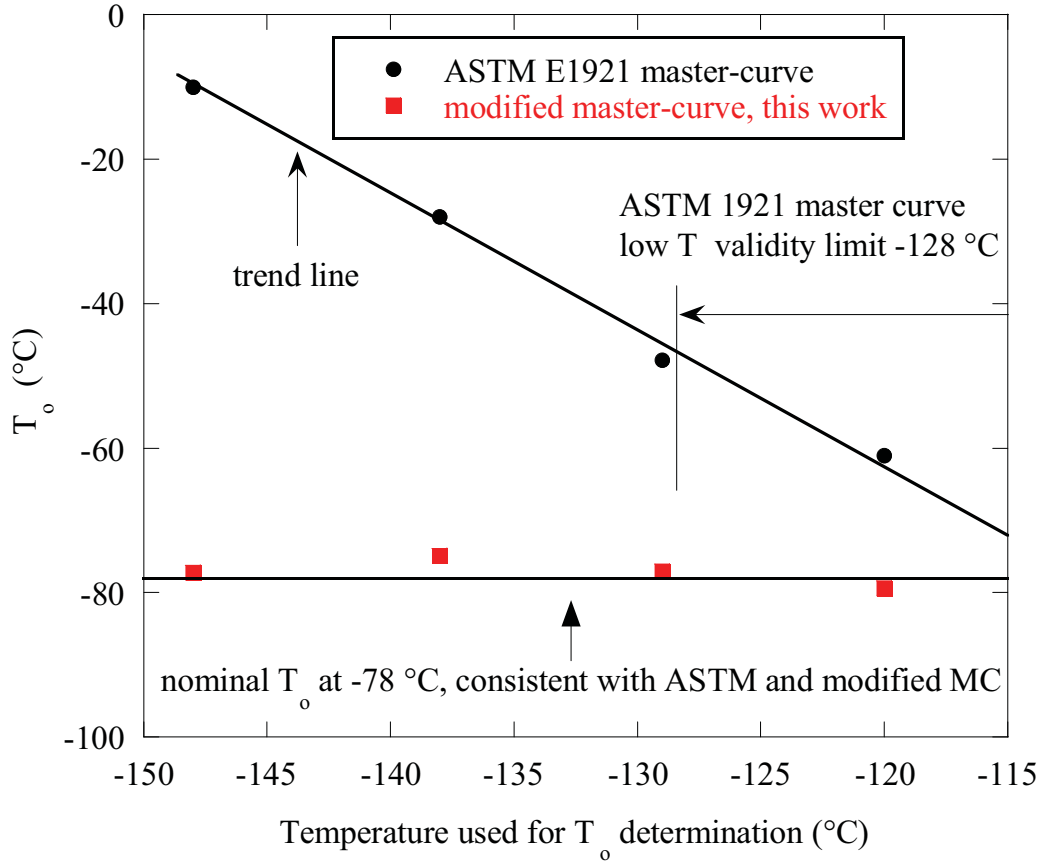
Figure 4-11: Single temperature T_o determination versus testing temperature with the ASTM-MC and modified-MC.

Having identified lower values of toughness than predicted by the ASTM E1921 master-curve, an adjustment of the coefficients in Eq. (4.7) was done. While it is in principle possible to fit the three parameters (A, C and T_o), we followed the procedure recommended by Wallin [16] and fitted only the athermal part of the master-curve (A) and the reference temperature T_o. This approach allows improving the description of the toughness-temperature curve in the lower transition region without modifying appreciably the general properties of the master-curve in the middle transition region [17]. The two coefficients were then obtained by solving numerically and iteratively Eq. (4.12) and Eq. (4.14). As mentioned at the end of the first paragraph of this section, we emphasize that we have considered only the fully constrained datasets. For example, the data of the 0.35T C(T) at -100 °C were not included in the shape assessment as the cumulative failure probability function of these data was shown to be biased by constraint loss. The resolution of the system of equations yielded the following parameters for the so-called modified-master curve:

$$K_{Jc\_median(1T)} = 12 + (100 - 12)\exp(0.019(T - T_o)) \qquad (4.15)$$

with $T_o = -78$ °C.

This modified master curve is plotted in Figure 4-12 where we can see that on the lower shelf side, the curve describes much better the data. Note that the data above the 99% failure bound at -100 °C are believed to have suffered from constraint loss. In order to cross-check the self-consistency of the modified master-curve, we performed a second multi-temperature T_o determination of the 0.87T C(T) data only and found $T_o = -75$ °C, which is in good agreement with the T_o obtained in Eq. (4.15), whose parameters are somewhat overweighed by the many low temperature data points. We also recalculated T_o with the modified master-curve equation on the low temperature 0.35T C(T) datasets (single T_o-determination) and plotted the results in Figure 4-11. While a very weak decrease of T_o was found (red squares) the absolute value of T_o is now consistent with a nominal T_o at -78 °C.
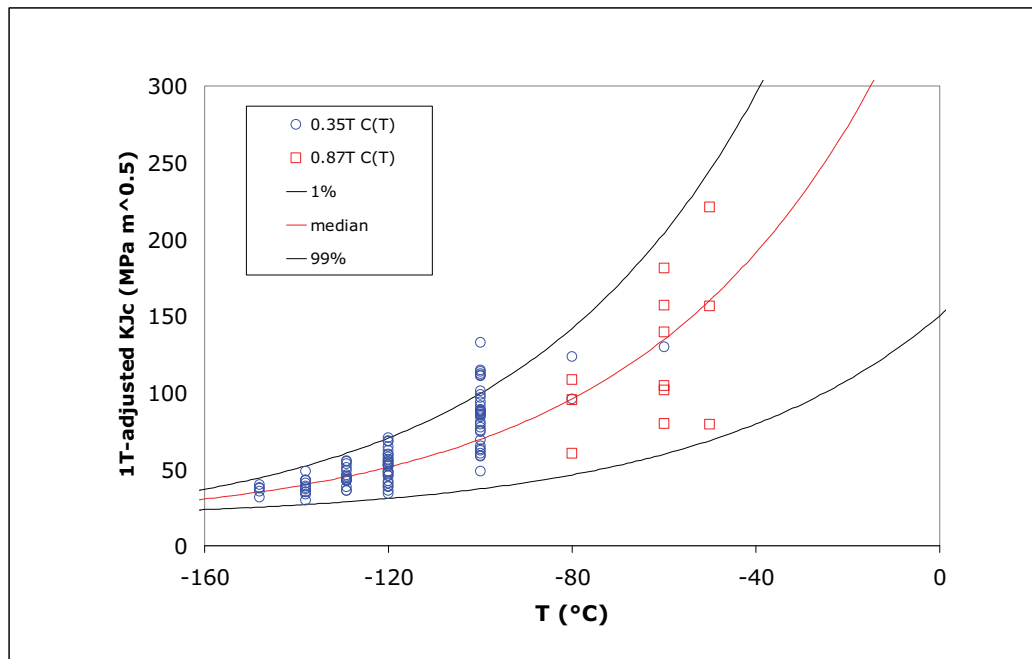

Figure 4-12: Modified master-curve analysis on the 0.87T C(T) data, T_o=-78 °C.

A check of the statistical description of the database (fully constrained datasets, namely those at -148, -138, -129, -120, -80, -60 °C), which contains 70 points, was

done for the modified master-curve and compared with the ASTM E1921 master-curve. By combining Eq. (4.9) with Eq. (4.7), it is straightforward to derive the temperature dependence on any given cumulative failure probability X, which is then given by:

$$K_{Jc(X)} = K_{min} + \left[\ln\left(\frac{1}{1-X}\right) \right]^{1/4} \left\{ \frac{A - K_{min}}{\ln(2)^{1/4}} + \frac{(100-A)}{\ln(2)^{1/4}} \exp\left[0.019(T - T_o) \right] \right\}$$

(4.16)

In Table 4-2 and Table 4-3, we counted the number of points falling above the upper bound and below the lower bound, determined with Eq. (4.16) for the desired failure probability and we compared the results with the predicted number. Again, we observe that the number of points falling out the bounds is completely asymmetric for the ASTM master-curve (Table 4-2) and inconsistent with the predictions when the master-curve and associated bounds are extended to lower temperatures than T_o - 35 °C, i.e. even in the valid temperature range. On the contrary, a very good agreement was found for the modified-master curve (Table 4-3).

Lower bound: LB.	Data below LB.	Upper bound: UB.	Data above UB.	Total data out of the two bounds.	Expected data out of the two bounds.
5%	14	95%	1	15	7
10%	26	90%	1	27	14
20%	40	80%	2	42	28
35%	53	65%	6	59	49

Table 4-2: Statistics on the fully constrained datasets (see text) calculated with the ASTM E1921 master-curve, T_o = -78 °C.

Lower bound: LB.	Data below LB.	Upper bound: UB.	Data above UB.	Total data out of the two bounds.	Expected data out of the two bounds.
5%	4	95%	4	8	7
10%	7	90%	8	15	14
20%	18	80%	13	31	28
35%	25	65%	22	47	49

Table 4-3: Statistics on the fully constrained datasets (see text) calculated with the modified master-curve Eq. 9. A=12 MPa m$^{1/2}$, T_o = -78 °C.

We emphasize that the modifications in the master-curve shape we propose here are critical if T_o determination is foreseen in a temperature window close to T_o-50 °C while they are almost irrelevant if T_o is determined with 1T-thick specimens at temperature close to T_o. This is illustrated in Figure 4-13 where the two master-curves are plotted together. Clearly, one can see that below -120 °C the amplitude of the scatter of the modified master-curve lies between the lower bound and median curve of the ASTM master-curve. Note that the ASTM E1921 procedure does not recommend doing crack front length adjustments of toughness (Eq. (4.8)) near the lower shelf. However, if the crack front adjustments are not done on the datasets at -148 ºC and -138 °C, which contain seventeen data, sixteen data remain below the ASTM E1921 median master curve. This observation gives additional credit to a moderate adjustment of the athermal component of the master-curve. The value of the athermal component in Eq. (4.15) (12 MPa m$^{1/2}$) suggests that the K_{min} value in Eq. (4.9) may be lower than 20 MPa m$^{1/2}$. Having to assess fracture toughness before and after irradiation with small specimens prone to very rapid constraint loss, it is critical to know precisely the toughness-temperature behavior close to the lower shelf to predict correctly T_o by extrapolation of the $K_{Jc\_med}(T)$ equation.
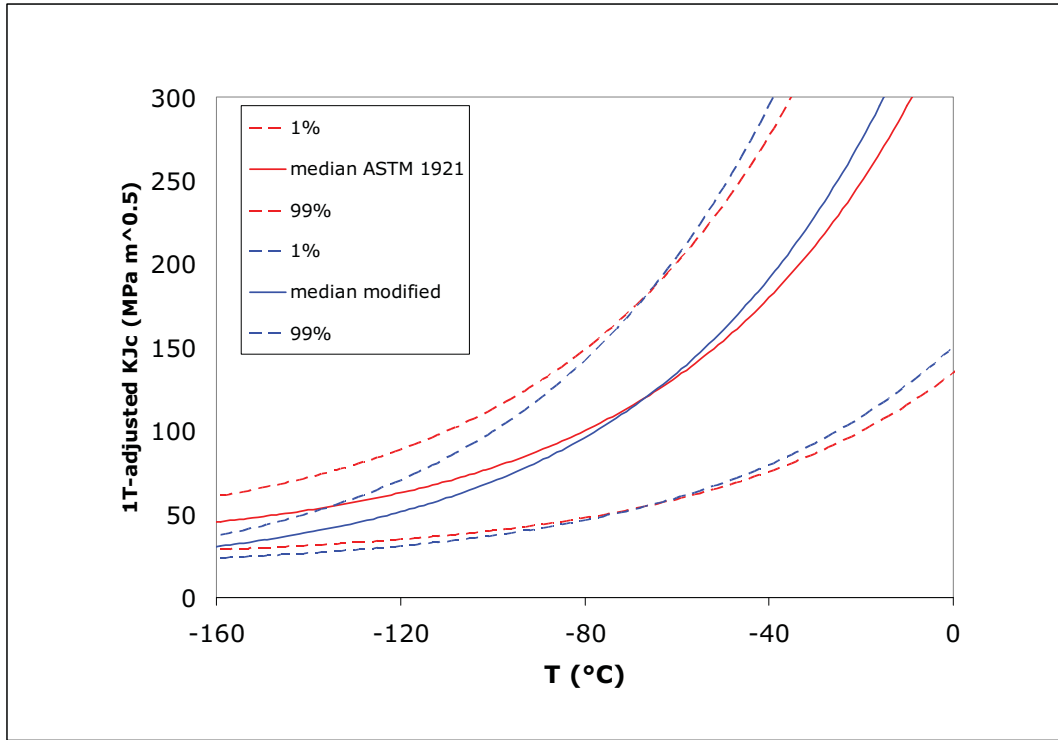
Figure 4-13: Comparison of the two master-curves, note the difference in the scatter amplitude below about -100 °C.

4.5.3   Conclusions

The fracture toughness behavior of the Eurofer97 steel was investigated in the lower to middle ductile to brittle transition region. By determining T_o in the middle transition region with the 0.87T C(T) specimens, we showed that in the lower transition region, the ASTM E1921 master-curve does not predict satisfactorily the temperature dependence of the median toughness and the scatter. In order to improve the description of the data near the lower shelf region, two parameters of the master-curve were fitted using the method of maximum likelihood, namely the athermal component, A, and the reference temperature, T_o. We found that the athermal part is significantly lower (12 MPa m$^{1/2}$) than the recommended value of the ASTM E1921 master-curve (30 MPa m$^{1/2}$). Thanks to the adjustment of the coefficient A, we demonstrated that the modified master-curve allows determining accurately T_o from tests at temperatures near the lower shelf region. Indeed, a value of T_o was found almost independent of the dataset temperature used to determine it when using the single temperature T_o determination method. Therefore it is of primary importance not

to overlook such shape adjustment if small specimens are used near the lower shelf to determine T_o.

4.6   Master Curve size limit adjustment

4.6.1   *Specimen size effect on measured fracture toughness*

The fracture toughness data of Eurofer97 steel tested above -100 ºC are shown in Figure 4-14 along with the ASTM E1921 toughness limit (K_{Jc_limit}) for the two tested specimen sizes: 0.37T and 0.87T The open symbols correspond to specimens having a load-deflection curve showing a load maximum. We recall that, within the framework of the ASTM E1921, this toughness limit is associated with an M value equal to 30. At -60 ºC, K_{Jc_limit} of the 0.35T specimens is approximately 205 MPa m$^{1/2}$. For this temperature the median toughness of the six 0.87T C(T) specimens tested was 131 MPa m$^{1/2}$. Using the ASTM size adjustment, Eq. (4.8), the median toughness of the 0.87T C(T) specimens increases up to 159 MPa m$^{1/2}$ for the 0.35T C(T). Thus, 0.35T C(T) median toughness value is well below the K_{Jc_limit} calculated with M=30. Consequently, we would expect to find about one half of the 0.35T values below 159 MPa m$^{1/2}$. However, from the eleven 0.35T specimens tested at -60 ºC, ten broke between 300 and 500 MPa m$^{1/2}$ and only one at 162 MPa m$^{1/2}$. Clearly loss of constraint starts much before what is predicted by the toughness limit related to M=30. Therefore, this limit is not restrictive enough and needs to be redefined.
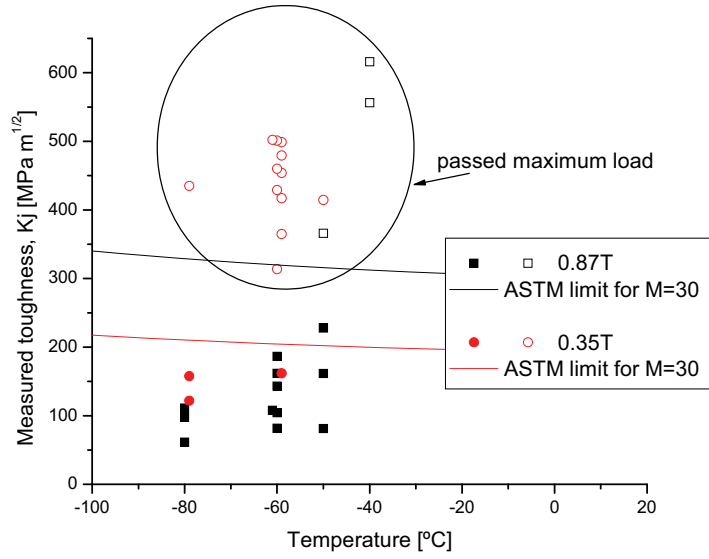
Figure 4-14: Experimental Eurofer'97 steel fracture toughness data measured with C(T) specimens.

In addition, the lowest toughness value from the six 0.87T specimens measured at -60 ºC was 82 MPa m$^{1/2}$. Using Eq. (4.8), this value corresponds to 97 MPa m$^{1/2}$ for a 0.35T specimen. Since none of the eleven 0.35T specimens tested at -60 ºC was close to 97 MPa m$^{1/2}$, in fact all the values fell above 162 MPa m$^{1/2}$, it is clear that loss of constraint already occurs at such low deformation. An M limit value of about M=134 is needed to have a K_{Jc_limit} = 97 MPa m$^{1/2}$ for 0.35T specimens.

We also found similar results when analyzing Sokolov and Tanigawa [18, 19] C(T) fracture data of F82H steel. As mentioned in Chapter 2, F82H is also a reduced activation tempered martensitic steel, from which the chemical composition of Eurofer97 originates, but with moderate difference in the chemical composition. Both of these steels have practically the same elastic properties and similar yield stress. While only one of the five 1T specimens tested at -50 ºC and reported in Table 4-4 showed a high toughness value (412.4 MPa m$^{1/2}$), seven out of the eight 0.4T specimens presented very high values of toughness (> 300 MPa m$^{1/2}$). Among the big specimens (1T), 4 out of 5 have broken below 150 MPa m$^{1/2}$. Using Eq. (4.8) this value corresponds to 183 MPa m$^{1/2}$ for a 0.4T specimen. Since the toughness limit related to M=30 for a 0.4T size specimen is K_{Jc_limit} = 219 MPa m$^{1/2}$, we would expect to find most of the 0.4T specimens below 183 MPa m$^{1/2}$. Only 1 over 8 of the small specimens (0.4T) broke below 300 MPa m$^{1/2}$. Again the experimental results show

clearly that loss of constraint started much before the standard ASTM limit, which means that a toughness limit related to M=30 is not restrictive enough.

Size	Measured toughness [MPa m$^{1/2}$]
1T	94.6
1T	114.6
1T	128.4
1T	146.7
1T	412.4
0.4T	124.5
0.4T	306.0
0.4T	322.9
0.4T	335.9
0.4T	340.6
0.4T	359.1
0.4T	393.0
0.4T	394.4

Table 4-4: F82H C(T) specimens tested at -50 ºC by Sokolov and Tanigawa [18].

4.6.2 T_0 dependence with M-limit

In order to better evaluate the K_{Jc_limit}, and find an M limit which is more representative of the onset of the measurable constraint loss influence on toughness, multi-temperature T_0 determinations (Eq. (4.10)) were performed for the Eurofer97 fracture data plotted in Figure 4-14. Figure 4-15 shows T_0 in function of the M limit value. Clearly T_0 is still significantly dependent on M for values around M = 30, where a strong T_o increase is observed with M. For M greater than about 100, T_0 oscillates around $T_0 \approx$ -75 ºC which is in good agreement with T_0 = -78 ºC that we reported in [14]. The standard requires a minimum of 6 valid data points, namely points lying below K_{Jc_limit}. For M>270 this criterion is not fulfilled (Figure 4-16), which explains the increase in the amplitude of the T_0 oscillations. In a previous section and also published by us in [14], the A value of Eq. (4.7) was fitted with the

method of the maximum likelihood according to [16, 17] in order to adjust the athermal part of the Master Curve to the data tested at low temperature (T<-100ºC). As mentioned the effect of this adjustment is not important at higher temperatures. This is also reflected in Figure 4-15.
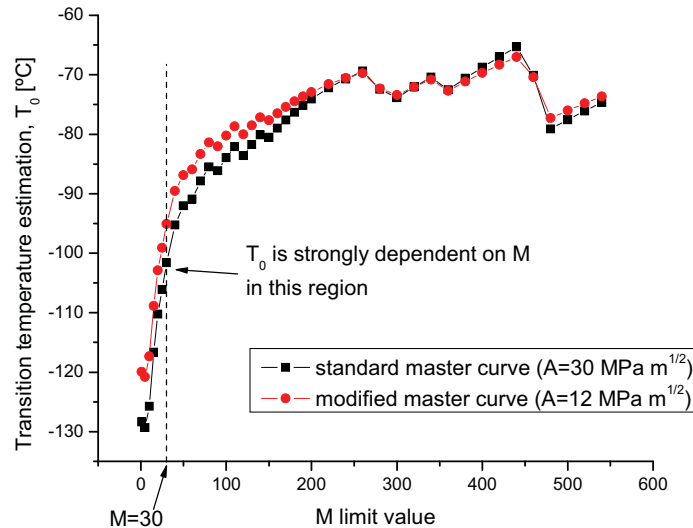
Figure 4-15: Transition temperature (T_0) determination using the data tested at temperatures above -90ºC. T_0 is strongly dependent on the M value in the M<80 region. A maximum toughness limit related to M=30 is not appropriate for this material.
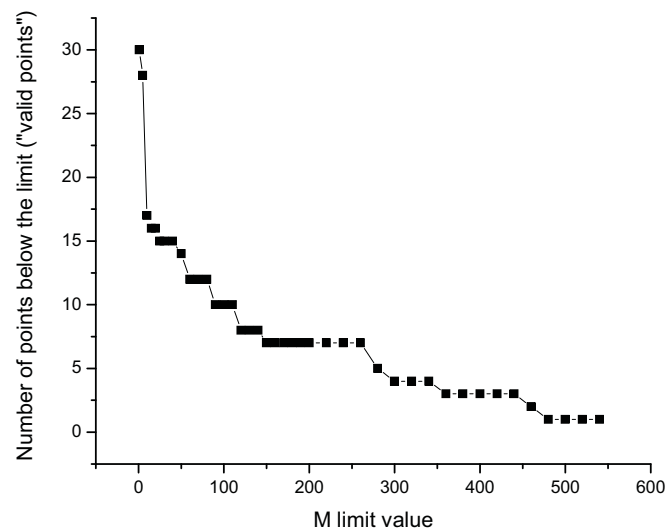

Figure 4-16: Number of points below the maximum toughness limit in function of M. The standard requires a minimum of 6 valid data points. For M>270 the number of valid points is too low.

4.7 Discussion

The main results of this Chapter are related to the Master Curve analysis of the fracture toughness data of Eurofer97. An application of the MC as standardized by ASTM in E 1921 to the fracture toughness database clearly shows that the distribution of the data is not properly described. One of the consequences of this fact is that single-temperature determinations of the ductile-to-brittle transition temperature T_0 is strongly dependent on the testing temperature for testing temperatures in the lower transition region. This occurs even within the temperature range $T_0\pm50^{\circ}C$ where the T_0 determination should properly work according to the standard using only 6 to 8 specimens or more. Another consequence of the bad data distribution prediction of the standard MC is the fact that most of the data in the lower transition ($T<T_0$) falls below the predicted median toughness.

To solve this first problem an adjustment of the athermal part of the MC was proposed (A-adjustment) and was shown to successfully fit the data distribution. Predicting fracture toughness as well as predicting the ductile-to-brittle transition temperature by testing small specimens is a crucial issue for the materials for fusion research community. Due to the limited irradiation volume of current and future materials irradiation facilities the fusion research community is forced to test small specimens. In order to avoid loss of constraint it is needed to test the small specimens in the lower shelf temperature range. This fact makes the adjustment of the athermal part of the MC (A-adjustment) extremely important to obtain a representative value of T_0.

The second problem regarding the application of the MC as standardized is related to the fracture toughness measuring capacity of a given specimen size. The standard minimum size requirements are too lenient. This fact is clearly observed in the temperature range corresponding to the upper transition ($T>T_0$). In this range the big specimens (0.87T) broke with relatively low fracture toughness. According to the standard size limits the measuring capacity of the smaller 0.35T specimens was well above the materials toughness. Nevertheless practically all of the tested 0.35T

Eurofer97 specimens suffered from loss of constraint which led to non realistic very high toughness values. Similar results were also found for F82H-mod steel tested at similar temperatures. These results clearly indicate that the standard limits are not appropriate for these tempered martensitic steels. If small specimens are used in the upper transition region, a significantly higher size limit criteria is extremely important to avoid wrong fracture toughness and T_0 determinations.

Note that the problems found by applying the standard MC to Eurofer97 and F82H-mod steels were not only found for these particular steels. Some similar results have already been reported for fission reactor bainitic steels. In next chapter we will address the problem of loss-of-constraint by a completely different way by studying the stress and strain fields of the tested specimens at the moment of fracture in order to model brittle fracture initiation by means of the finite element simulation results.

4.8   References

[1]   ASTM. E 1820 - 08. Standard Test Method for Measurement of Fracture Toughness; 2001.

[2]   Bonadé R. PhD Thesis Number 3405, Constitutive Behavior and Fracture Properties of Tempered Martensitic Steels for Nuclear Applications: Experiments and Modeling. Lausanne, Switzerland: EPFL; 2006.

[3]   ASTM. E 1921 - 08. Standard Test Method for Determination of Reference Temperature, T_0, for Ferritic Steels in the Transition Range; 2008.

[4]   Wallin K. The master curve method: a new concept for brittle fracture. Int J of Materials and Product Technology. 1999;14:342-354.

[5]   Wallin K. Structural integrity assessment aspects of the Master Curve methodology.   Engineering   Fracture   Mechanics.   2009;   doi: 10.1016/j.engfracmech.2009.02.010.

[6]   Wallin K. Master curve analysis of the "Euro" fracture toughness dataset. Engineering Fracture Mechanics. 2002;69:451-481.

[7]   Heerens J, Hellmann D. Development of the Euro fracture toughness dataset. Engineering Fracture Mechanics. 2002;69:421-449.

[8]   Wallin K. Irradiation Damage Effects on the Fracture Toughness Transition Curve Shape for Reactor Pressure Vessel Steels. Int J Pres Ves & Piping. 1993;55:61-79.

[9]   Rathbun HJ, Odette GR, He MY, Yamamoto T. Influence of statistical and constraint loss size effects on cleavage fracture toughness in the transition - A model based analysis. Engineering Fracture Mechanics. 2006;73:2723-2747.

[10]   Wallin K. Journal de Physique IV, Colloque C7, supplément au Journal de Physique III. 1993;3:575-584.

[11]   Wallin K. The Scatter in K_{IC}-Results. Engineering Fracture Mechanics. 1984;19:1085-1093.

[12]   Spätig P, Bonadé R, Odette GR, Rensman JW, Campitelli EN, Mueller P. Plastic flow properties and fracture toughness characterization of unirradiated and irradiated tempered martensitic steels. Journal of Nuclear Materials. 2007;367-370:527-538.

[13]   Bonadé R, Spätig P, Baluc N. Fracture toughness properties in the transition region of the Eurofer97 tempered martensitic steel. Journal of Nuclear Materials. 2007;367-370:581-586.

[14]   Mueller P, Spätig P, Bonadé R, Odette GR, Gragg D. Fracture toughness master curve analysis of the tempered martensitic steel Eurofer97. Journal of Nuclear Materials. 2009;386-388:323-327.

[15]   Lipton C, Sheth NJ. in Statistical design and analysis of engineering experiments New York: McGraw-Hill. 1973.

[16]   Wallin K. Effect of Strain Rate on the Fracture Toughness Reference Temperature T_0 for Ferritic Steels. Recent Advances in Fracture (Proc Int Conf Orlando, 1997) Minerals, Metals, and Materials Society, Warrendale, PA; 1997. p. 171-182.

[17]   IAEA. Technical reports series No 429, "Guidelines for application of the master curve approach to a reactor pressure vessel integrity in nuclear power plants". IAEA, Vienna; 2005.

[18]   Sokolov MA, Tanigawa H. Application of the master curve to inhomogeneous ferritic/martensitic steel. Journal of Nuclear Materials. 2007;367-370:587-592.

[19]   Sokolov MA, Tanigawa H. Fusion Materials Semiannual Progress Report for the period ending December 31, 2006, DOE-ER-0313/41. p. 85-97.

Chapter 5

Finite Element Simulations

In this chapter we present finite element simulations of the pre-cracked C(T) specimens, the notched specimens and the tensile specimens of Eurofer97. The numerical results are compared with the experimental ones presented in last chapter. The main objective of these finite element simulations is to calculate the stress and strain fields in function of the loading level of the studied specimens. In particular, these results are used to estimate the stress state at the onset of brittle fracture as well as to study and calibrate the parameters of a local approach model aimed to predict brittle fracture.

5.1 The σ*-V* local approach model: basis and implementation

5.1.1 The basis of the $\sigma^* - V^*$ model

By means of finite element simulations, the stresses and strains in a cracked specimen or structure can be calculated. The aim of a local approach model, such as the σ*-V* model mentioned in Chapter 2, is to predict the onset or probability of fracture from

the calculated local stress/strain fields around a crack. While requiring heavy computer calculations, two great advantages make the σ*-V* model very promising and powerful. First, geometry and size effects are intrinsically included in the model, which allows a direct transfer of laboratory data to real structures. Second, the critical parameters of this model are usually almost independent of temperature over a wide temperature range, including the ductile-to-brittle transition range [1], even when the critical stress intensity factor K_{Jc} varies strongly in that temperature range.

The maximum principal stress, σ_1, is defined as usual as the highest eigenvalue of the stress tensor. The stressed volume, V*, is defined as the volume of material where the maximum principal stress, σ_1, is greater than σ* ($\sigma_1 > \sigma^*$). For a given specimen geometry, V* is function of: σ*, the material constitutive properties $\sigma(\varepsilon,\dot{\varepsilon},T)$ and the applied stress intensity factor K_J.

$$V^* = f\left[\sigma^*, \sigma(\varepsilon,\dot{\varepsilon},T), K_J\right] \tag{5.1}$$

In this work, the material constitutive properties were defined by two elastic constants, the Poisson's coefficient ν and the Young's modulus E, which weakly depend on temperature, as well as by the plastic flow curve Eq. (5.2), which in principle depends on the strain rate, temperature and irradiation conditions.

$$\sigma(\varepsilon_{pl}) = \sigma(\varepsilon_{pl},\dot{\varepsilon}_{pl},T,irradiation) \tag{5.2}$$

The σ*-V* local approach model is based on the following assumptions:

- Brittle fracture of the specimen occurs with a certain probability when V*, related to σ*=σ*$_c$, reaches a critical value called V*$_c$. The material properties are then the critical parameters, σ*$_c$ and V*$_c$.

- These parameters are usually considered temperature independent in the transition range. Note however that a weak temperature dependence of σ*$_c$

above room temperature has been suggested to account for the invariant shape of the master-curve after irradiation [1].

This σ*-V* brittle fracture local approach model, originally developed by Odette and co-workers, has been successfully used by those authors to estimate the ductile-to-brittle transition temperature in the F82H-mod tempered martensitic steels [2], to model irradiation embrittlement [3] and constraint loss size effects in pressure vessel ferritic steels [4].

In the framework of this PhD work, the σ*-V* model was considered: i) to investigate the effects of σ* and V* on the shape of the toughness-temperature curve with plane-strain 2D simulations, ii) to quantify the constraint loss effect of tempered martensitic steels with 3D-simulations, iii) to assess the transferability of the σ*-V* model to notched tensile specimens and also iv) to assess the transferability to tensile specimens for the Eurofer97 steel. The results of these investigations have been published respectively in [5] [6] [7] [8] and are presented in the following sections 5.2 5.3   5.4   and 5.5   below.

5.1.2   Implementation of the $\sigma^* - V^*$ model

2D simulations:

The 2D plane-strain simulations can be used to model only the testing conditions for which the stress-state at the vicinity of the crack tip corresponds essentially to plane-strain conditions. Therefore, the use of these simulations was restricted to model the deformation levels corresponding to the toughness lower bound only, where the out-of-plane constraint loss is the more limited and the stress-state is expected to mainly derive from quasi plane-strain conditions. Note that for 2D simulations, we define an area A^* related to V^* such as: $A^* B = V^*$ with B being the specimen thickness.

These 2D finite element calculations were performed using ABAQUS/Standard 6.6 which solves the nonlinear equilibrium equations. Since large deformation levels are

expected in the region near the crack tip, a finite strain ("large displacements theory") approach was used. 2D plane strain quadrilateral linear elements with reduced integration were used. This type of elements are the appropriate selection for fracture mechanics studies due to its inherent advantages to model problems involving high level of plastic deformation, as it is the case in the crack tip region.

Due to symmetry considerations, only half of the specimen was modeled. Symmetric boundary conditions were applied on the crack plane. The loading of the model was carried out through the displacement of a rigid pin in contact (frictionless) with the specimen. In this way, the applied load can be easily obtained from the reaction force acting on the rigid body. The crack tip in the non-deformed configuration was represented as a small notch having a finite root radius ρ_o. To study different load levels, C(T) meshes were constructed having different initial notch radius ρ_o. In all the cases the characteristic size of the crack tip elements was $\rho_o / 20$, which typically corresponds to element size in the range of hundredths to tenths of μm^2 for the elements at the crack tip. Following McMeeking [9], a solution independent of the initial notch geometry is eventually attained provided that the crack tip opening displacement, CTOD, exceeds five times the initial root radius. The results presented hereafter correspond to specimens for which this criterion is fulfilled.

The J-integral was determined using the contour integral evaluation provided with ABAQUS/standard 6.6, which calculates the J-integral over a predefined number of contours around the crack tip. The J-values reported here correspond to those measured over the contours far enough from the crack tip (to avoid the large deformation region where a J-integral path-dependence exists) and for which the J-integral estimates over the different contours were found to be constant.

The stress/strain fields ahead of a crack tip for the plane strain and elastic-plastic case were also simulated in small-scale yielding (SSY) conditions. A fully circular model, based upon the pure boundary layer model (i.e. T stress = 0) that also contains a small notch radius ρ_o in the middle was built, in a quite similar way as the semi-circular model described in [10]. The opening of the crack was performed in mode I by

imposing the standard elastic displacements, Δx and Δy, of the nodes on the outer circular boundary and considering a T-stress equal to zero. Δx and Δy are written:

$$\Delta x = K \frac{1+\upsilon}{E} \sqrt{r/2\pi} \cos\left(\frac{\theta}{2}\right)(3 - 4\upsilon - \cos\theta) \qquad (5.3)$$

$$\Delta y = K \frac{1+\upsilon}{E} \sqrt{r/2\pi} \sin\left(\frac{\theta}{2}\right)(3 - 4\upsilon - \cos\theta) \qquad (5.4)$$

where r is the radial distance from the crack tip and θ is the angle between the crack plane and the direction to the node, ν is the Poisson's ratio and E the Young's modulus. Note that the imposed displacements scale with the applied stress intensity factor K. The simulations were also run such that the crack tip opening displacement δ assures that the ratio δ/ρ_o is larger than five.

3D simulations:

In order to study the loss of constraint that are responsible for the strong size effect observed in the experiments performed in the upper transition temperature region, three dimensional finite element simulations of the C(T) specimens tested at -60 ºC were performed. At this temperature the small (0.35T) specimens underwent large deformations before breaking. In this case the stress fields calculated with 2D plane strain simulations are not representative of the real stresses due to out-of-plane constraint loss. Only 3D simulations are suitable to simulate properly these large deformations. The code used for these simulations was ABAQUS/Standard 6.7. Symmetric boundary conditions allow solving only one quarter of the specimen reducing the number of elements of the model by a factor four and the calculation time by a factor even greater than four. 8-node linear brick elements were used. Plastic deformation was included in the model, the material properties were considered isotropic, the Young modulus was E=212.5 GPa, the Poisson ratio ν=0.33 and the plastic flow curve corresponds to the one plotted in Figure 5-1. A general view of the specimen along with the mesh is depicted in Figure 5-2. The specimen was loaded by imposing the displacement to a frictionless rigid body pin, with the

same diameter of the pin used in the experiments. The provision for the clip gage in the specimen front face machined in the 0.35T specimens was also included in the numerical model. This allows comparing at the same position the displacement measured experimentally by the clip gage with the one obtained from the numerical simulations. The 0.87T (B=22mm) C(T) specimens and the 0.35T (B=9mm) C(T) specimens tested at -60 ºC had both an average crack length of approximately $a/W = 0.52$. This value of a/W was used for the 3D simulations.
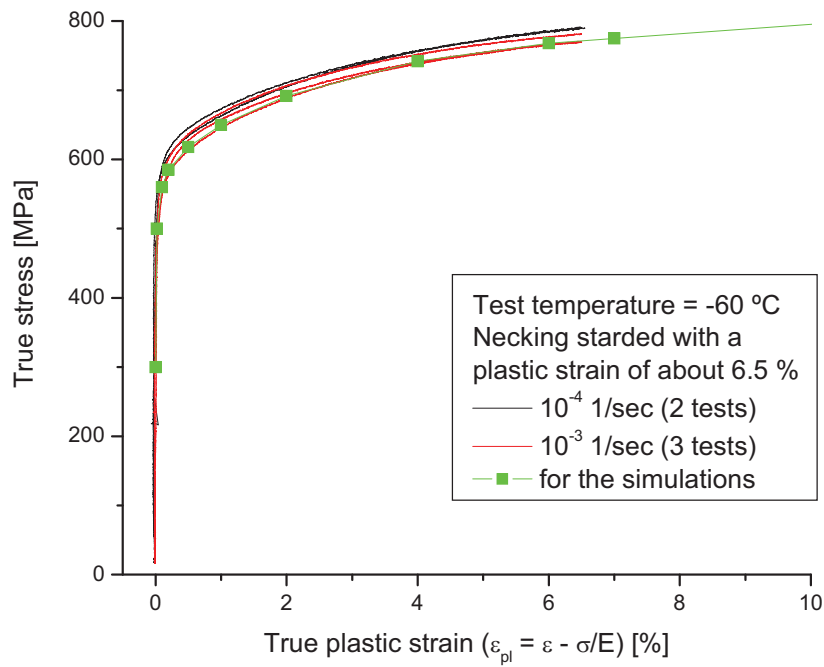

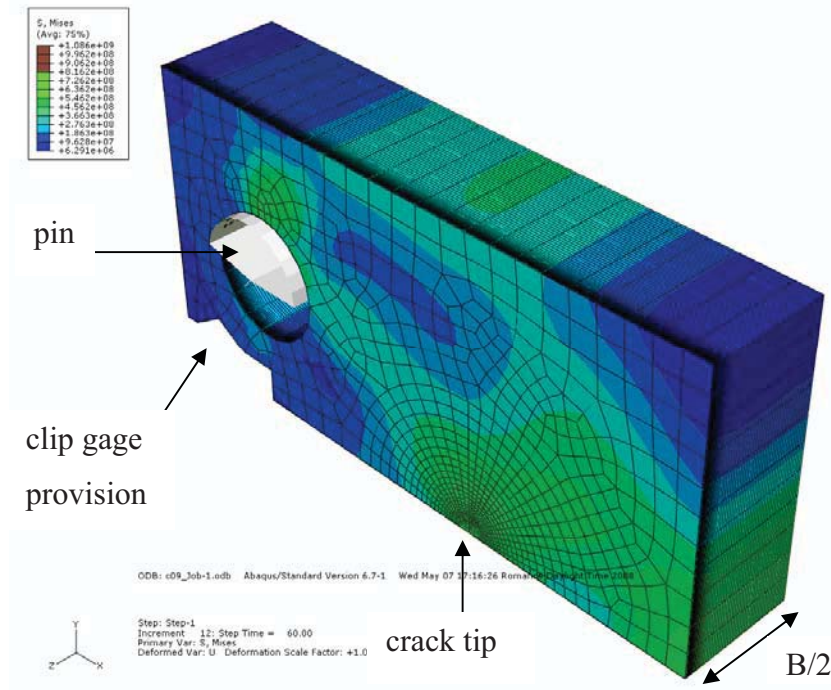**Figure 5-1**: Plastic flow curve of Eurofer97 steel at -60 ºC.

Figure 5-2: Finite Element model of the C(T) specimen. The loading pin and the clip gage provision are included in the model.

A finite initial crack tip radius (ρ_0) was used in the simulations. The effect of ρ_0 was studied using five models with different ρ_0/W ratios, namely $9000\rho_0/W = 1$, 2, 4, 8 and 16. The load-displacement curve was found to be independent of ρ_0 in the studied range. On the one hand, a large value of ρ_0 allows reaching large displacements of the pin without producing excessive deformation of the elements on the crack tip. On the other hand, for small loads, small values of ρ_0 are needed to have a good description of the stress fields close to the crack tip. This is shown and explained in detail in section 5.3   .
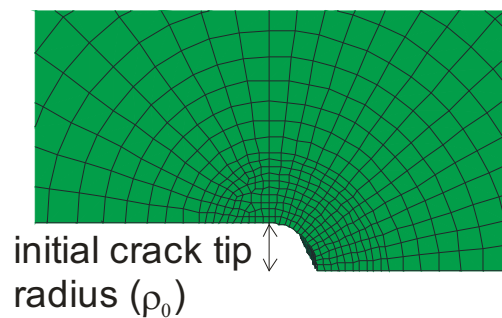

Figure 5-3: View of the Mesh close to the crack tip.

Determination of the stressed volume V*(σ*):

In order to calculate the stressed volume V* from a finite element simulation performed with ABAQUS, a post-processing program written in FORTRAN was developed. The input file of the program is a special output file of ABAQUS where, for instance, the nodes definition, the elements definition, the elements original and deformed volume and the value of the principal stress on each node are stored. After reading this information, the FORTRAN algorithm does the sum of the volume of all the elements where the maximum principal stress (σ_1) is higher than σ*. If an element has some of its nodes with $\sigma_1 > \sigma^*$ while the others are below, then only a fraction of the volume is added. For example, if 3 nodes of an 8-node element are above σ* then only 3/8 of the elements volume is added. This whole procedure is repeated for each time increment in order to obtain the stressed volume as a function of the load history for a given value of σ*. For 2D plane stress or 2D plane strain models, ABAQUS considers an arbitrary thickness defined by the user and calculates the volume of the elements using this information. In the case of an axis-symmetric model the volume also represents the real volume which is the ring shape volume formed by a revolution of the element around the symmetry axis.

5.2   C(T) specimens and small-scale yielding 2D simulations

5.2.1   2D simulation results

In this sub-section, we briefly report the numerical results, initially obtained by Bonadé [11] and Bonadé *et al.* [5], that will be used in next sub-section to describe the calibration procedure of the critical parameters: σ*$_c$ and A*$_c$.

The Figure 5-4 shows schematically the evolution of the enclosed area $A^*=A(\sigma^*)$ for different K_J values at a given temperature and for a given applied K_J level: A^* increases with decreasing σ^*.
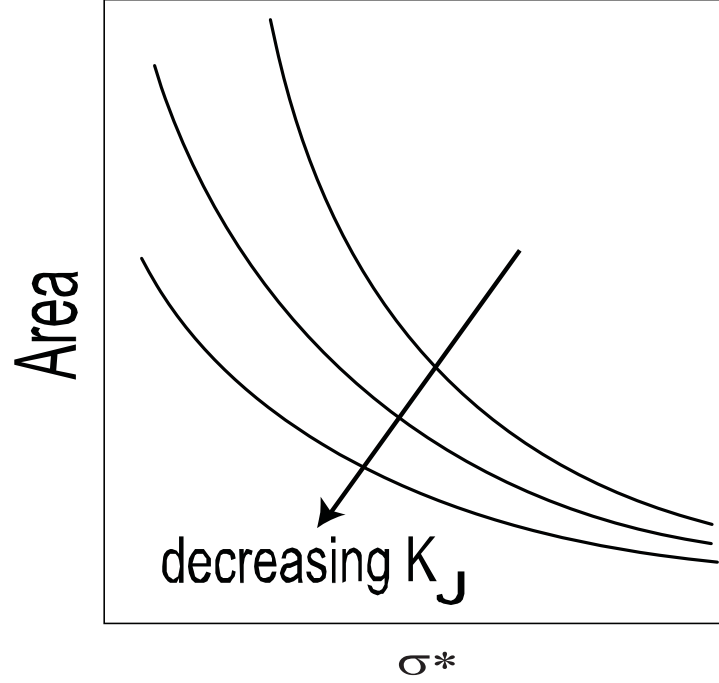

Figure 5-4: Schematic evolution of the area as a function of the principal stress level at a constant temperature. The effect of the loading level (represented here by K_J) is indicated in the plot.

A fundamental feature of the model is schematically presented in Figure 5-5, where the evolution of the A^* as a function of σ^* is plotted for three different cases. Each case is associated with a given temperature corresponding to fracture toughness level $K_{Jc}(T)$ defined at an arbitrary probability of fracture in the ductile-to-brittle temperature transition (DBTT) region (identical for all temperatures). Since the critical conditions are assumed to be temperature-independent, the three curves must intercept each other in a point labeled as (σ^*_c, A^*_c) in Figure 5-5. This point defines the critical conditions for cleavage fracture to occur. Naturally, the parameters of the model, σ^*_c and A^*_c, need to be calibrated in order to make the model predictions consistent with the experimental results. All the issues related to the calibration process are described in detail in next subsection.
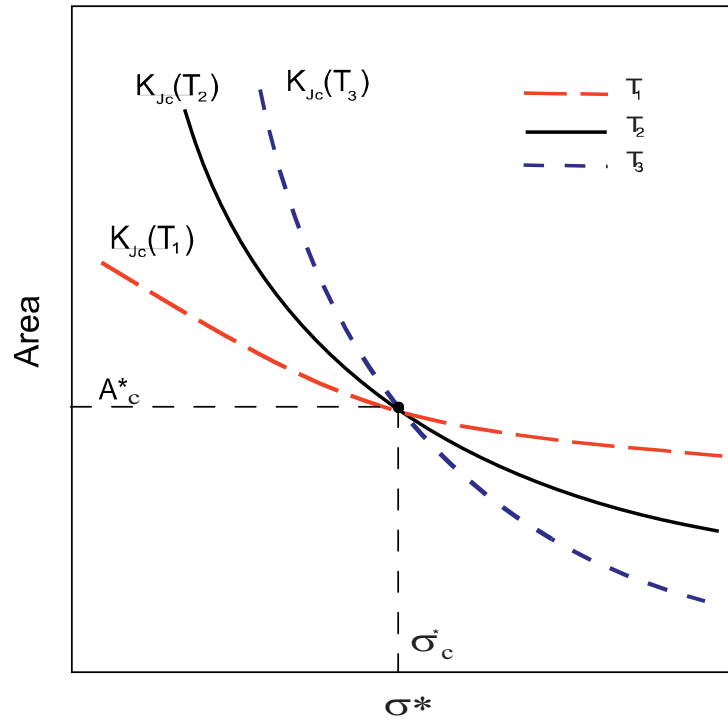
Figure 5-5: Expected evolution of the area $A*$ as a function of $\sigma*$ at different temperatures with the corresponding loading level, $K_{Jc}(T)$.
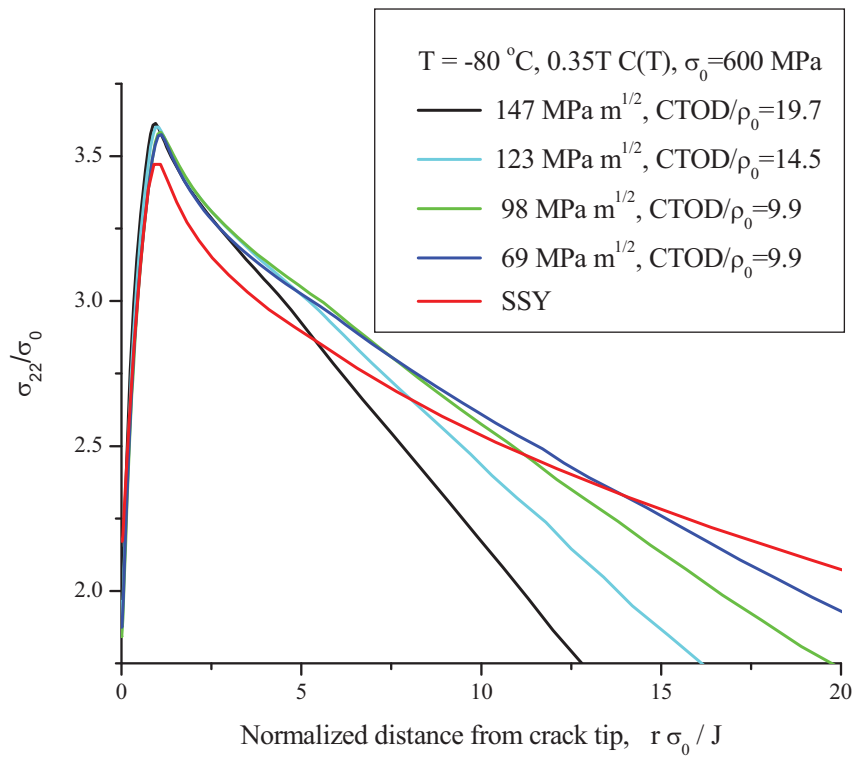

Figure 5-6: Comparison between SSY (T-stress = 0) and C(T) specimens calculations at T=-80°C. Note that r is the distance from the crack tip along the symmetry plane.

It has been shown by means of dimensional analysis for SSY conditions (T-stress =0) that the area enclosed by a given stress is proportional to the fourth power of K_J [12]. This fact is directly related to the self-similarity of the stress fields in the $r/J/\sigma_{0.2}$ non-dimensional space. However, in real fracture specimens, the stress fields in the crack tip region depart from this description. This point is illustrated in Figure 5-6 using a plane strain model for C(T) specimens at T = -80 °C, where the stress fields for different loading levels are plotted together with the corresponding SSY fields as obtained from the pure boundary layer problem $(T=0)$ as a function of $r/J/\sigma_{0.2}$. Figure 5-6 shows that in the region of the crack tip, the crack stress fields of C(T) specimens are significantly higher than those estimated for the SSY solution. This observation is consistent with the earlier observations made by Larsson and Carlsson [13] who already showed that the pure boundary layer solution of the elastic-plastic crack problem is not representative of a real crack problem. They showed that, in order to simulate correctly the stress field of a real specimen, the pure boundary layer formulation needs to be modified to take into account the non-singular T-stress that exists in the specimens. It is also well known that the C(T) specimens develop a positive T-stress upon loading, see for instance [14], so that the results in Figure 5-6 were indeed expected. In addition, O'Dowd and Shih [15] compared the results of simulations obtained with both the pure and modified boundary layer models and demonstrated the pronounced effect of the T-stress on the structure of stress field in the plastic zone. In particular, they found that a positive T-stress increases the σ_{22} value significantly. Therefore, it has to be recognized that the SSY calculations with T-stress = 0 cannot provide a reasonable estimate of the stress field of a real specimen. Nonetheless, for a real specimen, it is still possible to relate the area encompassed by a given stress to K_J through a power-law with exponent m, which may be different than the theoretical value equal to 4 for the pure layer model. Indeed, for a given temperature, the data obtained from the numerical simulations of the C(T) specimens have been fitted in the range of interest with the following general expression:

$$A^* = c \cdot K_J^m \qquad\qquad (5.5)$$

where c and m are constants that depend on temperature. The simulations have been run using [MPa] for stress unit and [abaqus unit] for length unit. Therefore, the dimension of the constant c is: $[c] = [MPa]^{1/m} [abaqus\ unit]^{2-m/2}$. To convert it in real units, one has to assign x microns per 1 abaqus unit ($[x]=[micron][abaqus\ unit]^{-1}$). In this case, the constant c_x reads:

$$c_x = x^{2-m/2}c \qquad (5.6)$$

The above equation shows that for $m=4$, the constant c is independent of the specimen size. For $m \neq 4$, the constant c in Eq. (5.6) becomes specimens size dependent so that we can scale it from one specimen size of width W_1, to another of width W_2, yielding:

$$c_{W_1} = c_{W_2} \left(\frac{W_1}{W_2} \right)^{(2-m/2)} \qquad (5.7)$$

Note that this size effect has nothing to do with the statistical size effect associated with the crack front length, but it is only mediated by the effect of the in-plane geometry of the specimens on the stress fields.

The numerical results presented in this section correspond to a 0.35T C(T) specimen. Eq. (5.5) was observed to adjust the numerical data, in the K_J-range of interest, for all the temperatures considered here. Note that the exponent m in Eq. (5.5) takes values a little greater than 4 for all the temperatures tested (from -50°C down to -196°C). The numerical results are summarized in Table 5-1 and Table 5-2. As an example, in Figure 5-7, the dependence on the K_J of the area A^* encompassing a maximum principal stress of 2000 MPa is plotted in a *log-log* diagram. Note that for this simulation, the transient associated with the blunting of the initial root radius up to CTOD/ρ_o>5 lasts up to 68 MPam$^{1/2}$. One can clearly see that in the loading range 68 to 100 MPam$^{1/2}$ the *log(A*)-log(K_J)* curve can be approximated by a linear relation whose slope is larger than 4 and which is likely to result from the growing T-stress effect in the initial loading as discussed above. Beyond about 100 MPam$^{1/2}$, the slope goes down indicating that in-plane constraint loss has started.

Temp.	Maximum principal critical stress [MPa]										
	2200	2150	2100	2070	2050	2030	2000	1970	1950	1930	1900
-50°C				2.61E-07	7.35E-07	1.39E-06	2.88E-06	5.13E-06	7.38E-06	1.01E-05	1.58E-05
-80°C			2.76E-07	1.48E-06	2.77E-06	4.60E-06	8.09E-06	1.40E-05	2.04E-05	2.65E-05	4.33E-05
-90°C			1.55E-06	3.45E-06	5.15E-06	7.29E-06	1.18E-05	2.00E-05	3.11E-05	3.95E-05	6.71E-05
-100°C	2.31E-06	5.27E-06	1.11E-05	1.66E-05	2.06E-05	2.64E-05	3.52E-05	4.53E-05	5.38E-05	6.40E-05	7.61E-05
-120°C	1.06E-05	2.00E-05	3.39E-05	4.44E-05	5.25E-05	6.20E-05	7.58E-05	9.26E-05	1.05E-04	1.18E-04	1.40E-04
-145°C	8.10E-05	1.84E-04	3.36E-04	4.67E-04	5.68E-04	6.88E-04	8.93E-04	1.10E-03	1.34E-03	1.57E-03	1.95E-03
-160°C	6.45E-04	8.75E-04	1.27E-03	1.58E-03	1.82E-03	2.08E-03	2.53E-03	3.03E+03	3.40E-03	3.80E-03	4.44E-03
-196°C	4.69E-03	5.51E-03	6.79E-03	6.65E-03	7.44E-03	8.52E-03	9.05E-03	9.60E-03	1.04E-02	1.02E-02	1.50E-02

Table 5-1: c coefficient in Eq. **(5.5)** for 0.35T C(T) specimens. $A^*/2 = c\, K^m$.

Temp.	Maximum principal critical stress [MPa]										
	2200	2150	2100	2070	2050	2030	2000	1970	1950	1930	1900
-50°C				4.5	4.5	4.5	4.5	4.5	4.5	4.5	4.5
-80°C			4.97	4.78	4.74	4.71	4.71	4.69	4.67	4.67	4.65
-90°C			4.79	4.75	4.74	4.75	4.75	4.70	4.68	4.68	4.63
-100°C	4.61	4.61	4.61	4.61	4.61	4.61	4.61	4.61	4.61	4.61	4.61
-120°C	4.61	4.61	4.61	4.61	4.61	4.61	4.61	4.61	4.61	4.61	4.61
-145°C	4.59	4.46	4.41	4.36	4.34	4.32	4.29	4.27	4.25	4.23	4.21
-160°C	4.30	4.26	4.23	4.21	4.19	4.18	4.15	4.13	4.12	4.10	4.08
-196°C	3.96	3.95	3.93	3.95	3.93	3.91	3.91	3.91	3.90	3.92	3.84

Table 5-2: m coefficient in Eq. **(5.5)** for 0.35T C(T) specimens. $A^*/2 = c\, K^m$.
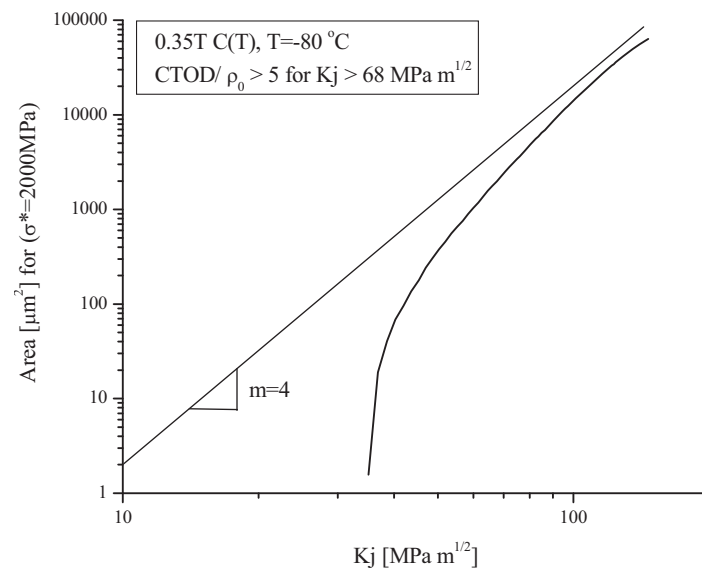

Figure 5-7: $A^*(K_J)$ curve at -80°C for a maximum principal stress equal to 2000 MPa.

5.2.2   Determination of the critical parameters and application to the reconstruction of the fracture toughness lower bound

As mentioned in before, the toughness lower bound, $K_{Jc(LB)}(T)$, is a fitted curve that, in the framework of the ASTM E1921-08 approach, corresponds to a given probability of fracture, typically 1%. Note that the choice of the lower bound is not unique. In principle, several $K_{Jc(LB)}(T)$ curves could be considered; for example the lower bound of the ASME approach would be a reasonable alternative. However, in the following and for the sake of clarity, the discussion is restricted to the reconstruction of the $K_{Jc(LB)}(T)$ of the "modified master-curve" as discussed in Chapter 4. The numerical results analyzed here include FE simulations for three temperatures in the lower shelf (-196°C, -160°C and -145°C) and five temperatures in the DBTT region (-120°C, -100°C, -90°C, -80°C, and -50°C).

In virtue of Eq. (5.5) and recalling the results presented in Table 5-1 and Table 5-2, it is possible to plot the *A*(σ*)* curves at different loading conditions represented by K_J. This process is repeated at all temperatures simulated. In order to determine the critical values (σ^*_c, A^*_c), one can start the calibration procedure by using the $K_{Jc(LB)}(T)$ values as loading parameter to plot the *A*(σ*)* curves at the considered temperatures. By doing so, one observes that the resulting *A*(σ*)* curves do not display a well-defined crossover point as discussed ideally in Figure 5-5. As a matter of fact, only the *A*(σ*)* curves at -196 °C, -160 °C and -146 °C (the red curves in Figure 5-8), corresponding to the lower shelf, are significantly off the intersection point defined by the black curves around 2000 MPa. However, it has to be emphasized that the load levels at which these two red curves are plotted correspond to extrapolation of the lower bound fit, which describes the data essentially in the transition, down to the lower shelf. Therefore, it is quite plausible that these extrapolations slightly overestimated the toughness level of the lower shelf. As a result, the *A*(σ*)* curves may be not correctly placed in the plot of the Figure 5-8. A change in the fracture controlling mechanism between the transition and lower shelf

region is another possible explanation for not having the lower shelf $A*(\sigma*)$ curve intersecting the other curves properly. Furthermore, it is important to outline that the locus of the curves in the $A*(\sigma*)$ space is extremely sensitive to the load level K_{Jc}. Indeed, Eq. (5.5) predicts a strong dependence of A on K_{Jc} such that a very small variation in K_{Jc} shift significantly the $A*(\sigma*)$ curve along the vertical axis.
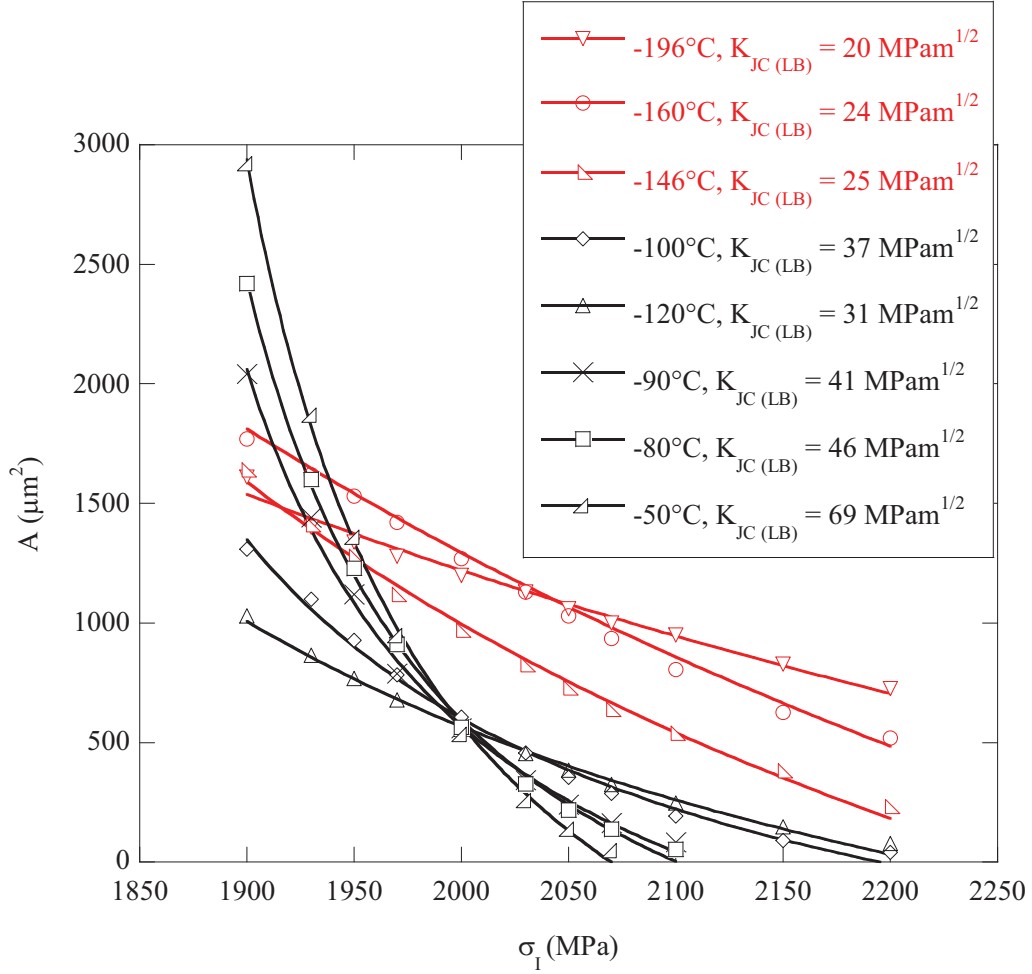

Figure 5-8: $A*(\sigma*)$ curves plotted at the load levels corresponding to $K_{Jc(LB)}(T)$ of the modified master-curve.

The effect of the critical values $(\sigma*_c, A*_c)$ on the shape of the $K(T)$ curves are exemplified in Figure 5-9 where two values of $\sigma*_c$ and two of $A*_c$ have been selected, namely $\sigma*_c$ =1950/2050 MPa and $A*_c$ = 500/4250 mm². With these values, four $K(T)$ curves have been reconstructed using all possible combination of $(\sigma*_c, A*_c)$. The most salient observations are related to the curvature of the $K(T)$ curve and to the

vertical position of the curve at the lower shelf. Indeed, an σ^*_c increase at a given A^*_c makes the curve rise much faster with increasing temperatures; this fact is illustrated by considering either the two black or the two red curves respectively. Similar conclusions were drawn by Ortner in [16]. The effect of a change in A^*_c at constant σ^*_c can be seen by comparing the curves with the circle and square symbols respectively. An increase of A^*_c yields a significant increase of fracture toughness on the lower shelf while the shape of the $K(T)$ curve remains little affected.
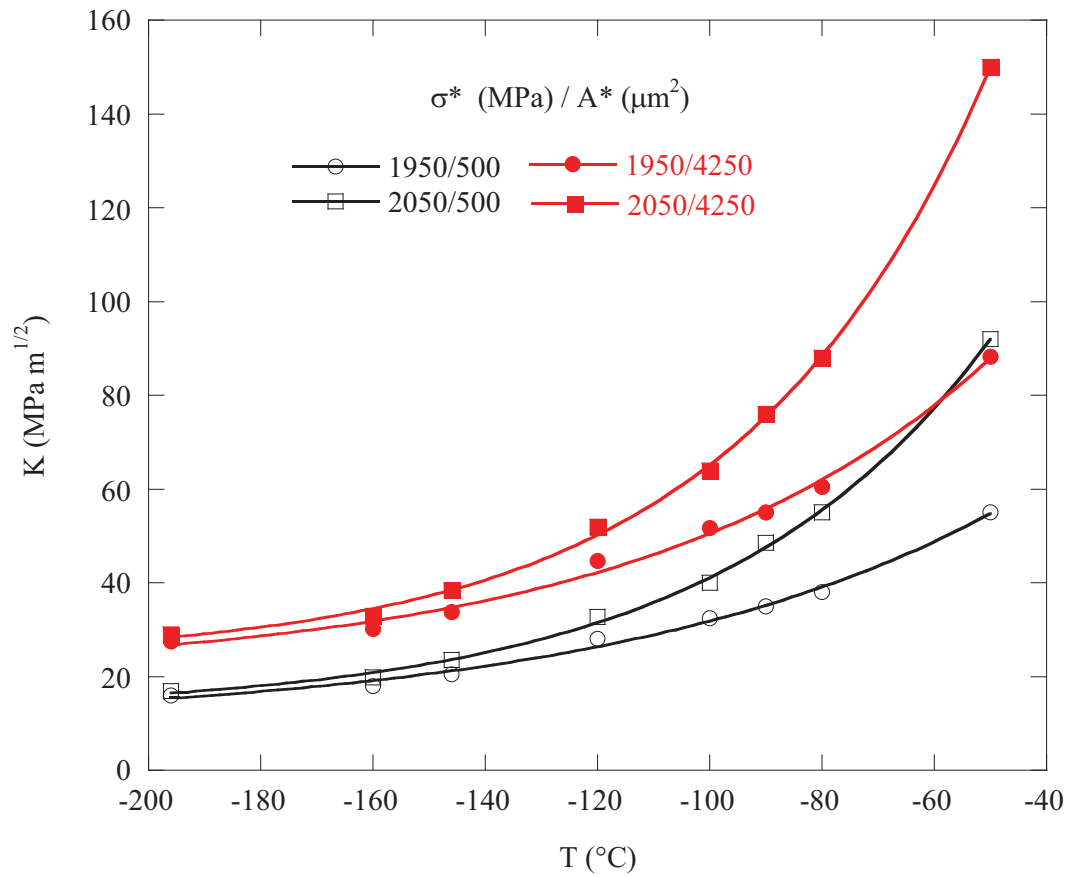

Figure 5-9: Illustration of the effect of the (σ^*_c, A^*_c) values on the shape of the K(T) curve.

It has also been found that several sets of (σ^*_c, A^*_c) values can be used to satisfactorily reconstruct the experimental $K_{Jc(LB)}(T)$ curve. All these "correct" pairs of critical values define a window that represents the uncertainty in the calibration process as a consequence of the experimental and numerical uncertainties in addition to the intrinsic uncertainties of the model. In Figure 5-10, we plot the experimental data, the experimental $K_{Jc(LB)}(T)$ curve as well as five different pairs of (σ^*_c, A^*_c)

calibrated according to the procedure described above and that were found to reconstruct rather well the $K_{Jc(LB)}(T)$ curve. It has to be emphasized that the critical stress σ^*_c is practically constant for each pair, and equal to 1955 ± 15 MPa while the uncertainty in the critical area A^* remains quite large 1100 ± 300 μm². It is emphasized that the model predicts the very weak temperature-dependence on the lower shelf of fracture toughness values. This observation is remarkable, considering that the maximum rate of variation in $\sigma_{0.2}$ with the temperature is actually observed in this temperature range. In Figure 5-11 the model predictions corresponding to the best estimate critical parameters are plotted along with the complete fracture dataset and the fracture lower bound.
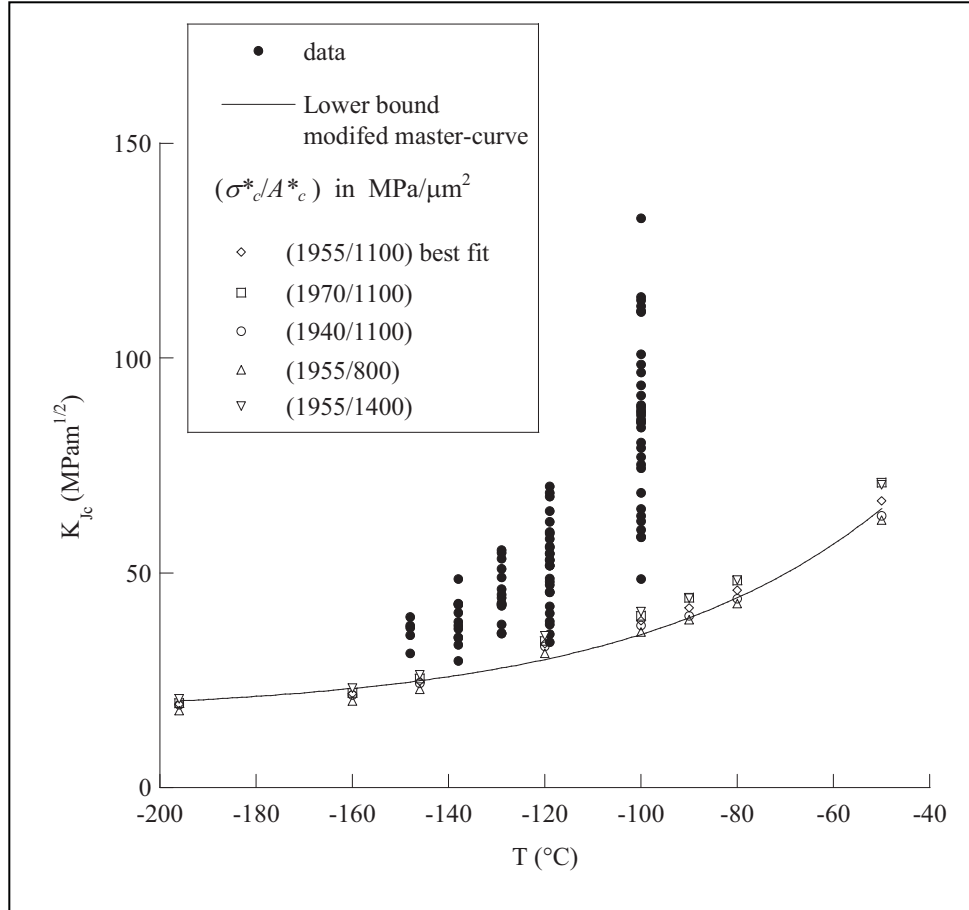

Figure 5-10: Reconstruction of the lower bound, $K_{Jc(LB)}(T)$, with different sets of criteria (σ^*_c, A^*_c)
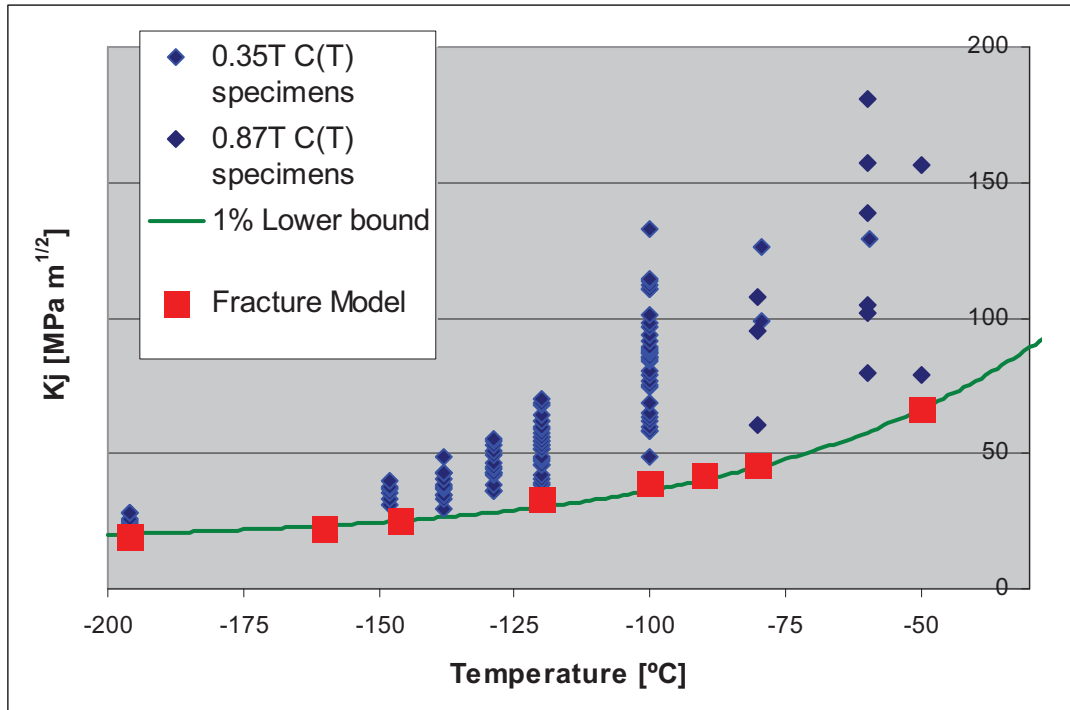
Figure 5-11: Best fit model prediction along with the fracture toughness data.

5.2.3   Summary

From two dimensional finite element simulations of C(T) specimens performed at several temperatures, it was shown that the experimental lower bound of the data can be modeled by means of a critical stress-critical area ($\sigma^* \text{-} A^*$) local criterion. The calibration procedure to determine the parameters σ^*_c and A^*_c was described and ultimately applied. The shape of the engineering lower bound $K_{Jc(LB)}(T)$ was shown to be essentially mediated by the σ^*_c value while the A^*_c value sets the position of the $K_{Jc(LB)}(T)$ curve in the $K(T)$ space. The uncertainty in the determination of the critical parameters was discussed. In particular, we showed that the critical stress is rather well defined. Due to the relatively low sensitivity of the critical area, even a rough estimation of this critical parameter is enough to predict fracture toughness with the σ^*-A^* local approach model. On the other hand it is necessary to have a good estimation of the critical stress.

5.3   C(T) specimens 3D simulations

5.3.1   Load-displacement curves

In Figure 5-12 we compare the experimental and simulated load-displacement curves for the 0.35T size specimens. As mentioned before, the displacement of these specimens was measured with a clip gage. The specimen chosen for the comparison was one with an average load-displacement curve (see Figure 5-13). As shown in Figure 5-12, there is very good agreement with the experimental data for openings below 1 mm. Fractographic observations of the broken specimens showed that a small amount of ductile tearing occurred for specimens that passed maximum load. At openings larger than 1 mm, ductile tearing starts on the real specimen, the crack starts to grow in a stable manner and the load reaches a maximum, decreasing afterwards. This stable crack growth was not modeled. In this work, only the simulations of specimens breaking before maximum load were considered. They reproduce the loading of a specimen with a stable blunting crack under increasing load. Thus, the stress fields analyzed in this work correspond to those of the specimens representative of the lower part of toughness distribution (below maximum load). We can also see in Figure 5-12 that there is no appreciable effect of the initial crack tip root radius, ρ_0, on the load-displacement-curve.
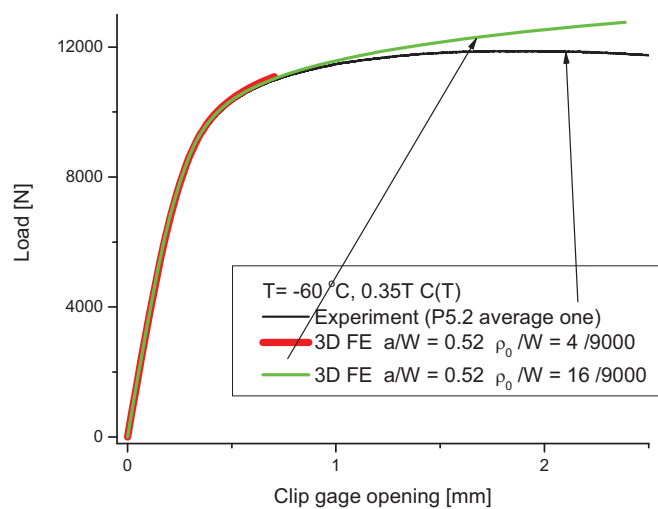

Figure 5-12: Experimental and numerical load – displacement curves.
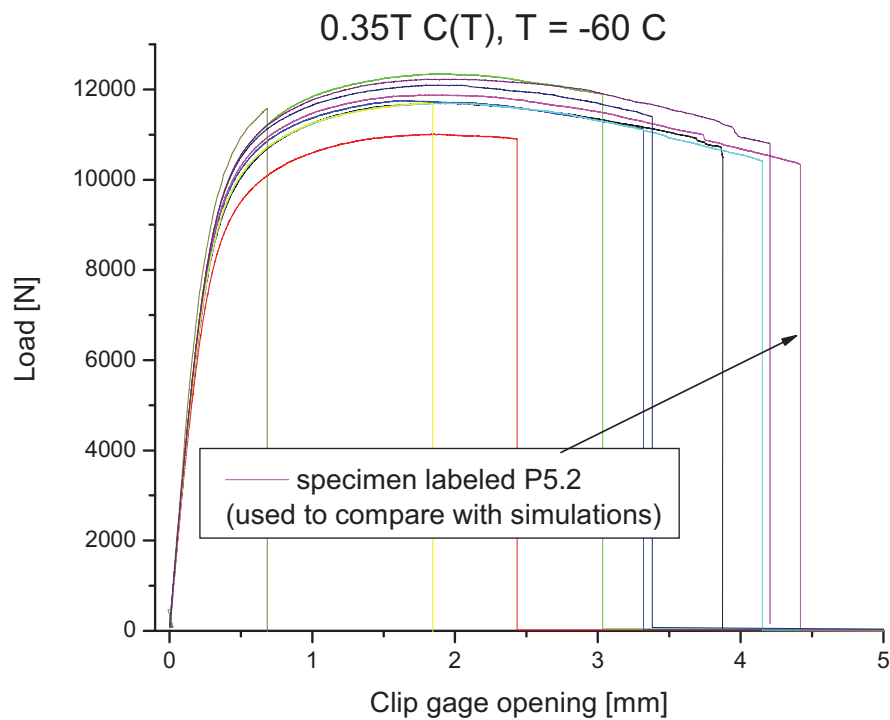
Figure 5-13: Load - displacement curves of the specimens measured with an attached clip gage.

For the 0.87T C(T) specimens the displacement of the mobile machine traverse was measured. The pin displacement was obtained performing the compliance correction of the machine. Figure 5-14 compares the 0.87T simulations and experiments. Again we found very good agreement between them. An experiment performed at a temperature of 10 degrees higher is also included in the Figure. This specimen broke after more deformation giving an idea of the load-displacement curve we would get with a tough specimen at -60 ºC. The breaking points of the experiments can also be seen in the figure.

Figure 5-14: Experimental and numerical load-displacement curves for the 0.87T specimens.

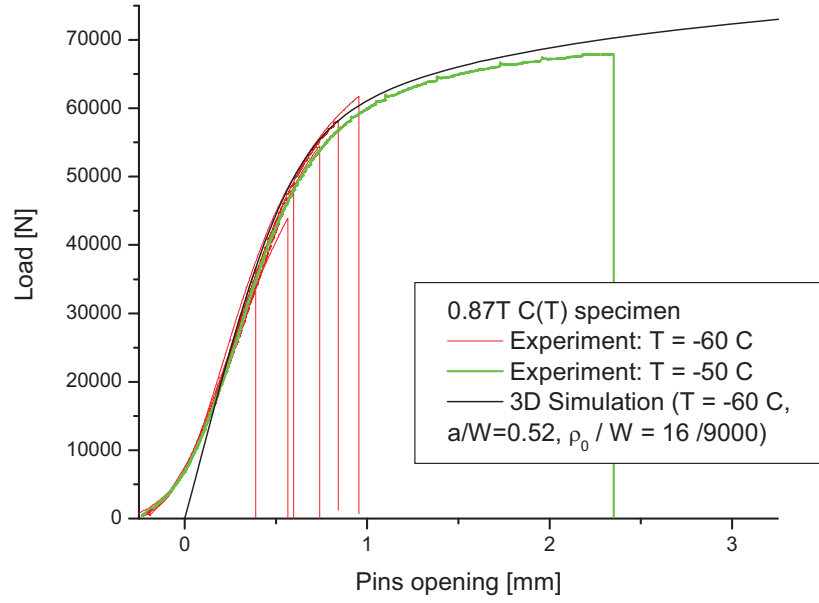Experimentally, the stress intensity factor K_J was calculated using the ASTM standard procedure [17]. Since the simulated curves were shown to reconstruct very well the experimental ones, the K_J values reported in this work were calculated with these same equations from the calculated curves (equations (4.1) to (4.5) in Chapter 4). It has been verified as well that these last K_J values are consistent with the K_J values obtained by calculating the specimen thickness average of the J-integral.

5.3.2   Effect of the constraint loss effect on measured toughness within the framework of σ* - V* model

Here we study the toughness increase predictions of the σ*-V* local approach model applied to the 3D simulations. We recall that the stressed volume V* is function of σ* and the applied stress intensity factor K_J, Eq. (5.2).

In Figure 5-15 we show the stressed volume V* for σ*=1500 MPa. V* was calculated from five different simulation models with different initial crack tip radius ρ_0. We see that after a short transient, V* becomes practically independent of ρ_0. This transient decreases when ρ_0 is decreased converging to the case of an initial sharp crack tip

when $\rho_0 \to 0$. In Figure 5-16 we see the same plot as before but with σ^*=1900 MPa. For higher values of σ^*, the effect of ρ_0 lasts longer, in terms of loading, because the volume of material under high stress is confined closer to the crack tip, where the influence of ρ_0 is more pronounced.
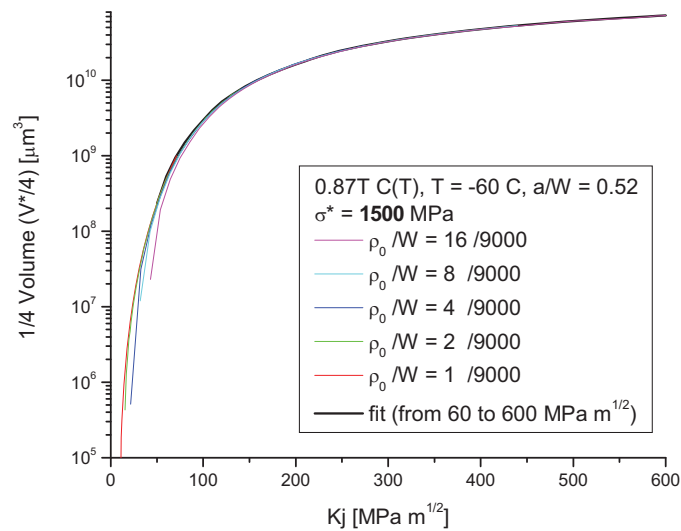

Figure 5-15: Volume of the specimen where the maximum principal stress is higher than 1500 MPa in function of the applied K_J.
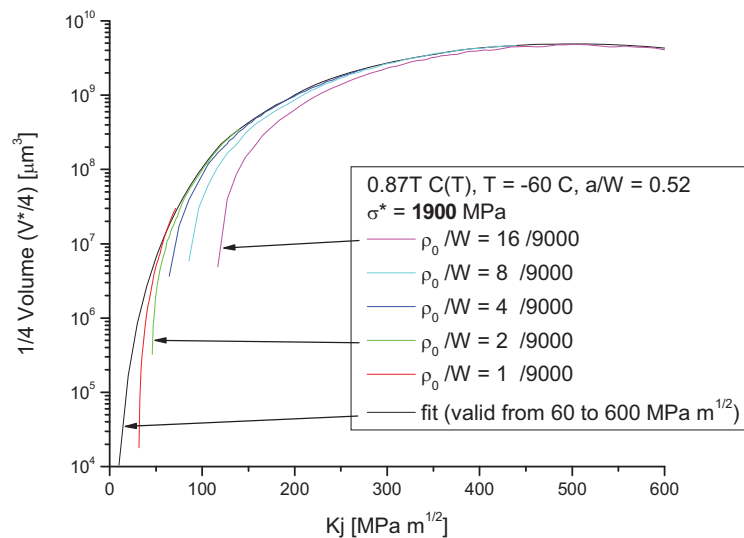

Figure 5-16: Volume of the specimen where the maximum principal stress is higher than 1900 MPa in function of the applied K_J.

For the application of the fracture model explained below, we considered only the segments of the $V^*(K_J)$ curve that appeared to be independent of ρ_0. The stressed volume V^* as a function of K_J was piecewise fitted for each value of σ^* used in this work. The fitted functions obtained are presented in the following tables.

Volume Function in $[10^{-3}\ \text{mm}^3]$	Fitting range in $[\text{MPa m}^{1/2}]$
$\frac{1}{4}V^* = 1204(K/71.2)^{2.9} - 200$	$55 < K < 120$
$\frac{1}{4}V^* = 0.2789K^2 + 49.73K - 4845$	$100 < K < 250$
$\frac{1}{4}V^* = -0.0783K^2 + 202.1K - 20705$	$240 < K < 600$

Table 5-3: Fitted stressed Volume V^* as a function of K_J **for $\sigma^* = 1500$ MPa** (0.87T C(T)).

Volume Function in $[10^{-3}\ \text{mm}^3]$	Fitting range in $[\text{MPa m}^{1/2}]$
$\frac{1}{4}V^* = \frac{8.2}{10^6}K^{3.8}$	$60 < K < 100$
$\frac{1}{4}V^* = 400(K/100)^{2.8} - 80$	$90 < K < 155$
$\frac{1}{4}V^* = 0.0576K^2 + 7.19K - 1221$	$150 < K < 300$
$\frac{1}{4}V^* = -0.07(K - 600)^2 + 12500$	$290 < K < 600$

Table 5-4: Fitted stressed Volume V^* as a function of K_J **for $\sigma^* = 1800$ MPa** (0.87T C(T)).

Volume Function in $[10^{-3}\ \text{mm}^3]$	Fitting range in $[\text{MPa m}^{1/2}]$
$\frac{1}{4}V^* = \frac{1.05}{10^6}K^4$	$58 < K < 120$
$\frac{1}{4}V^* = \frac{127}{10^6}K^3$	$120 < K < 200$
$\frac{1}{4}V^* = 17(K - 200) + 1000$	$190 < K < 385$
$\frac{1}{4}V^* = -0.06(K - 500)^2 + 4900$	$350 < K < 600$

Table 5-5: Fitted stressed Volume V^* as a function of K_J **for $\sigma^* = 1900$ MPa** (0.87T C(T)).

Volume Function in $[10^{-3}\ \text{mm}^3]$	Fitting range in $[\text{MPa m}^{1/2}]$
$\frac{1}{4}V^* = \frac{0.47}{10^6}K^4$	$60 < K < 135$
$\frac{1}{4}V^* = \frac{63}{10^6}K^3$	$135 < K < 250$

$\frac{1}{4}V^* = 10K - 1500$	$250 < K < 380$
$\frac{1}{4}V^* = -0.05(K - 450)^2 + 2550$	$360 < K < 600$

Table 5-6: Fitted stressed Volume V* as a function of K_J **for σ* = 1955 MPa** (0.87T C(T)).

Volume Function in $[10^{-3}\ mm^3]$	Fitting range in $[MPa\ m^{1/2}]$
$\frac{1}{4}V^* = \frac{0.22}{10^6} K^4$	$68 < K < 142$
$\frac{1}{4}V^* = \frac{19}{10^6} K^{3.1}$	$138 < K < 275$
$\frac{1}{4}V^* = 5.6(K - 275) + 702$	$275 < K < 390$
$\frac{1}{4}V^* = -0.04(K - 430)^2 + 1400$	$360 < K < 600$

Table 5-7: Fitted stressed Volume V* as a function of K_J **for σ* = 2000 MPa** (0.87T C(T)).

Before analyzing our 3D finite element simulations, we recall first that for plane strain and small scale yielding (SSY) conditions the stressed area, A*, has the following well known dependence on K_J:

$$A^* = cK_J^4 \tag{5.8}$$

where c is a constant that depends on σ* and constitutive properties. This equation is also the limit solution close to the crack tip for a specimen with a sharp crack under a low applied K_J, i.e., when the plastic zone size is much smaller than the characteristic specimen dimensions, ligament and crack front length. If we apply the σ*-V* model to this case with a specimen of thickness B then:

$$V^* = BA^* = BcK_J^4 \tag{5.9}$$

If a specimen of thickness B_1 breaks with a stress intensity factor K_{J1} then a specimen of thickness B_2 will reach the same critical volume for K_{J2}:

$$V^* = B_1 cK_{J1}^4 = B_2 cK_{J2}^4 \tag{5.10}$$

This gives a size effect of the form:

$$\frac{K_{J2}}{K_{J1}} = \left(\frac{B_1}{B_2}\right)^{1/4} \tag{5.11}$$

Note the similarity with the ASTM size adjustment Eq. (5.12). Equation (5.11) is practically the same but without the minimum toughness K_{min}.

$$\frac{K_{J2} - K_{min}}{K_{J1} - K_{min}} = \left(\frac{B_1}{B_2}\right)^{1/4} \tag{5.12}$$

For large values of K_J, the SSY description of the stress fields does not hold anymore. In this case, the stress field close to the crack tip is influenced by the boundaries of the specimen so that it is not any more mediated by K_J only but also by the crack front length and ligament length. If two different specimen sizes/geometries are considered, referred as to #1 and #2 hereafter, V* associated with each specimen remains given by Eq. (5.1) but two different functions f characterize the K_J and σ^* dependence on V*:

$$\begin{aligned} V_1^* &= f_1(K_{J,1}, \sigma^*) & \text{specimen #1} \\ V_2^* &= f_2(K_{J,2}, \sigma^*) & \text{specimen #2} \end{aligned} \tag{5.13}$$

f_1 and f_2 are two functions that can be used to rescale fracture toughness data from one specimen size to another on the basis of the σ^*-V* model. Indeed, Eq. (5.13) can be inverted to express K_J as a function of the other two variables for each specimen size as:

$$\begin{aligned} K_{J,1} &= h_1(V_1^*, \sigma^*) & \text{specimen #1} \\ K_{J,2} &= h_2(V_2^*, \sigma^*) & \text{specimen #2} \end{aligned} \tag{5.14}$$

By making $V_1^* = V_2^* = V^*$, the scaling law between the two specimens then reads:

$$K_{J,2} = h_2(V^*, \sigma^*) = h_2(f_1(K_{J,1}, \sigma^*), \sigma^*) \tag{5.15}$$

In order to quantify this phenomenon of constraint loss, we rely on 3D numerical simulations to calculate the f_i functions (Table 5-3 to Table 5-7). In Figure 5-17 the stressed volume as a function of the stress intensity factor K_J for two specimen sizes is plotted for σ^*=1955 MPa. Note that this stress value was shown in last section and in [5] to be the critical stress that allows reconstructing the temperature dependence of the 1% failure probability curve of the master-curve. As can be seen in Figure 5-17, the stressed volume in a 0.35T C(T) specimen does not follow Eq. (5.9) for K_J higher than about 80 MPa m$^{1/2}$. This means that for a 0.87T C(T) specimen with K_J higher than about 60 MPa m$^{1/2}$ the model predicts a higher toughness increase to 0.35T than Eq. (5.11). In Figure 5-17 we also see that V* reaches a maximum. Because of this maximum it is impossible to reach with a 0.35T C(T) specimen the stressed volume that a 0.87T C(T) specimen has when K_J is higher than about 140 MPa m$^{1/2}$. This indicates that a strong toughness increase can be expected and possibly also a change in the fracture mechanism.
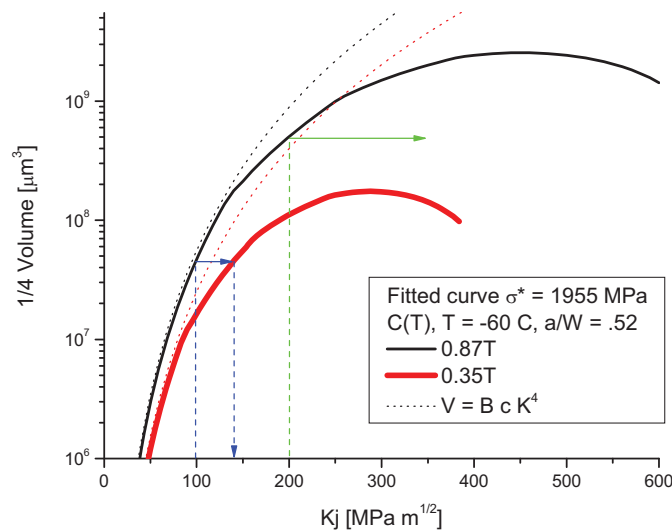
Figure 5-17: Model application example. A 0.87T size specimen that breaks at 100 MPa m$^{1/2}$ corresponds to a 0.35T specimen breaking at 140 MPa m$^{1/2}$. For a 0.87T specimen loaded to 200 MPa m$^{1/2}$ this critical condition cannot be reached by a 0.35T specimen, indicating that a large toughness increase is expected.

A parametric study of the model is shown in Figure 5-18 to illustrate the effect of the critical stress on the toughness scaling from 0.87T to 0.35T C(T) specimens. The

expected toughness increase ΔK_J from the 0.87T to 0.35T C(T) specimens is calculated using Eq. (5.15) that can be readily rewritten as:

$$\Delta K_J = K_{0.35T} - K_{0.87T} = h_2(f_1(K_{0.87T}, \sigma^*), \sigma^*) - K_{0.87T} \qquad (5.16)$$

Using Eq. (5.16), we calculated the toughness increase to 0.35T predicted by the model for the six 0.87T experimental values obtained, and we compare them with the ASTM prediction Eq. (5.12). Clearly the strong loss of constraint effect observed with the σ^*-V^* model is reflected by the experiments. We recall again that in principle this toughness model scaling is not intended to describe the probabilistic nature of cleavage.
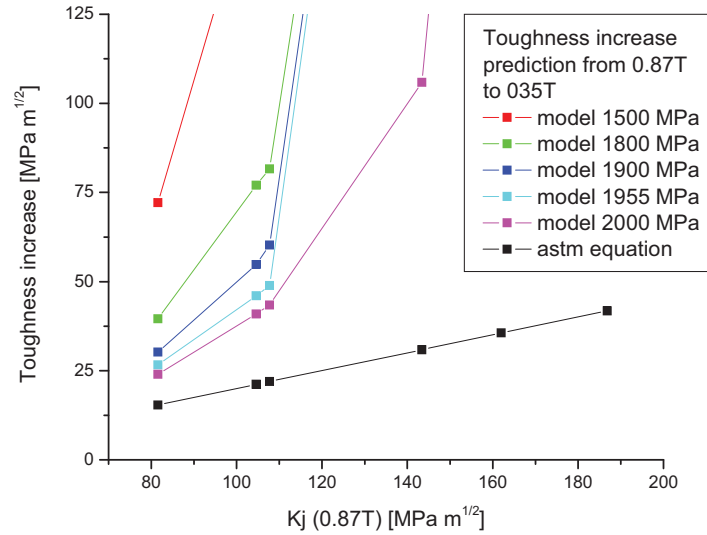
Figure 5-18: 0.87T to 0.35T toughness increase prediction of the σ^*-V^* model for different critical parameters along with the standard prediction.

5.3.3   Conclusions

In this section we studied the strong fracture size effect observed on our data of the reduced activation tempered martensitic steel Eurofer97 in the temperature range from -80 ºC to -40 ºC by means of 3D finite element simulations to study the predictions of the local approach type model called σ^* - V^*.

 - Even when the ASTM size requirements associated with M=30 were fulfilled well below the maximum limits, the 0.35T C(T) specimens yielded a 1T-adjusted toughness value much higher than the expected values.

 - It was shown that the 3D finite element simulations reproduced very well the load-displacement curves of the specimens up to the initiation of stable crack growth. No appreciable effect of the initial crack tip radius on the load-displacement curve was observed for the studied values, $\rho_0 / W < 16 / 9000$.

- The constraint loss effects on measured toughness were quantified using a critical condition for unstable fracture based on the attainment of a critical stress σ^* within a critical volume V^*. It was shown that special attention has to be paid to the effect of the initial crack tip radius, ρ_0 on V^*. Indeed, for small crack tip openings with values of σ^* close to the peak stress value, V^* depends on ρ_0. For low values of σ^*, V^* gets quickly independent of ρ_0 by increasing the applied K, even if the crack tip of the model is not blunted.

- The size effect predictions based on the σ^*-V^* model were found consistent with a strong size effect observed in the experiments. The size effect was found much larger than the B-adjustment recommended in the ASTM-E1921.

5.4   Notched specimens simulations

In order to check the transferability of the σ^*-V^* quasi-cleavage criterion to another specimen geometry, a series of tests with notched tensile specimens were carried out at four different temperatures, namely 20°C, -50°C, -100°C and -155°C. The last three temperatures correspond to the temperature range at which 0.35T C(T) pre-cracked specimens have been previously tested.

5.4.1   Load - deflection

As example, the load-displacement curves of the notched tensile specimen tested are shown in Figure 5-19. The curves calculated by finite element simulations are

indicated along with the experimental ones; an excellent agreement between them can be seen. The load-displacement curves are reported as a function of the displacement δ, which corresponds to the opening of the notch measured with a clip gage whose knives were symmetrically positioned at 5 mm on each side of the notch plane. In Figure 5-20, the radial variation of the maximum principal stress on the notch plane is plotted for different displacements, δ. At the beginning of the deformation (small δ values), a peak stress close to the notch tip is observed, somehow similar to the stress fields close to a crack tip. Note that, due to the triaxial stress state around the notch, the value of the critical stress σ* is larger than the average fracture stress determined by dividing the load by the actual minimum cross-section of a notched tensile or by the cross-section of a plain tensile specimen at the neck. At increasing deformation (opening of the notch), the height of the peak increases and the peak broadens until at large displacements the stress increases monotonously and reaches its maximum in the middle of the specimen. As a matter of fact, it was observed that at failure the stress distribution was always such that the maximum stress was located along the specimen axis.
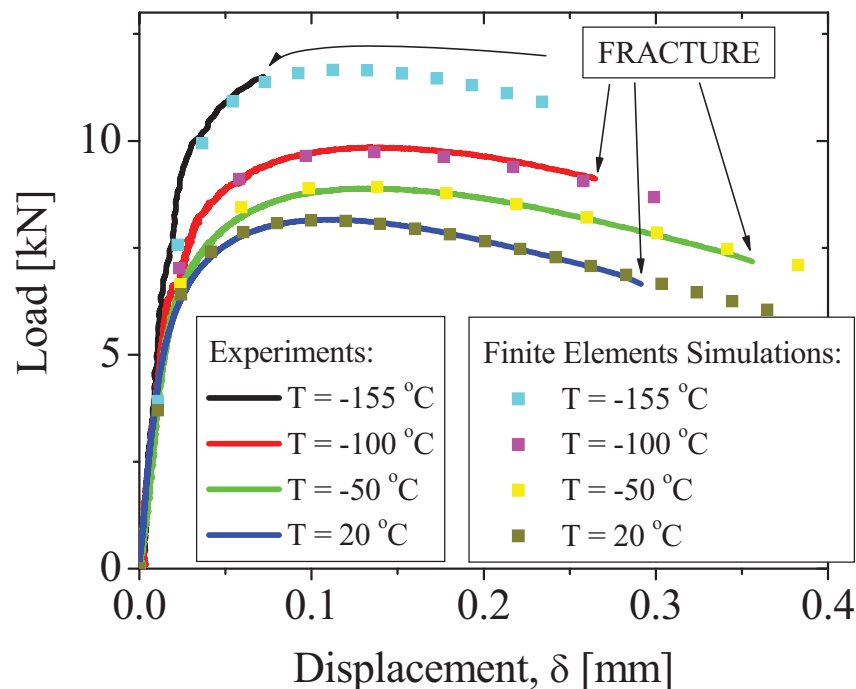

Figure 5-19: Experimental load-displacement curves of the notched tensile specimens at different temperatures along with the simulated curves (see text for δ definition).
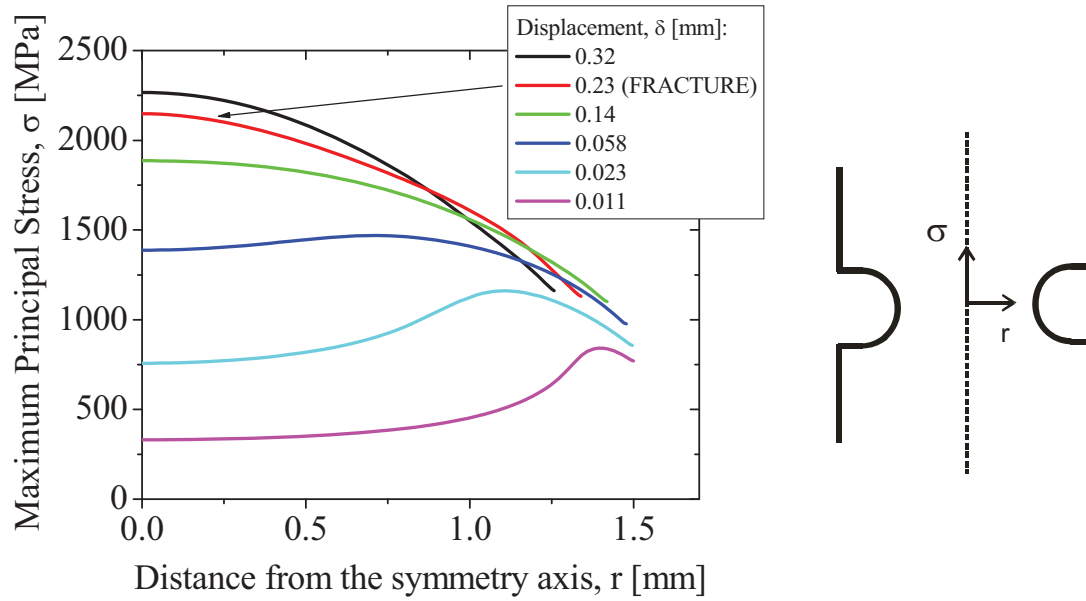
Figure 5-20: Maximum principal stress radial profile on the notch plane for different displacements, δ, at T = -100°C.

5.4.2   The σ^*-V^* model applied to notched tensile specimens

We just recall here that the σ*-V* brittle fracture local approach model which is based on the assumption that brittle fracture will be initiated with a certain probability when V*, defined as the volume of material with maximum principal stress higher than σ*, reaches a critical volume called V^*_c for a given critical stress called σ^*_c. The two material properties of this model are therefore the critical stress σ^*_c and the critical volume V^*_c. We also emphasize that the σ*-V* local approach model has been initially developed for pre-cracked specimens. In pre-cracked compact specimens V^*_c plays an important role because even a very small load produces high stresses close to the crack tip, even higher than the critical stress σ^*_c, but within a volume that is too small to trigger cleavage. However the specimen can only break if the critical stress acts over the critical volume that is for the lower shelf of Eurofer97 of the order of magnitude of 10^{-2} mm^3.

In the case of specimens without a pre-crack such as the notched tensile specimens studied here and the plain tensile specimens studied in next section, the small critical volume is reached practically as soon as the critical stress is reached (see Figure

5-21). This is due to the fact that for the non-pre-cracked specimens, the stress distribution is such that the stress gradient is much weaker than that of the pre-cracked specimen. As an example, in Figure 5-21 we can clearly see that for a notched specimen loaded at -100 ºC even if we multiply the critical volume by a factor of ten the model would predict practically the same breaking point (or equivalently the same displacement δ) for a given critical stress. Thus, the critical stress σ^*_c can be regarded as the governing parameter for these specimens. In other words, any reasonable value of V* would practically not affect the results, even for V* approaching zero ($V^* \to 0$). Note that in C(T) specimens, we showed that the predicted toughness is also weakly dependent on V* if the order of magnitude of V* is kept, but in the case of C(T) if $V^* \to 0$ then the predicted toughness is strongly affected (reduced). This facts may give some physical explanation to the apparently lower scatter of the breaking point observed in notched and normal tensile specimens compared to pre-cracked specimens like the C(T) ones, as discussed in next Chapter.
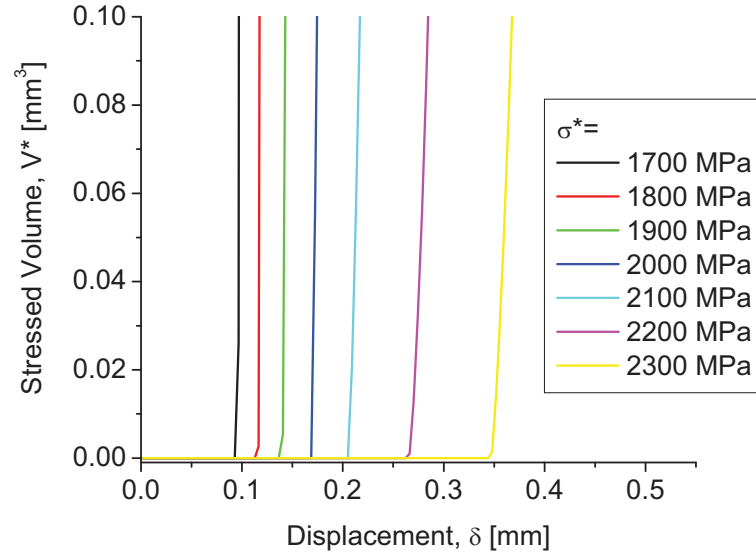
Figure 5-21: Stressed volume as a function of the displacement δ, for different σ* values. The results correspond to a notched specimen at -100 ºC. For notched specimens the critical stress determines the breaking point while the critical volume does not play a significant role.

In Figure 5-22, we show the highest maximum principal stress as a function of the displacement δ, at each tested temperature, along with the points corresponding to the experimental breaking loads. It can be seen that the critical stress σ^*_c= 1955MPa found to reconstruct the lower bound for fracture in pre-cracked C(T) specimens also

represents a lower bound for fracture for the studied notched specimens. The curve
that corresponds to room temperature (20 ºC) does not belong to the brittle fracture
regime and is only shown as complementary information.

Figure 5-22: Notched specimens highest maximum principal stress as a function of the displacement δ,
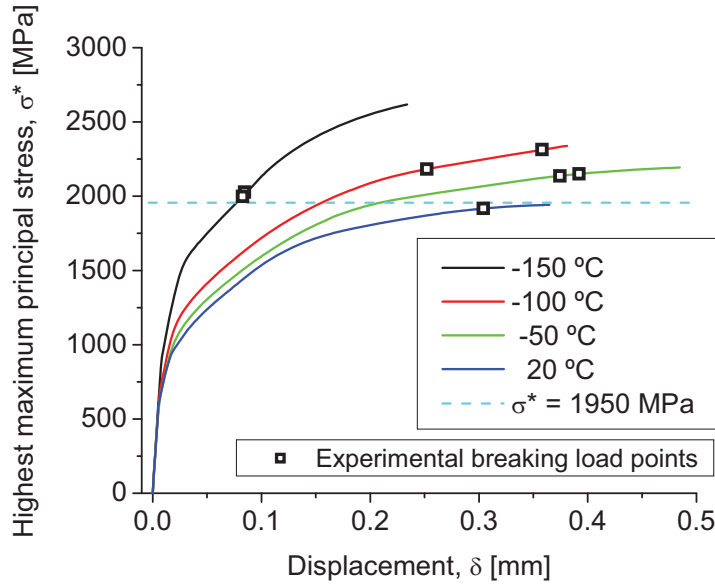for each tested temperature along with the point that corresponds to the experimental breaking load.

In Figure 5-20, the stress distribution at failure is indicated by the red curve where it
can be seen that σ^* is equal to about 2150 MPa. This value was used to predict the
breaking points of notched specimens in the brittle fracture temperature range. The
ability of the calibrated σ^*-V^* criterion to predict the failure load of the notched
specimens over this range of temperature was checked by running the simulations up
to a displacement level at which the mentioned value σ^*_c is attained. At this last
displacement, it was found that both the failure load and failure displacement match
well those of the experimental curve. In Figure 5-23 and Figure 5-24, we plot the
experimental failure load and the experimental failure displacement respectively
along with the calculated load and displacement at which the maximum principal
stress reaches 2150 MPa. Clearly, the calibrated critical stress data predicts quite well
the failure point of notched specimens in the brittle fracture temperature range from
-155 ºC to -50 ºC.

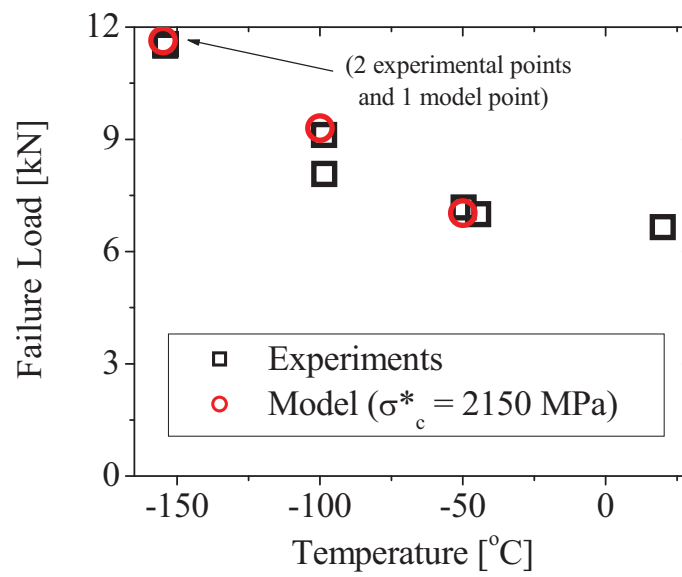**Figure 5-23**: Notched specimens: experimental and calculated failure load with a fracture stress equal to 2150 MPa.
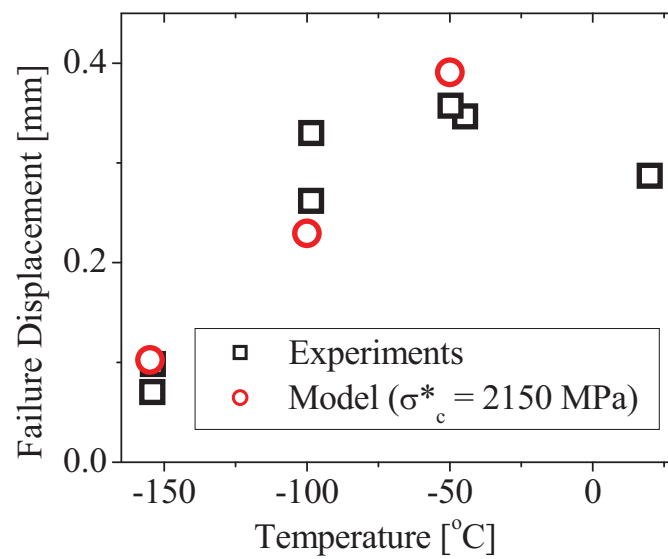

Figure 5-24: Notched specimens: experimental and calculated failure displacement with a fracture stress equal to 2150 MPa.

5.4.3   Conclusions

We showed before that the lower bound of fracture toughness versus temperature, can be reconstructed by calibrating a local criterion of fracture defined by the attainment of a critical value of the maximum principal stress σ^* over a critical volume V^* around the tip of the pre-cracked C(T) specimens. The simulations of the notched specimens indicate that applying the same fracture model with these critical parameters is also consistent with the experimental breaking points of notched specimens. This observation actually constitutes an important experimental verification of the applicability and transferability of such a criterion from laboratory specimens to more complex structural real components.

5.5   Tensile specimens simulations

The aim of this section was to simulate with the finite element method a complete Eurofer97 steel tensile test including the necking phenomenon in order to calculate the stress and strain fields at the onset of brittle fracture and to apply the σ^*-V^* local approach model to the results.

5.5.1   Experimental curves

The tensile tests analyzed in this section were carried out at -60 ºC and -100 ºC. DIN round tensile specimens were used with 3 mm diameter and 18 mm gauge length. The displacement of the specimen was measured by two independent methods: with a clip gage attached to the specimen, and by compliance correcting the displacement of the mobile traverse of the tensile test machine. Excellent agreement between the two methods has been found for strains before reaching maximum load. After maximum load, strain localization takes place in the specimen making the clip gage measurements dependent on the exact initial position of the clip gage and on the

position where necking takes place. Therefore in the following, the presented curves beyond maximum load correspond to the compliance corrected ones.

5.5.2   Simulated load – displacement

The simulations were performed using ABAQUS/Standard™ version 6.7 code. An axis-symmetric model was used. Due to the symmetry conditions of the tensile specimen the mentioned model gives the same results as a 3D model, but at a much lower computational cost. Bilinear quadrilateral elements were used for the mesh that consists of about 52'000 nodes. A non uniform size mesh was used in order to increase the number of elements in the necking region where the highest strain and stress gradients occurs (See Figure 5-25). Mesh and increment size independency of the presented results has been verified by doubling the number of nodes and reducing three times the increment size.
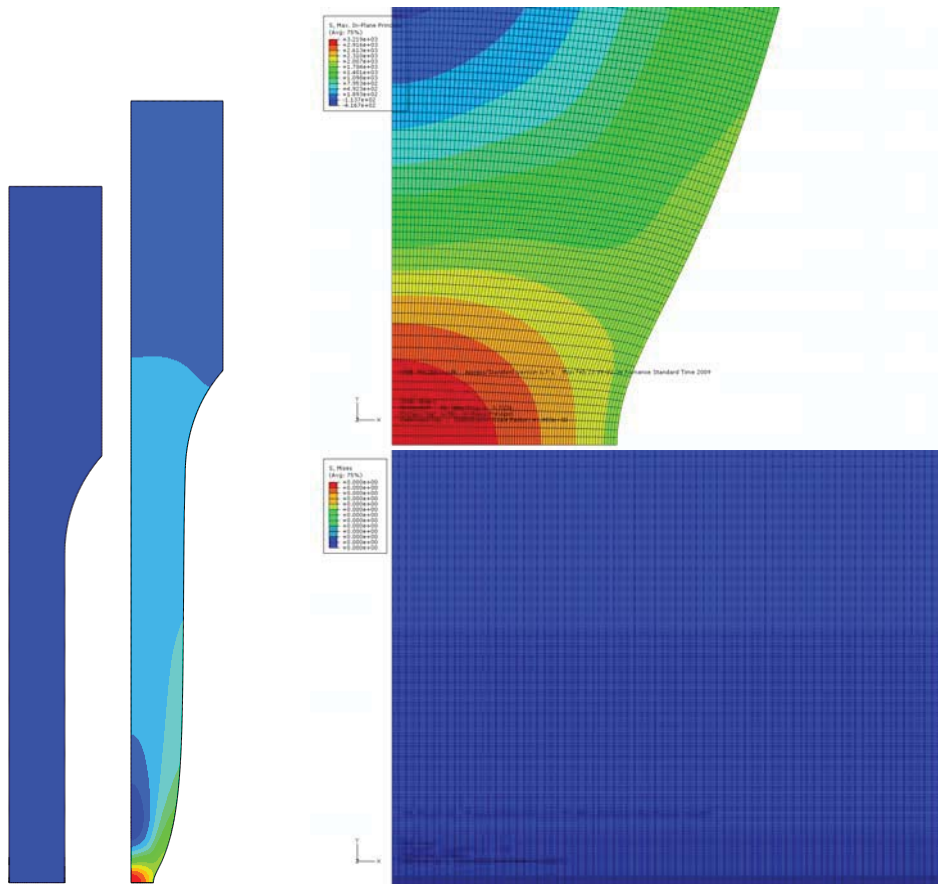

Figure 5-25: In this figure we show an unloaded FE model and a loaded model to 2956 N after necking at -100ºC. A detail of the mesh and the maximum principal stress is shown as well.

Elastic and plastic deformations were modeled. For the simulations the material constitutive properties were considered isotropic. The following elastic properties values were used: Young's modulus E = 212.5 GPa and Poisson's ratio ν = 0.33 at -60 ºC and: E = 214.6 GPa and ν = 0.33 at -100 ºC. The plastic flow properties up to the necking point were represented by the average true stress - true plastic strain curves of the tensile tests performed at the corresponding temperature. The plastic true stress – true plastic strain curve after necking was obtained by linearly extrapolating the flow curve beyond the onset of necking. This procedure was validated in [7, 18], where the load-displacement curves for small ball punch test, notched tensile and compact fracture specimens were successfully reproduced by finite element simulations.

A number of tensile test numerical simulations including the necking phenomenon can be found in the literature for round or flat tensile specimens. Some of these works are reported in [19-22]. An ideal plastic material in which no strain hardening occurs would become unstable in tension and begin to neck just as soon as yielding took place. However, a real metal undergoes strain hardening, which tends to increase the load-carrying capacity of the specimen as deformation increases. This effect is opposed by the gradual decrease in the cross-sectional area of the specimen as it elongates. Necking or localized deformation begins at maximum load, where the increase in stress due to decrease in the cross-sectional area of the specimen becomes greater than the increase in the load-carrying ability of the metal due to strain hardening [23]. After reaching maximum load, uniform strain in the specimen is not stable any more and necking starts in the weakest region of the specimen. Even the most homogeneous material has some degree of inhomogeneity that produces a stress concentration that grows when uniform strain is unstable. In a finite element simulation a small material properties inhomogeneity artificially introduced in the model, a small diameter difference, a small inhomogeneity in the stress fields produced by the specimen holders, or even a small rounding difference in a defect free model can initiate the necking phenomenon when uniform strain is unstable [21]. The strain at which the instability starts in a strain-rate independent material was first theoretically calculated by Considère [24] and is consistent with our results.

In Figure 5-26 and Figure 5-27 we show the experimental and numerical load - displacement curves obtained at -60 ºC and -100 ºC respectively. The load was normalized by the initial cross section area $A_0 = \pi(1.5mm)^2$ and the displacement by the initial length $L_0 = 18mm$. The curves show good agreement between experiments and simulations.

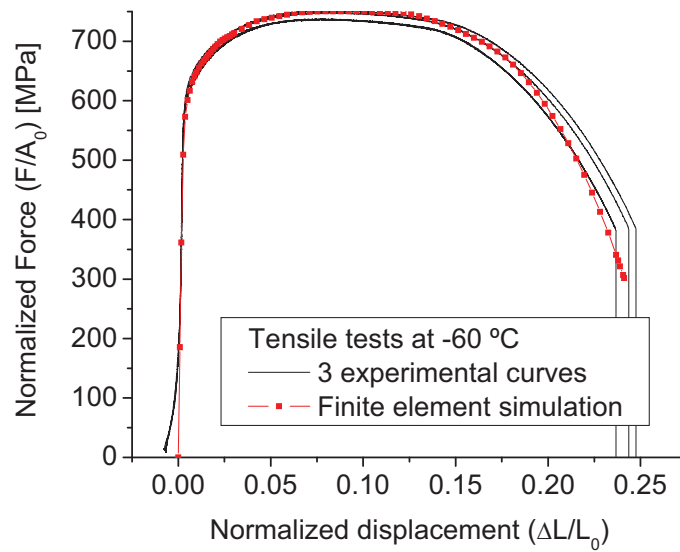**Figure 5-26**: Experimental and numerical load displacement curves at -60 ºC.
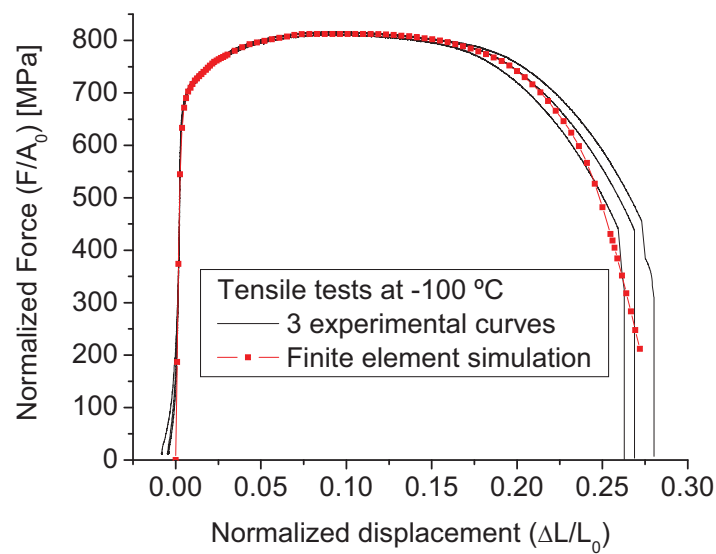
Figure 5-27: Experimental and numerical load displacement curves at -100 ºC.

5.5.3   Necking shape

In Figure 5-28 we show two pictures of a tensile specimen after testing at -60 ºC, along with the finite element simulation maximum principal stress contours and the simulated deformed geometry at the experimental failure load. Again good agreement between simulations and experiments can be seen.
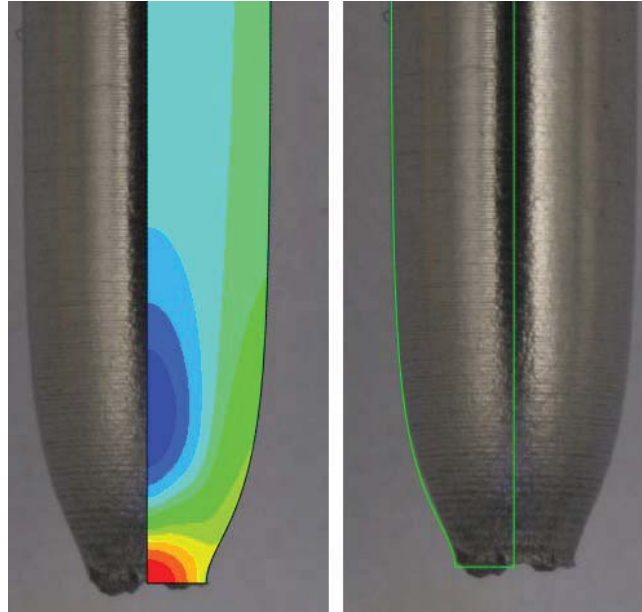
Figure 5-28: Tensile specimen pictures after testing at -60 ºC along with the finite element simulation maximum principal stress contours and the deformed geometry at the experimental failure load.

5.5.4   Fracture model

We have shown in [5] and [7] as well as in sections 5.2   and 5.4   that a critical stress value slightly below σ^*_c=2000 MPa describes the toughness lower bound of Eurofer97 for pre-cracked C(T) specimens and is consistent with the notched tensile specimens results. In Figure 5-29 we show the highest value of maximum principal stress in the specimen (σ^*) as a function of the normalized imposed displacement. The highest value of maximum principal stress is found on the symmetry axis of the tensile specimen at the necking position as seen in red in Figure 5-28. The simulations confirm that also the tensile specimens break with maximum principal stress values above the lower bound values. The critical parameters that describe a lower bound for toughness in pre-cracked C(T) specimens are consistent with the tensile test

simulations, even though they seem to be more conservative in this last case. Note that again, similar to the case of notched specimens explained in last section, the critical volume in tensile specimens practically does not play a role in the predictions. Also in tensile specimens the stressed volume grows very fast once the critical stress is reached, similar to what is shown in Figure 5-21.
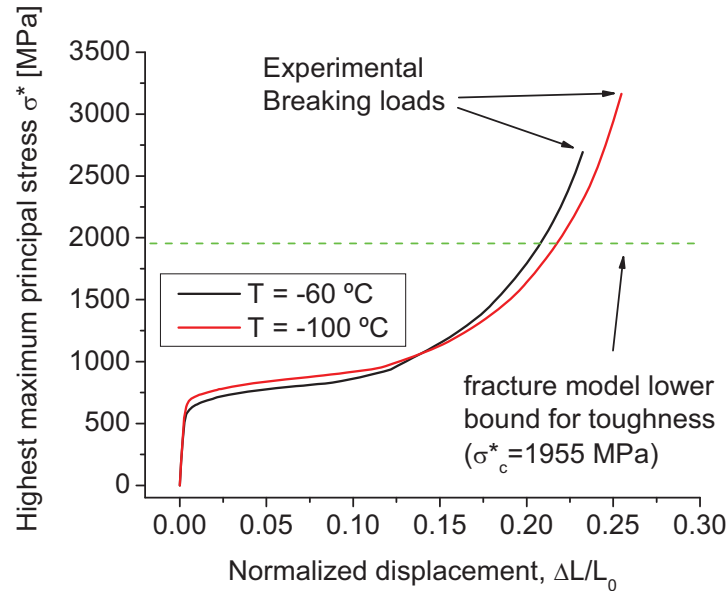
Figure 5-29: Highest value of maximum principal stress in the tensile specimen. The σ*-V* model, calibrated for pre-cracked C(T) specimens (σ*=1955 MPa), predicts that tensile specimens will break above the plotted lower bound for toughness line.

5.5.5   *Conclusions*

In this section we analyzed the round tensile test experiments and finite element simulations including the necking phenomenon at -60ºC and -100ºC performed on the reduced activation tempered martensitic steel Eurofer97. The studied temperatures correspond to the ductile-to-brittle transition range.

 - It was found that the calculated load-displacement curves by finite element simulations reproduce well the experimental curves.
 - The necking phenomenon starts when uniform elongation is not stable any more (Considère's criterion) It was found that necking can be properly reproduced by the simulations even without artificially introducing a small defect.

- In the simulations necking takes place at practically the same displacement as in the experiments.

- The calculated necking shape is very similar to the real one.

- The toughness lower bound predicted by the σ^*-V^* brittle fracture local approach model calibrated for C(T) specimens and compatible with notched specimens, is also compatible with tensile tests. Anyway for tensile specimens the highest critical stress at the breaking point of the measured specimens is higher than for notched specimens.

5.6   References

[1]   Odette GR, He MY. A cleavage Toughness Master Curve Model. Journal of Nuclear Materials. 2000;283-287:120-127.

[2]   Odette GR. On the ductile to brittle transition in martensitic stainless steels - Mechanisms, models and structural implications. Journal of Nuclear Materials. 1994;212-215:45-51.

[3]   Odette GR, Yamamoto T, Rathbun HJ, He MY, Hribernik ML, Rensman JW. Cleavage fracture and irradiation embrittlement of fusion reactor alloys: mechanisms, multiscale models, toughness measurements and implications to structural integrity assessment. Journal of Nuclear Materials. 2003;323:313-340.

[4]   Rathbun HJ, Odette GR, He MY, Yamamoto T. Influence of statistical and constraint loss size effects on cleavage fracture toughness in the transition - A model based analysis. Engineering Fracture Mechanics. 2006;73:2723-2747.

[5]   Bonadé R, Mueller P, Spätig P. Fracture toughness behavior in the ductile–brittle transition region of the tempered martensitic Eurofer97 steel: Experiments and modeling. Engineering Fracture Mechanics. 2008;75:3985–4000.

[6]   Mueller P, Spätig P. 3D Finite element and experimental study of the size requirements for measuring toughness on tempered martensitic steels. Journal of Nuclear Materials. 2009;389:377-384.

[7]   Mueller P, Bonadé R, Spätig P. Fracture properties of notched and pre-cracked specimens of a tempered martensitic steel at low temperature. Materials Science and Engineering A. 2008;483-484:346-349.

[8]   Mueller P, Spätig P. Finite element simulation of tensile tests including necking and a local approach model for fracture. Proceedings of the 2nd South East European Conference on Computational Mechanics. Island of Rhodes, Greece; 2009.

[9]   McMeeking RM. Path Dependence of the J-Integral and the Role of J as a Parameter Characterizing the Near-Tip Field. Flaw Growth and Fracture, ASTM STP 641. 1977:28-41.

[10]   Gao X, Ruggieri C, Dodds RH. Calibration of Weibull stress parameters using fracture toughness data. International Journal of Fracture. 1998;92:175-200.

[11]   Bonadé R. PhD Thesis Number 3405, Constitutive Behavior and Fracture Properties of Tempered Martensitic Steels for Nuclear Applications: Experiments and Modeling. Lausanne, Switzerland: EPFL; 2006.

[12]   Anderson TL. Fracture Mechanics, Fundamentals and Applications, Third Edition. 2005.

[13]   Larsson SG, Carlsson AJ. Influence of non-singular stress terms and specimen geometry on small-scale yielding at crack tips in elastic-plastic materials. J Mech Phys Solids. 1973;21:263-277.

[14]   Sherry AH, France CC, Goldthorpe MR. Compendium of T-stress solutions for two and three dimensional cracked geometries. Fatigue Fract Engng Mater Struct. 1995;18:141-155.

[15]   O'Dowd NP, Shih CF. Family of crack-tip fields characterized by a triaxiality parameter - I. Structure of fields. J Mech Phys Solids. 1991;39:989-1015.

[16]   Ortner S. Factors affecting the shape of the ductile-to-brittle transition. Int J Pressure Vessels and Piping. 2002;79:693-700.

[17]   ASTM. E 1820 - 08. Standard Test Method for Measurement of Fracture Toughness; 2001.

[18]   Campitelli EN, Spätig P, Bonadé R, Hoffelner W, Victoria M. Assessment of the constitutive properties from small ball punch test: experiment and modeling. Journal of Nuclear Materials. 2004;335:366-378.

[19]   Brünig M. Numerical analysis and modeling of large deformation and necking behavior of tensile specimens. Finite Elements in Analysis and Design. 1998;28:303-319.

[20]   Koc P, Stok B. Computer-aided identification of the yield curve of a sheet metal after onset of necking. Computational Materials Science. 2004;31:155-168.

[21]   Joun M, Choi I, Eom J, Lee M. Finite element analysis of tensile testing with emphasis on necking. Computational Materials Science. 2007;41:63-69.

[22]   García-Garino C, Gabaldón F, Goicolea J. Finite element simulation of the simple tension test in metals. Finite Elements in Analysis and Design. 2006;42:1187-1197.

[23]   Dieter GE. Mechanical Metallurgy, Third Edition, SI Metric Edition. 1988.

[24]   Considère M. Annales des Ponts et Chaussées. 1885;9:574-775.

Chapter 6

Discussion

6.1   General comments on the fracture local approaches

In this work, a brittle fracture "local" approach model was applied to reconstruct the toughness-temperature dependence of the lower bound in the ductile-brittle transition region, to quantify the specimen size effect on measured toughness as well as on notched and tensile specimens. The underlying idea of local approach models is to predict brittle fracture initiation from the analysis of the calculated local stress fields generated around a stress concentrator by the external applied loads. On the contrary, classic fracture toughness theories, also referred to as "global" approach hereafter, are based on linear elastic fracture mechanics (LEFM) and elastic-plastic fracture mechanics (EPFM). In LEFM, the elastic stresses in a large specimen have the well known asymptotic solution proportional to $K_I / \sqrt{r}$ close to the crack tip [1, 2]. In EPFM, provided that the analysis is performed for small strains and that the constitutive behavior is modeled by the Ramberg-Osgood relation, the local fields at the crack can be described by the single parameter J_I [3, 4]. However, the descriptions of the asymptotic field based upon a single parameter have their own limitations that call for a more advanced description of the near tip stress fields. Global approaches

incorporating a second parameter, such as the T-stress or Q, were shown to improve the description of the stress field in the plastic zone (finite strains) of real specimens [5, 6]. These global approaches hold as long as specific specimen size requirements are met that, for typical value of the toughness measured in the transition region, require rather large specimens. These requirements ensure that the size of the plastic zone remain small in respect of the other specimen dimensions. However, the fracture specimens typically incorporated into irradiation capsules are usually quite small and practically never meet the size limits imposed by the global approaches. Therefore, the measured toughness of such specimens is significantly dependent on specimen type and size and the near crack tip stress fields generated cannot be uniquely determined by the stress intensity factor. In order to account for these mentioned specimen size effects on measured fracture, local approach development was initiated in the 80s [7]. As mentioned above, the generic idea of the different types of local approaches is to predict the critical condition of fracture based on the actual local stress fields around a stress concentrator calculated in the loaded specimen. Thus, specimen size and specimen type effects are intrinsically included in these local approach models. In addition, they are foreseen to be used to address important issues such as the problem of the "transferability" of results from laboratory scale specimens to structural components.

6.2   The σ*-V* model and its critical parameters

The origin of this local approach model lies in the work of Ritchie, Knott and Rice [8], which is based on the assumption that brittle fracture in a fracture specimen depends on a critical fracture stress σ^* acting over a length λ* ahead of the crack tip. Anderson, Dodds and co-workers [9-12] presented a model to account for the *constraint loss effects* on the fracture toughness values at a given temperature. They proposed a method to *scale* each fracture toughness value as determined from specimens having low constraint level in such a way that the scaled values correspond to those that would have been obtained from testing highly-constrained specimens. The main goal of the scaling toughness model was to deal with the problem of the in-

plane constraint loss, characteristic in the case of shallow cracks or deep cracks loaded up to large strains. The approach was further used in 3D numerical studies [13] were the concept of an "effective thickness" B_{eff} was introduced. Explicit corrections to account for the out-of plane loss of constraint were proposed in their work.

Odette and coworkers have extended the scale toughness model beyond its original scope of scaling low constraint toughness data at a constant temperature [14-16]. They developed the so-called "critical stress-critical area" model, $\sigma^* - A^*$, which was aimed at describing the evolution of fracture toughness with temperature in the ductile-brittle transition region. The $\sigma^* - A^*$ model (and its extensions) are based on the two following hypotheses:

a) brittle fracture is triggered when a critical area A^* (or volume V^*) of material encompasses a critical stress level σ^*.

b) the critical values σ^* and A^* (or V^*) are usually assumed to be material properties independent of the temperature. However, a modest temperature dependence of σ^* was considered and discussed in [14].

The critical stress σ^*_c

We discuss here the value of the critical stress that we calibrated in previous Chapter. Cleavage in "ferritic" steel is usually considered to be initiated at cracked carbides [17], or more generally at broken particles, and macro-fracture is considered to occur when a critical local tensile stress σ^*_c is reached to propagate the resulting micro-crack. The value of σ^*_c can be interpreted in terms of the modified Griffith's criterion [18], which for a penny-shape crack of critical radius r_c, is given by:

$$\sigma_c^* = \left(\frac{\pi E (\gamma_s + w_p)}{2(1-v^2)r_c} \right)^{1/2} \qquad (6.1)$$

where E is the Young's modulus of the ferrite, v is the Poisson's coefficient, γ_s is the surface energy of the ferrite and w_p is half the plastic work done per unit of area in propagating the crack. The term $(\gamma_s + w_p)$ is the effective surface energy. In practice however, micro-cracks initiated at a broken particle can propagate into the ferritic matrix where they can arrest so that the real size of the micro-cracks to consider is not the radius of the particle itself but rather an effective length, l_{eff}, larger than the particle radius [19]. In this case, Eq. (6.1) can be rewritten as:

$$\sigma_c^* = K_{local}\sqrt{\frac{\pi}{2l_{eff}}} \qquad \text{with} \qquad \mathrm{K}_{local} = \left(\frac{E(\gamma_s + w_p)}{(1-v^2)}\right)^{1/2} \qquad (6.2)$$

This view of fracture actually implies that the critical step in cleavage is the propagation of the micro-crack into the ferrite matrix and not the initiation. This interpretation has been invoked by several authors, e.g. [18, 20], and will be used in the following as a basis to discuss the value of the critical stress.

An estimate of σ^*_c is done using Eq. (6.1) and considering published values of γ_s and w_p. Values of the effective surface energy $(\gamma_s + w_p)$ has been reported to be between 5-14 Jm^{-2} [20] for low-alloyed steels. Taking the surface energy of iron as reference, determined from experiments by Price et al [21] and simulation using the Finnis-Sinclair potential, γ_s is around 2 Jm^{-2} [22]. These values of $(w_p + \gamma_s)$ and of (γ_s) indicate that the larger part can be attributed to the plastic work w_p. In Figure 6-1, we plot the micro-crack length dependence of σ^*_c calculated with Eq. (6.1) for three different values of $(\gamma_s + w_p)$: 7, 10, 14 Jm^{-2}. The three curves indicate that the micro-crack length must be of the order of 0.5 μm to 2 μm to be consistent with the critical stress (of nominal value 2000 MPa) required to reconstruct the toughness-temperature master-curve. In the Figure this is indicated by the green rectangle.
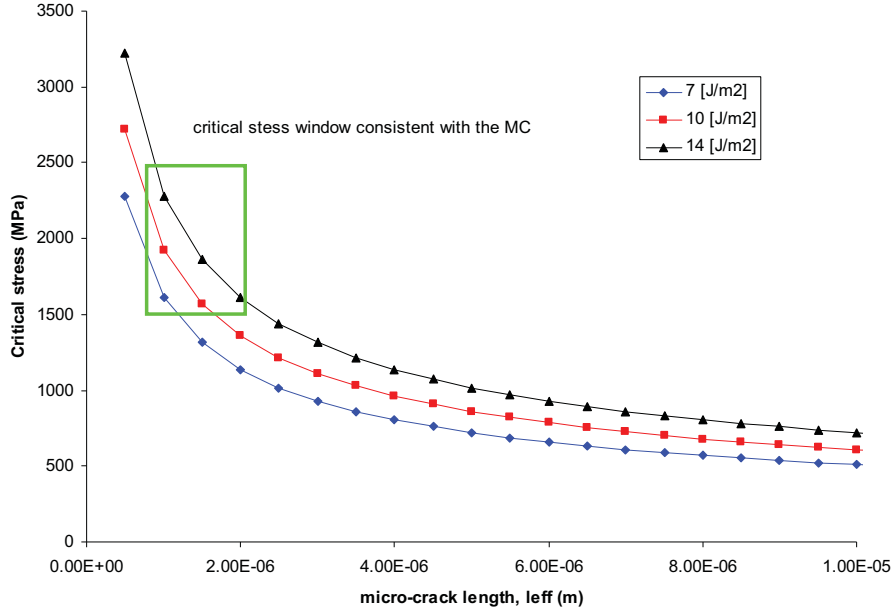
Figure 6-1: σ^*_c calculated for different values of effective surface energy as a function of the micro-crack length.

As shown in Chapter 3, we recall here that in the studied tempered martensitic steels the carbides are quite small, below 1 μm. In addition, we showed that the tempered martensitic microstructure consists of small sub-grains, often elongated, of the order of 1 μm. Thus, one can reasonably assume that the critical micro-cracks length, emanating from such small carbide, are in the range of few tenths to few microns, i.e, long enough to propagate within the sub-grain they propagate into.

Attention has to be given to one of the main assumptions of the σ^*-V^* model: the temperature independence of σ^*_c. This assumption is supported by a great deal of studies showing that the local cleavage fracture stress is essentially temperature independent [18, 23-25]. A sound physical explanation of this observation is not straightforward and remains an issue far from being fully resolved. However, looking at Eq. (6.1), the following comments can be made. The temperature independence of σ^*_c implies that the right side of Eq. (6.1) is independent of temperature. γ_s can be regarded in good approximation as temperature independent. As a matter of fact, γ_s presents the same temperature dependence as that of the Young's modulus, which for Eurofer97 varies less than 10% from room temperature down to -200 ºC. The plastic work w_p represents the work done to emit and move dislocations, which always occurs even at the lowest temperature investigated. As a rule, dislocation nucleation

and propagation increase with temperature and consequently the plastic strain level in the vicinity of the micro-crack. However, as temperature increases, the flow stress, which is thermally activated, decreases. At temperatures in the transition region, the plastic flow properties strongly depend on temperature. The yield stress for instance varies from around 550 MPa at room temperature to around 1100 MPa at liquid nitrogen temperature. In this temperature range, the dislocation mobility is highly thermally activated and controlled by the nucleation of double kinks below about -100 °C [26]. Thus, the temperature dependence of w_p may remain quite weak owing to the trade-off between the increase of equivalent plastic strain and decrease of plastic flow stress as the temperature increase. In addition, any temperature variation in the effective surface energy is smoothed by the square root in Eq. (6.1). Nowadays, no model and/or theory has been formulated to explain the constancy of w_p.

As a final comment for this sub-section, we note that, as mentioned by Croates et al. [27], the exact interpretation of the critical fracture stress is not universally admitted to be the modified Griffith energy balance. Indeed, it can also be considered as: i) the stress to nucleate a micro-crack from a grain-boundary carbide, ii) the stress to propagate this crack through the adjacent grain, iii) the stress to propagate the micro-crack through the next grain-boundary carbide or iv) the stress to propagate the crack to the next adjacent grain. Nonetheless, using Griffith's equation and a reasonable value of the modified surface energy, it was possible to derive consistent σ^*_c values with those used to reconstruct the master-curve.

The critical volume V^*_c

Another assumption of the model is related to the attainment of a critical volume V^*_c, encompassing σ^*_c, to trigger macro-failure. This volume is the natural consequence of the fact that the occurrence of a single micro-crack is not sufficient to initiate a macro-crack but that macro-failure results from the coalescence of a collection of micro-cracks in the process zone. This is supported by experimental evidence presented by Edsinger [28] and Odette et al. [29, 30] who have shown, using a special fracture reconstruction technique, that material separation take place in the so-called process zone ahead of the crack tip. This technique allows visualization of the areas of

the crack plane where plastic deformation occurred as a function of the crack tip opening displacement. Quasi-cleavage in tempered martensitic steels is seen as the growing of a process zone, in which many micro-cracks are created upon loading. Ultimately the process zone reaches an instability point where sufficient micro-cracks coalesce into a single unstable macro-crack leading to macroscopic fracture. Hence, V^*_c, is related to the critical size of this process zone and we emphasize that a local fracture criterion based only on a critical stress cannot be realistic and that the attainment of critical volume is needed. If the local fracture model relied only on a single parameter, such as a critical stress, fracture would occur at very low load, at least in pre-cracked specimens where even a very small load is enough to create a small region of high stress close to the crack tip. The structure and evolution of the stress field with increasing K is illustrated in Figure 6-2. Ahead of the crack tip, the stress field peaks at a certain value, which is independent of the applied K, but the width of peak increases with K. Hence, the effect of the increasing loading is essentially to broaden the peak.
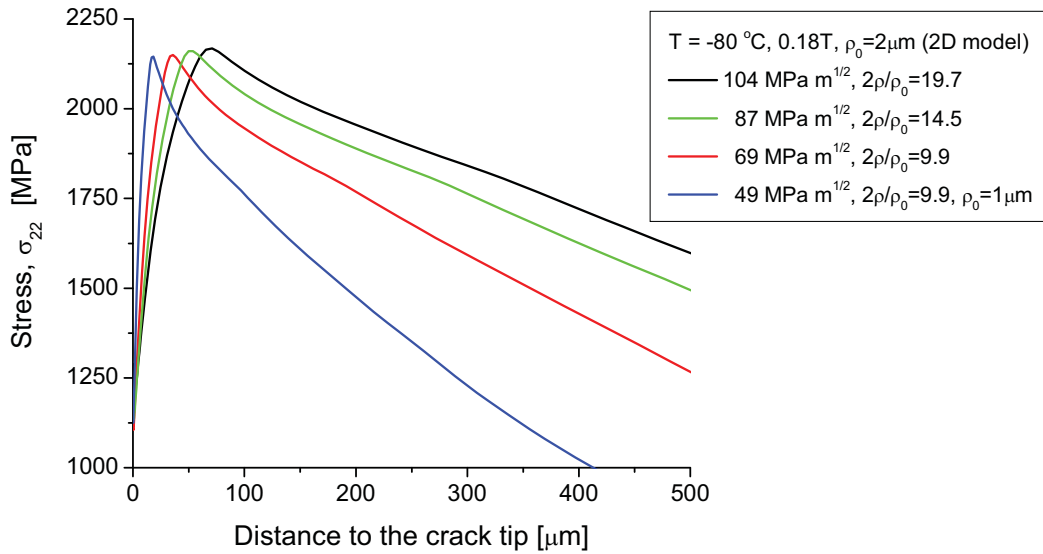
Figure 6-2: Evolution of the stress field in the finite strain region with increasing applied stress intensity factor in a C(T) specimen. Note that ρ_0 is the initial crack tip radius and ρ is half the crack tip opening displacement.

We also recall the effect of the values of σ^*_c and of V^*_c on the toughness temperature curve, K(T). Increasing σ^*_c makes the K(T) curve steeper while increasing V^*_c shift

the whole curve up (see Figure 5-9). Therefore, the shape of the K(T) curve is very well mediated by σ^*_c because small variation of σ^*_c, typically 100 MPa over 2000 MPa, results in well identifiable K(T) curvature change. Further in this, we showed that various pairs of critical values, σ^*_c and of V^*_c, can be chosen to reconstruct an experimental K(T) curve with practically the same quality. For the lower bound curve of Eurofer97, the average values were: $\overline{\sigma}^*_c = 1955$ MPa and $\overline{A}^*_c = 1100$ μm^2, and the corresponding uncertainties were: $\Delta\sigma^*_c = 15$ MPa and of $\Delta A^*_c = 300$ μm^2. The rather large uncertainty in the critical volume stems from the very strong dependence of the critical area on the applied toughness, $A^* = c \cdot K^m_J$, with m about 4.

The ability of the model to reproduce the correct temperature dependence of the measured toughness in the ductile-brittle transition region with temperature independent critical parameters may appear at first glance contradictory. However, this can be readily understood from the temperature dependence of the stress fields that appear in the process zone ahead of the crack tip of the loaded specimens. Indeed, the maximum of the peak stress in the process zone is actually temperature dependent, owing to the strong temperature dependence of the flow stress in that temperature domain. Actually, the lower the temperature is, the higher and wider the peak stress is and consequently the higher the critical volume for a given applied K. This is shown in Figure 6-3 and explains the fact that at higher temperature a higher applied stress intensity factor K is needed to initiate brittle fracture. A higher K broadens the stress peak enough so that the critical volume is reached and the specimen breaks by cleavage. Ultimately, by increasing the temperature sufficiently (or equivalently by decreasing the flow stress), the peak stress ahead of the crack tip will not reach the critical stress and the crack will then grow in stable manner and ductile fracture mechanisms start to dominate.
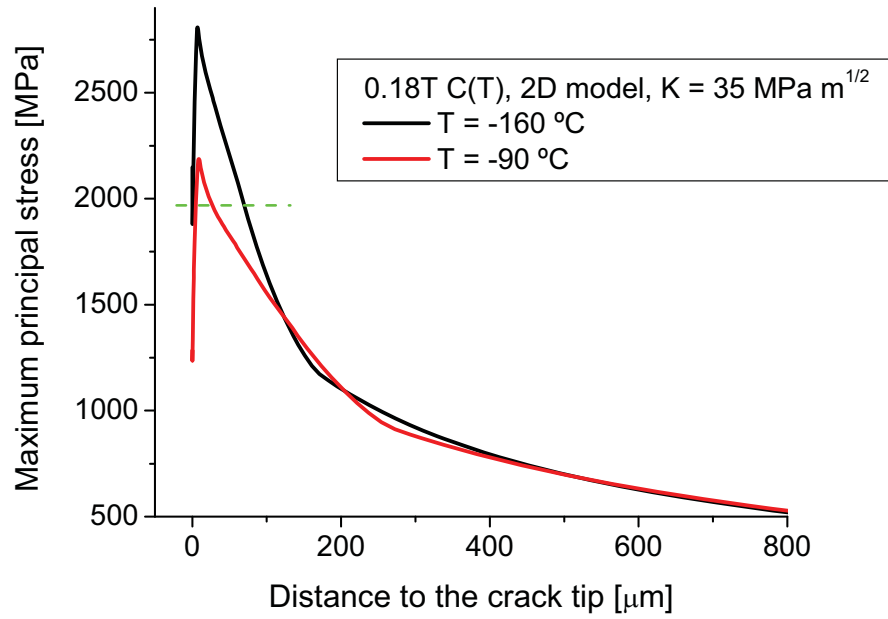
Figure 6-3: Stress field ahead of the crack tip of a C(T) specimen for a stress intensity factor K = 35 MPa m$^{1/2}$. Clearly at low temperature a higher and wider stress peak appears.

Finally, from the 3D simulations performed at -60 °C, it is possible to validate the results of the 2D we used to reconstruct the lower bound. First, we note that at -60 °C, the toughness on the lower bound is about 60 MPa m$^{1/2}$. For the validation, we basically need to check that the product of the critical area determined in 2D specimens at 1950 MPa and of the crack front length B is equal, or very close, to the critical volume calculated for the same specimen size in 3D. In 2D, we have determined a nominal critical area of 1100 μm^2, which yields a critical volume of 0.0242 mm^3 for the 0.87T C(T) (B=22 mm). On the other hand, from the 3D simulations at -60 °C, we can calculate the critical volume with the relation given in Table 5.6 for a critical stress of 1955 MPa and in the range of 60 < K < 158 MPa m$^{1/2}$. In 3D, we obtained 0.024 mm^3, which is practically identical to that derived from the 2D. Note that the stress fields close to the crack tip calculated with 2D simulations are consistent with the 3D ones only for low applied loads or deformations like the ones corresponding to the toughness lower bound.

6.3   Effectiveness, advantage and limitations of σ*-V* model

The effectiveness of the model was first demonstrated by predicting with temperature independent critical parameters, the temperature dependence of the 1% fracture toughness lower bound of Eurofer97 pre-cracked C(T) specimens in the temperature range from -196 ºC to -40 ºC. Second, the failure load temperature dependence of the notched specimens was also well described by the σ*-V* model in a similar temperature range. Third, simulations of standard tensile tests up to failure provided useful information. We recall that the calibrated critical stress of 1955 MPa bounds all experimental failure points of the three studied geometries. While C(T) specimens and notched specimens present failure points not far above 1955 MPa, in the tensile tests, it was found that the critical stress increase up to 2690 MPa and 3160 MPa at failure load at -60 °C and -100 °C respectively. Note that for notched specimens the median breaking temperature dependence was properly predicted by a critical stress of 2150 MPa. Thus, it clearly appears that the critical stress is not fully independent of the geometry of the stress concentrator, which in our case was: either a sharp pre-crack, or machined notch, or the neck of a tensile specimen. This reflects the fact that the overall stress state is also a factor controlling the value of critical stress. In particular, it is well known that among the various factors that promote cleavage the level of stress triaxiality plays an important role. While not quantified in this work, a higher triaxiality level is expected in the process zone of the pre-cracked C(T) specimens and notched specimens, owing to the stronger plastic strain gradient at the crack tip or notch, than in that of the neck of the tensile specimens. Thus, the critical stress determined for the toughness-temperature dependence of pre-cracked specimens on the lower bound can be regarded as the minimum value of σ* that must be reached in other specimen geometries and, as such can be used as a conservative value.

The main advantage of the σ*-V* model resides in the simplicity of the calibration procedure to extract the two critical values: σ^*_c and V^*_c. Once the shape of the K(T) curve is given, or equivalently any particular failure bound of the master-curve is known, one can derive σ^*_c and V^*_c according to the procedure describe in Chapter 5. As shown in Chapter 4, moderate deviations in the shape of the master-curve can be expected. We do believe that such deviations are not specific to the tempered

martensitic steels but stem from differences in the microstructure and constitutive behaviors between different ferritic steels. So, before calibrating the critical parameters, it is of primary importance to check and/or adjust the shape the master-curve. From the point of view of the experimental testing, one has to perform a series of tests at different temperatures such that a high level of constraint is maintained in the fracture specimens; in other words, one should ensure that the M values associated to the toughness data remain above at least 100. Typically, testing a total of six sub-sized specimens at four different temperatures to have enough statistics is sufficient to do an adjustment of the shape of the K(T).

In this simple form of the σ^*-V* model, statistical effects are not explicitly taken into account. However, in addition to its capability to predict the toughness temperature dependence, it is extremely useful to account for the constraint loss effects and to scale toughness data between two different specimen sizes. Statistical effects can in principle be included in further developments the model. One possible staring point to do so, is the approach proposed by Wallin [31, 32]. In their model, they calculated the statistical effects in toughness results based on the probability of encountering a particle having a radius satisfying the modified Griffith's criterion within the plastic zone around the crack tip. Thus, a direct link between the calculated stress, the particle size and the particle size distribution and density was established. Another local approach is that based upon the work of Beremin who [33] also developed a local model to deal with the statistical effects, based on the probability of finding a critical micro-crack in the plastic zone. In Beremin's model the cumulative failure probability is expressed with a two parameter Weibull distribution, the variable being the so-called Weibull stress that depends on the applied stress intensity factor. Gao *et al*. [34] proposed a sophisticated calibration procedure to determine the two parameters in Beremin's equation, which requires the use of fracture data obtained with high and low constraint specimen configurations as well as detailed 3D finite element simulations (such experimental data are not available in this work).

In spite of the fact that the σ^*-V* model is deterministic, some comments about the scatter of our data can be done within the framework of this model. For instance, if we compare the scatter in fracture toughness of the Eurofer97 C(T) specimens tested at -

60 ºC with the tensile specimens tested at the same temperature or with the notched specimens tested at -50 ºC, it is clear that the scatter in C(T) specimens is greater. The relative difference in the maximum and minimum breaking load, or K_J measured in C(T) specimens is much greater than the relative difference in breaking load of the non-pre-cracked specimens. This is reflected by the σ*-V* model by the different sensitivity in the predicted breaking point with the critical volume. In Figure 5-17, we can see that if the critical volume in C(T) specimens increases by a factor 10 then the predicted K_J increases up to 2 times, but for non-pre-cracked specimen the same variation in critical volume practically does not change the predicted breaking load as reflected in Figure 5-21. This difference in behavior results from the difference between the stress gradient that exists ahead of a crack tip and the one at vicinity of the notch. In the case of the notch, the critical stress alone controls the failure point, i.e., as soon the critical stress is reached, a volume large enough is encompassed by that critical stress to lead to failure. On the contrary, for the C(T) specimens, even if the critical stress is reached close to the peak stress at low load, the stressed volume is not sufficient to trigger failure and the load has to be increased until the critical volume is attained.

As presented in Chapter 2, neutron irradiation creates defects in the steel matrix such as interstitials and vacancies clusters and gaseous impuritites, which accumulates with neutron fluence. Below about 450 °C in steels, these defects act as additional obstacles against dislocation glide, which are finally responsible for irradiation hardening. This increase of the flow stress in steels produce higher stress fields in the fracture process zone than those in the unirradiated materials tested at the same temperature. Irradiation embrittlement or equivalently decrease of the fracture toughness result from irradiation hardening. For this kind of embrittlement, it is very likely that the σ*-V* model could predict the decrease of toughness after irradiation with the same critical parameters calibrated for the unirradiated steel. In this case, the increase of the flow curve controls the stress fields at the crack tip but the micro-mechanisms of micro-crack initiation and propagation are assumed not to be affected by the very fine irradiation-induced damages. It has to be emphasized that depending on the irradiation conditions there are other embrittlement mechanisms called non-hardening embrittlement, such as helium embrittlement resulting from the helium

accumulation at the grain boundaries that can lead to intergranular cleavage. In such a case, the micro-mechanisms of fracture change from transgranular cleavage in the unirradiated material to a combination of transgranular and intergranular cleavage after irradiation.

This model takes advantage of the today's availability of powerful computers and advanced finite element simulation codes which allow calculating accurately the stress fields generated in the finite strain region of real specimens as a contrast of using approximate solutions mainly derived from elastic and elastic-plastic theories. However, the stress and strain fields calculated by finite element on the basis of the continuum approach code and rely on the J2-plastic theory where the effects of different crystallographic orientations of the grains that form the steel are not considered. The calculated fields have to be regarded as represented an average of the stress over a number of grains that are randomly oriented. The actual local crystallographic orientation and configuration of the grains inside the process zone at the crack tip is likely to play a role in the measured toughness scatter.

6.4 Relation between M and the critical parameters of the σ*-V* model

In Chapter 4, we studied the reference temperature T_o dependence on the M limit factor. For the sake of clarity, we just recall here the definition of the M limit factor.

$$K_{Jc\_limit} = \sqrt{\frac{Eb_0\sigma_{ys}}{M(1-v^2)}} \tag{6.3}$$

M is the dimensionless quantity that sets the specimen measuring capacity, or in other words, the maximum toughness that can be measured with a certain specimen size having a given yield stress. The specimen size is only characterized by the uncracked ligament length b_o, and the yield stress represents the material properties. Provided that an M value greater than 100-150 is considered, we showed that T_o determined according to the ASTM-E1921 standard remains specimen size independent. Such a

large M value is well above 30 as recommended in the standard. We also remind that, for Eurofer97, T_o was about -78 °C.

The 3D-simulations we performed at -60 °C to quantify the specimen size effect can be also analyzed in order to assess the M factor. This was readily done by reprocessing the data presented in Figure 5-17. In that Figure, the evolution of the calculated volumes V*, encompassing the maximum principal stress 1955 MPa for two specimen sizes 0.35T C(T) and 0.87T C(T), is plotted along with the small-scale yielding V*(K) curves (SSY curve). The SSY curve has the form V*=cK^4. For this discussion, we selected σ*=1955 MPa because this stress is the calibrated one for the 1% lower bound. In Figure 6-4 and Figure 6-5 below, V* is plotted against the M parameter deduced from Eq. (6.3). For low deformation, i.e., large M value, the calculated volume of the real specimen converges to that the SSY solution; this occurs for M value greater than 200. We note that the convergence seems to be slower for the 0.35T C(T) specimen than for the 0.87T C(T). This fact is likely to result from out-of-plane constraint loss effects that are not explicitly taken into account in the M factor; indeed only the uncracked ligament length appears in the M definition. This is an indication that the specimen thickness, or the crack front length, should meet a minimum explicitly size requirement, which for the time being remains to be determined.
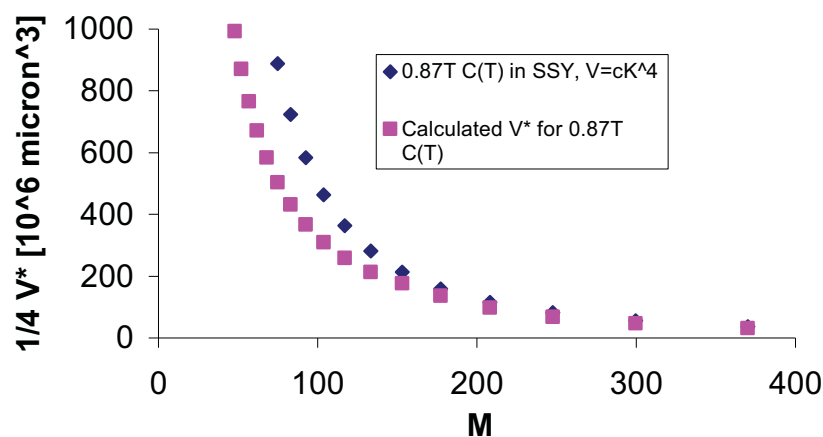

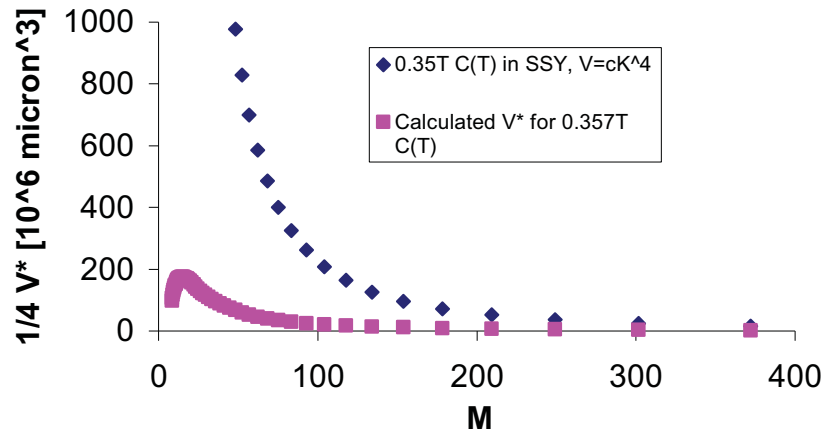**Figure 6-4**: V* encompassing σ*=1955 MPa versus M, for the 0.87T C(T) specimen and ideal SSY case.

Figure 6-5: V* encompassing σ*=1955 MPa versus M, for the 0.35T C(T) specimen and ideal SSY case.

More enlightening than plotting V* as a function of M is the evolution of the difference ΔK between K measured on a real specimen and K_{SSY} that would be obtained from a specimen in SSY condition. This is represented in Figure 6-6 and Figure 6-7, for the 0.87T C(T) and 0.35T C(T) specimens respectively. One can see that for small deformation corresponding to M values larger than 200, ΔK is constant. However, at a critical increasing deformation represented by M of about 150 (M decreasing), the increase of ΔK becomes very abrupt, clearly indicating a strong specimen size effect. This value is in full agreement with that obtained in Chapter 4 from the analysis of the entire fracture toughness database. It is indeed remarkable that it is actually possible to extract a reasonable M value from the finite element simulations based upon the calibrated σ*. Finally, we mention that an increase of 10% in measured toughness due to specimen size effects corresponds to a M value of about 80. Therefore, such a M value can be regarded as large enough for a reliable determination of T_o, since it would result in an error of less than 10 °C of T_o for specimens tested at temperatures close to T_o.
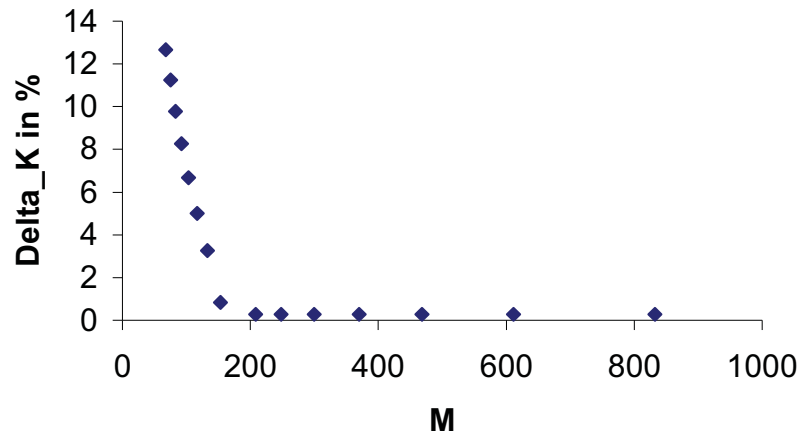
Figure 6-6: $\Delta K=100*(K_{0.87T\ C(T)} - K_{SSY})/K_{SSY}$ versus M for the 0.87T C(T) specimen size.
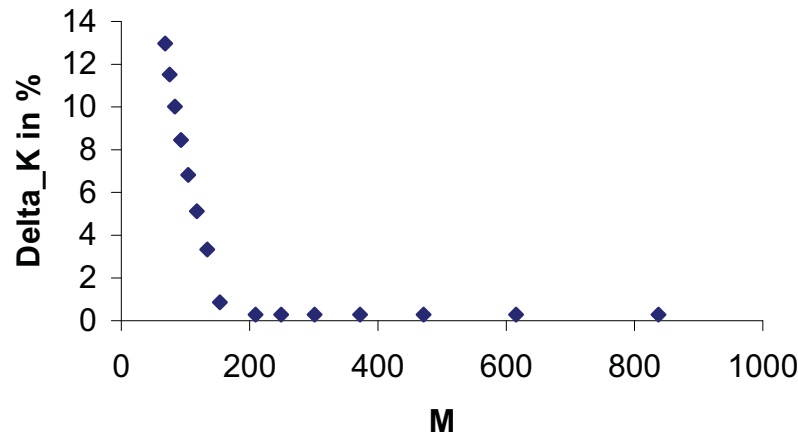
Figure 6-7: $\Delta K=100*(K_{0.35T\ C(T)} - K_{SSY})/K_{SSY}$ versus M for the 03.35T C(T) specimen size.

6.5   Difference in the fracture properties between F82H-mod and Eurofer97 in relation to their microstructures.

In this Section, we highlight and discuss the differences in the toughness properties in the transition region between Eurofer97 and F82H-mod steels. Since different heats and plates of these steels were produced, we restrict the comparison to the 25 mm thick plates for which large fracture specimens could be used to index the reference temperature T_o of the master-curves. For Eurofer97 and F82H-mod, the heat numbers of these thick plates were respectively E83697 and 9753. In total only a limited

number of tests with 1T C(T) specimens of F82H-mod were performed by Wallin [35] as well as by Sokolov *et al*. [36]. As far as Eurfoer97 is concerned, the biggest specimens tested are the 0.87T C(T) presented in this study.

First, we assembled the F82H-mod data of Wallin and Sokolov *et al*. and performed a T_o determination according to the ASTM-E1921 standard, similarly to what these authors did in their own investigation. In Figure 6-8, we plot the data with the master-curve that was indexed at T_o = -99 °C with the corresponding 1% and 99% tolerance bounds. We precise here that T_o was obtained by considering M = 30 as recommended in the standard. There are a total of 43 data points in this plot for which 5 fall out of the 1% and 99% tolerance bounds, which is of course significantly more than expected since all the data should in principle lies between the two bounds. This observed excessive scatter has initiated some debate within the fusion material community regarding the applicability of the master-curve concept to the high-alloy tempered martensitic steels [37]. The other relevant observation is that the data points falling out the tolerance bounds are only those obtained by Sokolov *et al*.
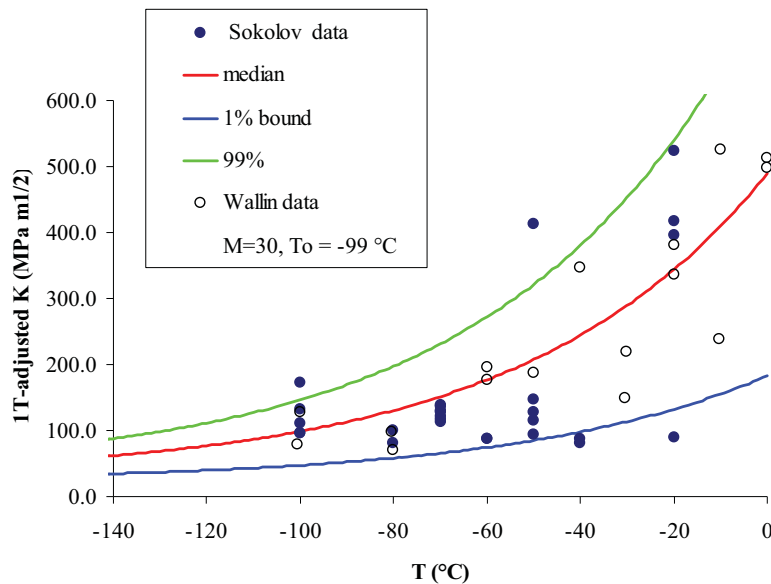

Figure 6-8: F82H-mod C(T) fracture toughness data.

On the contrary, the statistical distribution of Eurofer97 data we determined in Chapter 4 was shown in full agreement with the probabilistic predictions of the master curve, provided that a shape adjustment on the lower part of the transition was done.

In particular, not a single point was found between the 1% tolerance bound for a database containing 70 fully constrained data points. On the one hand, regarding T_o as an indicator of brittleness, Eurofer97 with T_o at -78 °C appears clearly more brittle than F82H-mod with T_o at -99 °C. On the other hand, the underlying idea of the master-curve method is to define a lower tolerance bound for integrity assessment. Interestingly, when plotting the F82H-mod and Eurofer97 data together with the 1% bound of Eurofer97 (Figure 6-9), one observes that, even though the reference temperature of Eurofer97 is about 20 °C higher than that of F82H-mod, the Eurofer97 lower bound does not represent a conservative bound for F82H-mod, as we can still find F82H-mod data below it. In that sense, Eurofer97 does not necessarily appear more brittle than F82H-mod.
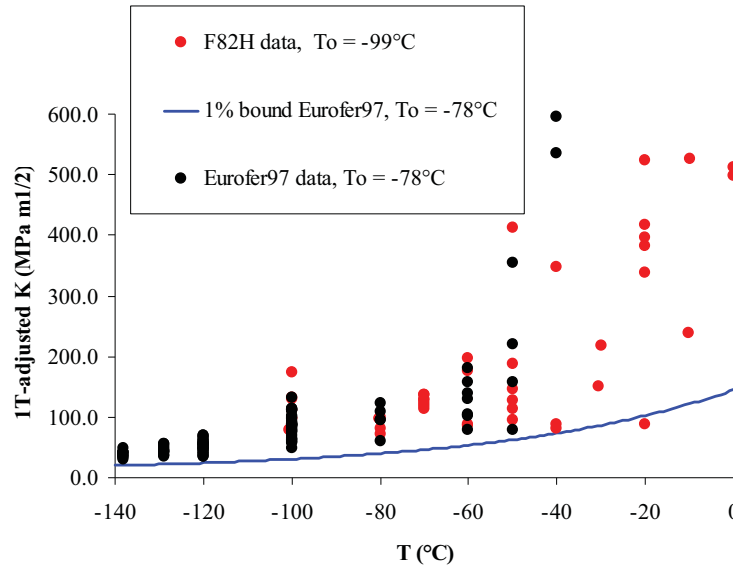
Figure 6-9: Eurofer97 and F82H-mod C(T) fracture toughness data along with Eurofer97 lower bound.

Further in this, from an engineering point of view, a deterministic analysis and assessment of structure integrity, based on the master-curve method, relies on a conservative reference temperature, defined as RT_o, and on the selection of a lower tolerance bound. RT_o is then defined as [38]:

$$RT_0 = T_0 + \Delta \tag{6.4}$$

Indexing the master curve with RT_o instead of T_o produces a safety margin, by shifting the associated lower bound to higher temperature. Δ has to be such that all the

available data are above the selected lower bound. RT_o is based on a simple addition of 19.4 °C to the value of T_o obtained from ASTM E 1921 [39]. RT_o reference transition temperature can then be used to index the ASME code reference K_{Ic} curve, which has to be conservative relative to the actual fracture toughness data. An additional safety margin taking into account for example the material inhomogeneity and the uncertainty in the measurement of T_o may in principle be added to RT_o. One manifestation of material inhomogeneity through a large plate can be variation in T_o as a function of the location in the plate, whose consequences are to increase the scatter in the transition.

Sokolov and Tanigawa proposed to improve the description of the F82H-mod scatter with two more sophisticated methods than the standard master-curve [36]. First they looked at the bimodal master-curve approach for the F82H-mod and showed that the description of the scatter of the data in the transition region slightly improve the description of the scatter. However, the bimodal master-curve suffers from a lack of a sound physical basis. It was indeed initially proposed by Wallin *et al.* [40] to characterize the fracture toughness data distribution measured in the heat-affected zone of welds. In such a case, one could reasonably expect to obtain toughness data representing base metal and others representing the heat-affect zone. However, there is a priori no physical basis to invoke the bi-modal approach to describe the toughness data and associated scatter of the F82H-mod in the transition region. Sokolov and Tanigawa also analyzed their data with the random inhomogeneity technique, which associates a specific T_o value for each specimen. With this method, the scatter in toughness in the transition was significantly improved. However, a major drawback of the method is that it requires the use of at least 20 specimens. This may be a limiting factor regarding the applicability of this method for irradiated specimens whose numbers is usually quite limited. It is also worth emphasizing the fact that the reference temperatures obtained by Sokolov and Tanigawa by the standard master-curve and the random inhomogeneity technique yielded about the same T_o, namely -103 °C and -93 respectively. In conclusion, one can assert that, for safety assessment, the determination of T_o by the master-curve does not appear to be a serious issue but it is rather a selection of the appropriate lower bound (possible lower than 1%) as well as of the correct temperature margin to add to T_o.

Attempts to link microstructural brittle features to inhomogeneity of fracture toughness have been done by Gelles and Sokolov [41]. These authors performed fractography, metallographic and SEM observations of broken specimens and revealed larger particles rich in Ta and O dispersed through the plate thickness. The size distribution measurement of these particles indicates a rather homogeneous distribution through the plate. Tanigawa *et al.* [42] also study the nature of the inclusions. They also found that Ta does not form MX precipitates in F82H-mod but forms composite Al_2O_3-Ta(V,Ti)O oxides (composite) or Ta(V)O oxides (single phase) and that the composite ones are dominant at the bottom of the ingot. From fractography observations, Tanigawa *et al.* suggested that the inhomogeneity in composite inclusion distribution is responsible of the very low toughness data point reported by Sokolov only as the specimens were taken from the bottom of the ingot.

In this work, large oxide composite up to 25 µm were also identified in F82H-mod. While one could be tempted to associate low fracture toughness to the presence of these oxides, the exact role they really play in the overall sequence of micro-mechanisms leading to macroscopic fracture certainly remains speculative. As discussed above, it is believed that the initiation of the macro-crack results from the nucleation and coalescence of many micro-cracks within the small process zone. The presence of few large inclusions in the vicinity of the crack is likely to contribute to a decrease of toughness but quantifying this effect remains an open issue. In any case, it is thought that the σ^*-A^* local criterion for fracture is not significantly modified by the presence of these big inclusions because this criterion represents the local stress field to create a large collection of micro-cracks emanating from other initiators than those inclusions. This assertion is supported by the fact that the 1% lower bound F82H-mod is not much different than that of Eurofer97, which was reconstruct with a nominal critical stress σ^* of 2000 MPa and such a value of the critical stress was shown to be consistent with micro-crack of about 1 µm. Thus, if big particles (> 10 µm) mediated the lower bound then the critical stress should be lower than 1000 MPa as shown in Figure 6-1 and the shape of the lower would be different from what it actually is.

6.6   References

[1]   Westergaard HM. Bearing Pressures and Cracks. Journal of Applied Mechanics. 1939;6:49-53.

[2]   Irwin GR. Analysis of Stresses and Strains near the End of a Crack Traversing a Plate. Journal of Applied Mechanics. 1957;24:109-114.

[3]   Hutchinson JW. Singular behaviour at the end of a tensile crack in a hardening material. J Mech Phys Solids. 1968;16:13-31.

[4]   Rice JR, Rosengren GF. Plane strain deformation near a crack tip in a power-law hardening material. J Mech Phys Solids. 1968;16:1-12.

[5]   O'Dowd NP, Shih CF. Family of crack-tip fields characterized by a triaxiality parameter - I. Structure of fields. J Mech Phys Solids. 1991;39:989-1015.

[6]   Larsson SG, Carlsson AJ. Influence of non-singular stress terms and specimen geometry on small-scale yielding at crack tips in elastic-plastic materials. J Mech Phys Solids. 1973;21:263-277.

[7]   Pineau A. Development of the local approach to fracture over the past 25 years: theory and applications. International Journal of Fracture. 2006;138:139-166.

[8]   Ritchie RO, Knott JF, Rice JR. On the Relationship Between Critical Tensile Stress and Fracture Toughness in Mild Steel. J Mech Phys Solids. 1973;21(395-410).

[9]   Anderson TL, Stienstra DIA, Dodds RH. A theoretical framework for addressing fracture in the ductile-brittle transition region. Fracture mechanics: 24th volume, ASTM STP 1207. Philadelphia: American Society for Testing and Materials; 1995.

[10]   Dodds RH, Shih CF, Anderson TL. Continuum and Micromechanics Treatment of Constraint in Fracture. International Journal of Fracture. 1993;64:101-133.

[11]   Anderson TL, Dodds RH. Specimen size requirement for fracture toughness testing in the transition region. J Test Eval. 1991;19(2):123-134.

[12]   Dodds RH, Anderson TL, Kirk M. A framework to correlate a/W ratio effects on elastic plastic fracture toughness (Jc). International Journal of Fracture. 1991;48:1-22.

[13]   Nevalainen M, Dodds R. Numerical Investigation of 3-D Constraint Effects on Brittle Fracture in SE(B) and C(T) Specimens. International Journal of Fracture. 1995;74:131-161.

[14]   Odette GR, He MY. A cleavage Toughness Master Curve Model. Journal of Nuclear Materials. 2000;283-287:120-127.

[15]   Odette GR, Rathbun HJ, Rensman JW, van_der_Broek FP. On the Transition Toughness of Two RA Martensitic Steels in the Irradiation Hardening Regime: a Mechanism-Based Evaluation. Journal of Nuclear Materials. 2002;307-311:1011-1015.

[16]   Rathbun HJ, Odette GR, He MY, Yamamoto T. Influence of statistical and constraint loss size effects on cleavage fracture toughness in the transition - A model based analysis. Engineering Fracture Mechanics. 2006;73:2723-2747.

[17]   Curry DA, Knott JF. Effect of Microstructure on Cleavage Fracture Toughness of Quenched and Tempered Steels. Metal Science. 1979;13:341-345.

[18]   Bowen P, Druce SG, Knott JF. Effects of microstructure on cleavage fracture in pressure-vessel steel. Acta Metallurgica. 1986;34:1121-1131.

[19]   Odette GR, Yamamoto T, Rathbun HJ, He MY, Hribernik ML, Rensman JW. Cleavage fracture and irradiation embrittlement of fusion reactor alloys: mechanisms, multiscale models, toughness measurements and implications to structural integrity assessment. Journal of Nuclear Materials. 2003;323:313-340.

[20]   Roberts SG, Noronha SJ, Wilkinson AJ, Hirsch PB. Modelling the initiation of cleavage fracture of ferritic steels. Acta Materialia. 2002;50:1229-1244.

[21]   Price AT, Holl HA, Greenough AP. The surface energy and self diffusion coefficient of solid iron above 1350°C. Acta Metallurgica. 1964;12:49-58.

[22]   Kohlhoff S, Gumbsch P, Fischmeister HF. Crack propagation in b.c.c. crystals studied with a combined finite-element and atomistic model. Phil Mag A. 1991;64:851-878.

[23]   Knott JF. Some effects of hydrostatic tension on the fracture behaviour of mild steel. J Iron Steel Inst. 1966;204:104-111.

[24]   Wilshaw TR, Rau CA, Tetelman AS. A general model to predict the elastic-plastic stress distribution and fracture strength of notched bars in plane strain bending. Engineering Fracture Mechanics. 1968;1:191-196.

[25]   Ortner SR, Hippsley CA. Two component description of ductile to brittle transition in ferritic steel. Materials Science and Technology. 1996;12:1035-1042.

[26]   Spätig P, Odette GR, Lucas GE. Low Temperature Yield Properties of Two 7-9Cr Ferritic/Martensitic Steels. Journal of Nuclear Materials. 1999;275:324-331.

[27]   Coates M, Kumar A, Roberts SG. Crack initiation in the brittle fracture of steels. Fatigue Fract Engng Mater Struct. 2006;21:661-671.

[28]   Edsinger K. PhD Thesis: Fracture Reconstruction and Advanced Micromechanical Modeling of Structural Steels. Santa Barbara: University of California; 1995.

[29]   Odette GR, Edsinger K, Lucas GE, Donahue E. Developing fracture assessment methods for fusion reactor materials with small specimens. ASTM-STP-1328, American Society for Testing and Materials, Philadelphia, PA. 1998:p. 298.

[30]   Spätig P, Donahue E, Odette GR, Lucas GE, Victoria M. Transition Regime Fracture Toughness-Temperature Properties of Two Advanced Ferritic/Martensitic Steels. Material Research Soc Symp Proc- Multiscale Modeling of Materials, Editors: LP Kubin, JL Bassani, K Cho, H Gao, RLB Selinger 653. 2001:pp. Z7.8.1-Z.7.8.6.

[31]   Wallin K. The Scatter in K_{IC}-Results. Engineering Fracture Mechanics. 1984;19:1085-1093.

[32]   Wallin K, Saario T, Törrönen K. Statistical model for carbide induced brittle fracture in steel. Metal Science. 1984;18:13-16.

[33]   Beremin FM. A Local Criterion for Cleavage Fracture of a Nuclear Pressure Vessel Steel. Metallurgical Transactions A. 1983;14A:2277-2287.

[34]   Gao X, Ruggieri C, Dodds RH. Calibration of Weibull stress parameters using fracture toughness data. International Journal of Fracture. 1998;92:175-200.

[35]   Wallin K, Laukkanen A, Tähtinen S. Examination on Fracture Resistance of F82H Steel and Performance of Small Specimens in Transition and Ductile Regimes. ASTM STP 1418, Small Specimen Test Techniques: Fourth Volume. 2002.

[36]   Sokolov MA, Tanigawa H. Application of the master curve to inhomogeneous ferritic/martensitic steel. Journal of Nuclear Materials. 2007;367-370:587-592.

[37]   Lucon E. A closer look at the fracture toughness of ferritic/martensitic steels. Journal of Nuclear Materials. 2007;367-370:575-580.

[38]   IAEA. Technical reports series No 429, "Guidelines for application of the master curve approach to a reactor pressure vessel integrity in nuclear power plants". IAEA, Vienna; 2005.

[39]   ASTM. E 1921 - 08. Standard Test Method for Determination of Reference Temperature, T_0, for Ferritic Steels in the Transition Range; 2008.

[40]   Wallin K, Nevasmaa P, Laukkanen A, Planman T. Master Curve analysis of inhomogeneous ferritic steels. Engineering Fracture Mechanics. 2004;71:2329-2346.

[41]   Gelles DS, Sokolov MA. Fusion Materials Semiannual Progress Report for Period Ending December 31, 2003. DOE/ER-0313/35. 2003.

[42]   Tanigawa H, Sawahata A, Sokolov MA, Enomoto M, Kueh RL, Kohyama A. Effects of Inclusions on Fracture Toughness of Reduced-Activation Ferritic/Martensitic F82H-IEA Steels. Materials Transactions. 2007;48:570-573.

Chapter 7

Conclusions

In this work we studied brittle fracture in tempered martensitic steels for fusion applications. We focused on two reduced-activation steels: F82H-mod and Eurofer97. The main activities were carried out on Eurofer97, which is the most recently developed steel. Mechanical tests were performed to characterize the fracture properties in the ductile-to-brittle transition region with pre-cracked and notched tensile specimens and to investigate the plastic flow properties with standard tensile specimens. Characterization of the microstructure was also done by optical microscopy, scanning electron microscopy, transmission electron microscopy and energy-dispersive X-ray spectroscopy

Three sizes of pre-cracked compact fracture specimens of Eurofer97 steel were produced and tested in the temperature range [-197 ºC, -40 ºC]. Notched tensile specimens and normal tensile specimens of Eurofer97 were also tested in the temperature range [-160 ºC, 20 °C]. The experimental fracture toughness data was analyzed in terms of the standard master-curve method (ASTM-E1921 standard) that was originally developed to determine a ductile-to-brittle transition temperature, T_0, in fission reactor pressure vessel steels from a small number of fracture toughness tests. 3D and 2D finite element simulations of the tested compact specimens as well as

axisymmetric finite element simulations of the notched and tensile specimens were undertaken in order to study the stress fields at the onset of cleavage fracture initiation for the different studied temperatures.

In order to have a good description of the scatter in the transition, the standard master-curve equation had to be slightly modified. To do so, the reference temperature as well as the athermal part of the master-curve equation was fitted using the maximum likelihood method. This fitting was possible due to the large number of measured data points and the following modified master-curve equation was obtained:

$$K_{Jc\_median}(T) = A + (100MPa\sqrt{m} - A)exp(C(T - T_0)) .$$

With $A = 12MPa\sqrt{m}$ and $C = 0.019/\,^{\circ}C$. The athermal component in the last equation is represented by the coefficient A, which is equal to 30 MPa m$^{1/2}$ in the standard master-curve. The proposed *modified* master-curve allowed predicting T_0 values, from a small number of small specimens tested in the lower transition temperature range, which are consistent with T_0 values obtained with bigger specimens in the middle transition. This was possible because the modified master-curve properly predicts the scatter distribution of the experimental data. The benefit of this master-curve equation adjustment was outlined, in particular to realize a reliable T_0 determination from the limited number of specimens that are usually incorporated in irradiation capsules.

The specimen fracture size requirements were investigated. A determination of the adequate value of the dimensionless parameter M, which sets the maximum K_{Jc} value that can be measured with a given specimen size at a specific yield stress, was performed. The ASTM-E1921 standard recommends M=30. Nevertheless, we showed that even when the ASTM size requirements were fulfilled, the 0.35T C(T) Eurofer97 specimens and the 0.4T C(T) F82H-mod specimens yielded a 1T-adjusted toughness value much higher than the expected values. An M value larger than about 100 is needed to avoid constraint loss effects that artificially increase toughness and decrease T_0. This clearly indicated that the standard minimum specimen size limit related to M = 30 is too lenient for these tempered martensitic steels. Another clear indication that

M = 30 is too low for these materials is the fact that the ductile-to-brittle transition temperature, T_0, has a significant dependence with M for values below 100 for instance.

2D and 3D finite element simulations of pre-cracked compact specimens were run. Stationary blunting cracks were simulated. The 3D simulation results were validated by showing an excellent agreement between the calculated and experimental load-displacement curves for specimens that fail below maximum load before some crack growth takes place. The calculated stress fields around the crack tip using material constitutive properties at different temperatures were analyzed within the framework of a simple local fracture model. The local fracture criterion to trigger unstable fracture is based upon the attainment of a critical value σ^* of the principal stress within a critical volume V^*, considering these two parameters temperature independent. Using the results of the 2D simulations, the model was employed first to reconstruct the temperature dependence of the lower bound of the modified master-curve of Eurofer97 and to study the effect of the critical parameters σ^* and V^* on the shape of the toughness-temperature curve. The 3D simulations were analyzed to quantify the effect of constraint loss that lead to the apparent fracture toughness increase by decreasing the specimen size. Special attention to quantify the effect of the initial root radius in the determination $V^*=V^*(\sigma^*)$ is needed. Using the calibrated values of the σ^*-V^* model, we showed that the dimensionless parameter M determined from the simulations is fully consistent with the M value obtained previously by looking at the M-dependence of the reference temperature T_0. The calibrated stress was associated to the critical stress necessary to propagate a micro-crack of about of the order of 1 μm in the ferritic matrix using the Griffith's energy balance equation.

Axisymmetric simulations of notched and standard tensile specimens were also performed. The stress fields in the vicinity of the notch and of the neck at fracture load were studied. The calibrated σ^*-V^* criterion with the pre-cracked C(T) specimens could be successfully used to predict the fracture load of the notched tensile specimens. However, the critical stress calculated in the neck of the standard tensile specimens indicated a higher value of the critical stress in comparison to that

of the pre-cracked and notched fracture specimens. This was interpreted as a limitation to the transfer of the σ*-V* criterion to configurations for which the triaxiality level is lower than in that of pre-cracked and notched fracture specimens.

While the microstructures of both steels are typical of tempered martensitic steels, some differences could be easily identified in terms of the prior austenite grain size, type of inclusions and carbides. The prior austenite grain size was about 7-8 times larger in F82H-mod than in Eurofer97. Tantalum was added to these steels in order to create a fine dispersion of Tantalum carbides, which are supposed to stabilize the prior austenitic grain size. These small carbides were found in Eurofer97 but not in F82H-mod. Ta in F82H-mod was found in the form of very large complex oxides (AlTaTiO). These inclusions in F82H-mod were even larger than 10 μm that corresponds to the mean prior austenite grain size of Eurofer97. Such large inclusions were not observed in Eurofer97. Despite these microstructural differences, the fracture properties between the two investigated steels were quite similar even though the reference temperature T_0 was about 20 °C lower for F82H-mod. The scatter in the transition region was perfectly described by the master-curve method for Eurofer97 while an excessive number of fracture toughness data fell below the 1% tolerance bound in F82H-mod. These low toughness points could be related to the mentioned big inclusions found in F82H-mod. Taking into account these two observations (lower T_0 and excessive scatter in F82H-mod), the overall fracture databases are encompassed by practically the same tolerance bound.

Acknowledgements

First of all I want to say thank you to Dr. Philippe Spätig. It was really great working with him during the last four years, I am happy to have had the opportunity to work with a very good person like him and at the same time an excellent PhD advisor and scientist.

I also want to acknowledge Dr. Bonadé, Dr. Campitelli, Dr. Kruml, Prof. Odette and Dr. Schäublin for their help in different opportunities during my work.

I appreciate a lot the work performed by Prof. Baluc leading the Fusion Technology – Materials Group and Prof. Tran leading the whole Plasma Physics Research Center, CRPP.

For making a very nice working atmosphere in our fusion materials group I want to acknowledge all members from the last four years, Raul, Emiliano, Philippe, Robin, Nadine, Nazar, Paulina, Julijana, Pierre, Masood, Mira, Amutan, Eugenia, Roger, Guillaume, Gabriel, Stefan, Jan, Jürgen, Caroline, Yu Gang, Apostolos, Andreas, Zbyszek. The group is a nice mix of nice people coming from many different Swiss cantons and countries like, Geneva, Vaud, Neuchâtel, Aargau, Fribourg, France, Germany, Poland, Argentina, Serbia, Rumania, Bulgaria, Greece, Iran, China, Czech Republic, India and Ukraine.

Finally I want to say thank you to my family which gave me the most important help and support of all.

Pablo Mueller

Born July 14th 1977, married, 2 children.

2005 – 2009   EPFL, École Polytechnique Fédéral de Lausanne, CRPP, Centre de Recherche en Physique des Plasmas, Fusion Technology – Materials, Villigen PSI, Switzerland.

        PhD Thesis: "Finite element modeling and experimental study of brittle fracture in tempered martensitic steels for thermonuclear fusion applications"

2003 – 2005   CNEA, Comisión Nacional de Energía Atómica, Engineer, Bariloche, Argentina.

        Universidad Nacional de Cuyo, Instituto Balseiro, Teaching assistant, Bariloche, Argentina.

1999 – 2003   IB, Balseiro Institute, Bariloche, Argentina.

        Master Thesis: "Turbulent Flows Finite Element study using Large Eddy Simulation techniques"

        Nuclear Engineer

1996 – 1999   UBA, University of Buenos Aires, Engineering student.

Selected publications related to this work

P. Mueller, P. Spätig, "Finite element simulation of tensile tests including necking and a local approach model for fracture", SEECCM 2009, Proceedings of the 2nd South-East European Conference on Computational Mechanics, Rhodes, Greece, 22-24 June 2009.

P. Mueller, P. Spätig, "3D finite element and experimental study of the size requirements for measuring toughness on tempered martensitic steels", *Journal of Nuclear Materials*, Volume 389, Issue 3, Pages 377-384, 1 June 2009.

P. Spätig, R. Stoenescu, P. Mueller, G. R. Odette, D. Gragg, "Assessment of irradiation embrittlement after 590 MeV proton irradiation of the Eurofer97 steel using mini pre-cracked bend bars", *Journal of Nuclear Materials*, Volumes 386-388, Pages 245-248, 30 April 2009.

P. Mueller, P Spätig, R. Bonadé, G. R. Odette, D. Gragg, "Fracture toughness master curve analysis of the tempered martensitic steel Eurofer97", *Journal of Nuclear Materials*, Volumes 386-388, Pages 323-327, 30 April 2009.

R. Bonadé, P. Mueller, P Spätig, "Fracture toughness behavior in the ductile–brittle transition region of the tempered martensitic Eurofer97 steel: Experiments and modeling", *Engineering Fracture Mechanics*, Volume 75, Issue 13, Pages 3985-4000, September 2008.

P. Mueller, R. Bonadé and P. Spätig, "Fracture properties of notched and pre-cracked specimens of a tempered martensitic steel at low temperature", *Materials Science and Engineering A*, Volumes 483-484, Pages 346-349, 15 June 2008.

P. Spätig, R. Bonadé, G.R. Odette, J.W. Rensman, E.N. Campitelli and P. Mueller, "Plastic flow properties and fracture toughness characterization of unirradiated and irradiated tempered martensitic steels", *Journal of Nuclear Materials*, Volumes 367-370, Part 1, Pages 527-538, 1 August 2007.